



HAL
open science

Remote sensing of swell and currents in coastal zone by HF radar

Weili Wang

► **To cite this version:**

Weili Wang. Remote sensing of swell and currents in coastal zone by HF radar. Oceanography. Université de Toulon; Zhongguo hai yang da xue (Qingdao, Chine), 2015. English. NNT : 2015TOUL0011 . tel-01393566

HAL Id: tel-01393566

<https://theses.hal.science/tel-01393566>

Submitted on 7 Nov 2016

HAL is a multi-disciplinary open access archive for the deposit and dissemination of scientific research documents, whether they are published or not. The documents may come from teaching and research institutions in France or abroad, or from public or private research centers.

L'archive ouverte pluridisciplinaire **HAL**, est destinée au dépôt et à la diffusion de documents scientifiques de niveau recherche, publiés ou non, émanant des établissements d'enseignement et de recherche français ou étrangers, des laboratoires publics ou privés.

ÉCOLE DOCTORALE 548 : Mer et Sciences
Institut méditerranéen d'océanologie

THÈSE

présentée par :

Weili WANG

soutenue le : 27 mai 2015

pour obtenir le grade de Docteur en Sciences de l'Univers

Spécialité : Océanographie, Sciences de l'Univers

Remote sensing of swell and currents in coastal zone by HF radar

THÈSE dirigée par :

Monsieur FORGET Philippe

Directeur de recherche CNRS, Institut
méditerranéen d'océanologie (MIO), Université de
Toulon

Monsieur GUAN Changlong

Professeur, Université océanique de Chine
Qingdao

JURY :

Monsieur ARDHUIN Fabrice

Directeur de recherche CNRS, IFREMER
Centre de Bretagne

Monsieur FRAUNIE Philippe

Professeur des Universités, Université de
Toulon

Monsieur YIN Baoshu

Professeur, Université océanique de Chine
Qingdao

Monsieur ZHAO Dongliang

Professeur, Université océanique de Chine
Qingdao

To my dearest grandmother forever.

----- Weili WANG

Remote sensing of ocean swell and some other coastal processes by HF radar

Abstract

Nearshore marine environment contains many complex processes, but the lack of high-resolution data over a large area during a long time is often the primary obstacle to further research. High-frequency (HF) radar is a mean of remote sensing which obtains continuous near-real time sea surface information over a large area. Thus the study of inversion of marine parameters from HF radar data is very meaningful. This thesis makes use of a 13-month-long dataset collected by two phased array HF radar to investigate the characteristics of the sea echo signals, study the data processing and inversion methods, compute sea surface parameters and evaluate the accuracy of radar inversion of swell parameters.

The thesis refers to the ground wave HF radar, whose radio waves interact with ocean by Bragg resonance scattering. The development history and applications of HF radar is introduced. The basic theory of electromagnetic wave is reviewed. The principles of inversion of sea surface current, wind direction and swell parameters are described. The feasibility of the swell parameter inversion is investigated.

Based on theoretical analysis and statistical studies of a large number of samples, the thesis proposes a series of methods on raw signal processing and quality control, including the determination of the noise level, data averaging in space and time, the proper identification of spectral peaks, the peak width threshold, etc. Respecting the characteristics of different physical processes, inversions of current and wind use spectra collected every 20 min; inversion of swell parameters uses one-hour averaged spectra. The statistics of qualified spectra for swell parameter calculations are presented for both stations. A set of efficient, with a reduced computational cost, automatic computing programs are developed to do the processing and derive marine parameters.

Radial current velocities are derived from single radar station. Current vector fields are obtained by combination of both stations. One-year mean flow field in the Iroise Sea is shown, together with the computation of vorticity and divergence. A one-month SeaSonde radar dataset off Qingdao is studied. One-month mean flow pattern together with vorticity and divergence are presented.

Relative wind direction with respect to radar look direction is measured through ratio of Bragg peaks amplitudes. Different empirical models are employed to derive radar-inverted relative wind direction. Results show reasonable agreement with model estimations. Different directional distribution models are used to measure the spreading factor for the Iroise Sea.

The thesis focuses on the study of swell parameters. Results are validated by buoy and wave model (WAVEWATCH III) data. The assessments show that the accuracy of swell frequency is very good, the accuracy of swell significant waveheight is reasonable, and the accuracy of relative swell direction is low. Consistency of measurements by both radar stations is verified by comparison between the two. This also supports the use of double samples to do the inversion. Use of two radars not only further improves the accuracy but also solves the ambiguity of relative swell direction from single station and gives the absolute wave direction to a certain precision. The thesis proposes a constant relative direction method to derive swell significant waveheight, based on the studies of radar integral equation and the inverted results of relative swell direction. This proposal is demonstrated to improve the agreement of radar inversion and buoy/model provided significant waveheight and increases significantly the number of samples.

The thesis investigates the accuracy of swell parameters obtained by HF radar. Contributions of random errors in radar observations are quantified. Comparing the differences between radar and buoy/model estimations gives assessments of the contribution of radar intrinsic uncertainty and contribution of other factors.

Keywords: High-frequency radar; Doppler spectrum; swell; current; wind direction; Iroise Sea

Table of contents

1	Introduction.....	1
1.1	HFR system.....	1
1.2	Development history.....	2
1.3	Applications of HFR.....	3
1.4	Objectives and Contributions.....	6
1.5	Organization of the thesis.....	8
2	Methodologies.....	10
2.1	Basic backscatter theory.....	10
2.2	Methods for the inversion of surface current.....	14
2.3	Methods for the inversion of wind direction.....	16
2.4	Methods for the inversion of swell.....	20
2.4.1	Swell frequency.....	23
2.4.2	Swell waveheight.....	24
2.4.3	Relative swell direction.....	27
3	Radar data processing.....	30
3.1	Locations and radar parameters.....	30
3.2	Beam forming.....	32
3.3	Averaging of Doppler spectra.....	33
3.4	Quality control.....	37
3.5	Statistics of qualified spectra.....	43
3.6	Summary.....	45
4	Results of surface currents.....	47
4.1	Radial current velocities.....	47
4.2	Total current vectors.....	50
4.3	Currents by SeaSonde.....	54
4.4	Summary.....	59
5	Results of wind directions.....	60
5.1	Radar inverted relative wind direction.....	60
5.2	Measurement of spreading parameter.....	61
5.3	Summary.....	65
6	Results of swell.....	66
6.1	Swell frequencies.....	66
6.1.1	Consistency of both radar measurements.....	66
6.1.2	Comparison with buoy data.....	70
6.1.3	Comparison with model data.....	75
6.2	Swell directions.....	84
6.2.1	Comparison between POS and LS methods.....	84
6.2.2	Comparison with model data.....	85
6.2.3	Absolute swell direction.....	88

6.3 Swell significant waveheights.....	90
6.3.1 Comparison with buoy data	91
6.3.2 Comparison with model data	93
6.3.3 Consistency of both radar measurements	99
6.4 Summary	100
7 Accuracy analysis	101
7.1 Radar intrinsic errors.....	101
7.1.1 Random error in radar-inverted frequency	102
7.1.2 Random error in radar-inverted relative direction	103
7.1.3 Random error in radar-inverted waveheight.....	104
7.2 Methodological discrepancies.....	104
7.3 Buoy and model intrinsic errors.....	105
7.4 Summary	105
8 Conclusions and perspectives	107
8.1 Main conclusions	107
8.2 Inadequate points and future work.....	108
Appendix A.....	111
References	113
Acknowledgements.....	121
CV	122
List of articles	123

1 Introduction

1.1 HFR system

High-frequency radar (HFR) is a radio equipment transmitting electromagnetic waves at high-frequency band (3-30MHz). The radio wavelength ranges from 10 m to 100 m.

There are two types of HFR divided by the way of propagation of radio waves: sky wave HFR and ground wave HFR. Sky wave radar is also called over-the-horizon (OTH) radar. Its radio wave propagates via ionospheric reflection and detects targets over the horizon. It is employed mainly for long distance tracking, but the spatial resolution is much limited. This thesis concerns only the ground wave HFR deployed for the observation of sea surface. It is usually installed on shore. Ground wave is transmitted at grazing angle and propagates over the conductive ocean surface. Radio waves are vertically polarized. Radio waves are backscattered by ocean waves with certain wavelength and are collected by the receive antenna. Information of the sea surface, such as currents, waves and winds etc., is carried back in the received voltage signals. The raw signals can be analyzed via specific processing techniques and inversion methodologies.

According to radar antenna structure and direction resolving technique HFRs are also divided into two categories. One category is the broad beam radar using cross-loop receiving antenna. A representative system is SeaSonde, former CODAR (Coastal Ocean Dynamics Applications Radar) system by CODAR Ocean Sensors (Barrick et al. 1977a; Lipa and Barrick 1983). SeaSonde transmits FMICW pulse waves. It uses compact antenna and receives backscattered sea echoes in all directions. The multiple signal classification method MUSIC (Multiple Signal Classification) (Schmidt 1986) is employed for azimuthal determination. SeaSonde occupies small area to be installed and is very flexible for application. The other category is narrow beam radar using a phased array antenna system. The representative narrow beam radar system is WERA (Wellen Radar) (Gurgel et al. 1999; Liu et al. 2014). WERA uses FMCW chirp waves. It makes use of a relatively large array of antenna (100 m or so). The received sea echo signals are analyzed by BF (Beam Forming) technique to select the azimuths of observation. The system can also be configured to operate in direction-finding mode. It provides fine azimuthal resolution at the cost of larger area

of land and higher power consumption.

HFR reaches a wide area, like hundreds of kilometers depending on the transmitting frequency etc., off shore. It has fine spatial (e.g. 1.5 km) and temporal resolutions (e.g. 20 min). Meanwhile, HFR costs low power consumption (e.g. transmitting power of 40 watts on average by SeaSonde) and works continuously even during extreme weather conditions. Radar coverage is divided into small units in a polar coordinate by distance and angle centered at radar station. The radar-inverted measurement of a sea surface parameter in one radar cell is the mean sea surface information over the small patch.

1.2 Development history

The capability of HF radar for ocean surface observation was discovered in the 1950's. Crombie (1955) studied sea echoes from a rough, moving sea surface collected by radar transmitting at 13.56MHz. For the first time he pointed out that the principle of radar signal backscattering was because of Bragg resonance between electromagnetic waves and Bragg waves with half radio wavelength. This opened the era of research on theories and applications of HF radar remote sensing of the ocean surface. Crombie (1972) investigated the relationship between sea echoes collected from two neighboring radar beams and found that a homogeneous surface currents field brought additional Doppler shift to the backscattered spectra. His research suggested that underlying currents can be tracked by the Doppler frequencies of first-order spectral peaks. Based on these studies, the very first HFR system all over the world for monitoring the surface currents was born in the 1970's. It was a CODAR system developed by WPL (Wave Propagation Laboratory) in NOAA (National Oceanic and Atmospheric Administration) in US.

Giving the unique advantage of field observation instead of point measurement by traditional devices, HFR immediately attracted worldwide interests. Since then, research on currents observation by HFR boomed in Germany, Japan, Britain, Australia etc. Many countries started to develop their own radar systems. UK developed the commercial radar OSCAR (Ocean Surface Current Radar) for sea surface currents and residual current observations (Prandle 1987). James Cook University in Australia (James Cook University) built COSRAD (COStal ocean rADar) radar system (Heron and Rose 1986). University of Hamburg in Germany designed the WERA system with phased array antennas within the European project - surface

current and wave variability experiment, SCAWVEX (Gurgel et al. 1999). In fact, University of Hamburg initially used the radar system from NOAA in 1980. In the following five years the radar was tested and experiments were carried out (Essen et al. 1983). They carried out a number of improvements concerning this radar system on both hardware and software facilities. Progresses were achieved on reducing internal noise, improving accuracy and sensitivity, optimizing algorithms etc. Accumulation of these electronic and algorithmic experiences helps propose the new radar system, WERA. This system can use transmit frequencies of 5-45MHz. WERA is more flexible in adjusting spatial resolution. Range resolution ranges 250m-2km. WERA improved some shortcomings of CODAR system on ocean wave observations by allowing beam-forming (BF) with up to 16 receive antennas. The BF technique is critical for obtaining reliable high-quality second-order Doppler spectra. It also improves radar observation coverage area.

A rough statistics by Fujii et al. (2013) showed that by 2013 there were at least 268 HFRs all over the world. A majority of them used standard transmit frequency of 10-100 MHz band. The other 100 stations made use of longer radio waves of 3-10 MHz. Asian countries including China, Japan, Korea, Indonesia, Thailand and Vietnam, had at least 96 stations in all, 69 using stand transmitting band and 41 using low transmitting band. Most of these HFRs are commercial systems, mainly CODAR and WERA. Among these countries, Japan has the largest number of HFRs, followed by Korea and China. Japan and China both have two kinds of HFR, cross-loop and phased-array, while Korea has only the former one. Japan and China are also devoted to develop their own HFR system. China is very concerned about the development and application of HFR. There are no less than 15 stations, including systems of SeaSonde (CODAR), WERA and OSMAR (Ocean State Monitoring and Analyzing Radar) developed by Wuhan University (e.g. Wu et al. 2003).

There have been several decades since the first HFR system was implemented to measure surface currents. To date, HFRs have been greatly developed and achieved many progresses. With increasing demand for near real-time ocean surface observations many countries set out to establish marine radar network, such as NOAA's IOOS in US.

1.3 Applications of HFR

As was mentioned in Section 1.2, the mechanism of HFR sea echo backscatter is

Bragg resonance scattering (Crombie 1955). The corresponding feature in the Doppler spectrum is two most significant symmetrically located sharp peaks, called Bragg peaks or first-order peaks (Barrick 1972a). The ocean waves interacting with electromagnetic waves have wavelengths of half radio wavelength as the incident angle is near grazing, and they propagate along the radar look direction. These ocean waves are called Bragg waves. Bragg peak positions in the Doppler frequencies are irrespective of sea state and are determined exclusively by the frequency of Bragg waves in absence of surface currents. Without currents, radar transmitting frequency is the only factor determining Bragg peak frequencies as it determines the frequency of Bragg waves.

The existence of surface current brings additional Doppler shift of the Bragg peaks from their theoretical frequencies (Crombie, 1972). By measuring this quantity of current-induced Doppler shift, the velocity component of surface current in the radial direction of radar station, also simply called radial velocity, can be derived. Radial velocity by two or more of HFR stations can be combined to give surface current vector field by the law of vector.

The principle of the inversion of current is straightforward. Using the first-order spectra, HFR provides the most reliable sea surface parameter - the surface current field. Stewart and Joy (1974) validated the theory of current inversion using drogue measurements of the same currents in the Pacific near California in January 1973. Barrick et al. (1977a) and Frisch and Weber (1980) did a series of experiments and gave the root-mean-square difference (RMSD) between radar-derived currents and in situ measurements of 15 cm/s - 27 cm/s. Paduan and Rosenfield (1996) obtained RMSD of 13 cm/s. Chapman et al. (1997) measured RMSD among different radar stations of 9 cm/s to 16 cm/s. Kosro et al. (1997) compared currents by ADCP with radar measurements and obtain the RMSD of 15 cm/s with the correlation coefficient of 0.8. Currently, HFR technique of sea surface current is well developed and is widely used in field observations of circulation in coastal waters (Shay et al. 2007; Kim et al. 2011; Zhao et al. 2011). Meanwhile, further separation of surface flow components has been investigated. With studies of local tides, the residual current field can be obtained (Ardhuin et al. 2009a; Sentchev et al. 2013). Moreover, the concept of measuring vertical structure of current by HFR, originally proposed by Stewart and Joy (1974), has been further developed. Different electromagnetic waves go through different depths on the surface layer of the sea. Thus the shear of vertical

velocity of sea surface current can be measured by HFR (Shrira et al. 2001; Ivonin et al. 2004).

Barrick (1972a) derived the first-order equation of radar cross section based on the small perturbation assumption of surface waves. The equation describes not only the location of Bragg peaks in Doppler frequencies but also the relationship between the amplitude of Bragg peaks and the waveheight of Bragg waves. Long and Trizna (1973) carried out the first attempt to map winds over a large area by HFR. Researchers obtained different models relating the ratio of the strengths of first-order peaks in Doppler spectra and the sea surface wind direction (Tyler et al. 1974; Harlan and Georges 1974). Most analyses showed the accuracy of wind direction by HFR of around 20° (Stewart and Barnum 1975; Wyatt et al. 2006). Heron et al. (1985) discovered that the existence of swell decreased the accuracy of the measurement of wind direction. In that sense, the measurements of swell will contribute to the inversion of other surface parameters, such like wind direction. Wind speed is even more challengeable to be obtained from HFR (Cochin et al. 2005; Green et al. 2009; Shen et al. 2012). Approaches are mainly based on empirical relationship between wind and surface waves. However, the correspondence of surface waves and local winds are complex and may not be totally dependent. Wyatt et al. (2006) concluded that it is possible to derive wind directions with reasonably good accuracy when the first-order Bragg waves are perfectly driven by local wind but the inversion of wind speed is not sufficient accurate with HFR for operational use.

The less energetic continuum around first-order Bragg peaks is called the second-order spectra. Second-order spectra are generated by two wave trains with certain wavelengths propagating at certain angle. Rice (1961) described the random conductive ocean surface and the electromagnetic field above it as two-dimensional Fourier series. Hasselmann (1971) pointed out the correlation between the ocean surface and radar sea echo by interpreting the HFR Doppler spectrum as the product of wave spectrum multiplied by a weighting function. Barrick (1972b) derived the resolved integral relationship between ocean wave spectrum and second-order sea echo spectrum. In principle, ocean wave spectrum can be inverted from second-order spectrum of HFR sea echo (Wyatt 1986; Howell and Walsh 1993; Hisaki 2005; Lipa and Nyden 2005). However, the correspondence between the two is complex and wave measurement is highly dependent on the quality of data (Forget 1985; Wyatt et al. 2011). At present, most inversions of ocean wave spectrum use empirical or

semi-empirical models, and are mainly used to compute integral ocean parameters like significant waveheight of the total sea surface (Lipa and Barrick 1986; Wyatt 1990; Gill et al. 1996; Gurgel et al. 2006; Lipa et al. 2014).

There are other applications of HFR, such as recently implemented detection of tsunami (e.g. Lipa et al. 2006).

1.4 Objectives and Contributions

Hydrodynamic environment in near shore area is much concerned for the safety of human activities, like fishing, navigation, rescue, etc. The ocean surface is a complex combination of many processes. Surface waves are critical objects to be investigated. In nearshore area, shallow water causes increase of waveheight by shoaling. Waves break and release much energy into the water column and thus play an important role in the impact on coastal and offshore infrastructures.

The sea surface waves are usually divided into two groups: wind waves and swell. Wind waves are surface waves generated by local wind and contribute to the high frequency part of the total wave spectrum. Swell are surface waves generated by distant storms travelling across the ocean (Munk et al. 1963; Jiang and Chen 2013). Swell is usually located in the low frequency part of the total wave spectrum, with larger wavelengths and faster phase velocities. Wind waves dissipate much energy through wave breaking, whereas swell can spread over long distances due to smaller dissipation rate (Snodgrass et al. 1966; Collard et al. 2009; Ardhuin et al. 2010). In the ocean wave research, one of the interests is to separate wind wave and swell components from the complex total structure.

In recent years, contribution of swell in ocean processes has been much discussed. Laboratory studies by Phillips and Banner (1974) found that long-period waves inhibit growth of wind waves. Hara et al. (2003) used observations during two field programs to study the evaluation of the hydrodynamic modulation of wind waves by swell. Smedman et al. (2009) showed that the existence of swell accompanies variation of the profile of marine atmospheric boundary layer. Swell induces momentum and energy fluxes into the marine atmospheric boundary layer (Kudryavtsev and Makin 2004). Swell spread across the continental shelf and interacts with topography. Refraction and shoaling are caused by large-scale topography while the effects of intermediate scales and very small scales pose more difficulties to be understood (Ardhuin et al. 2003; Magne et al. 2007). The

mechanisms behind the observed nonlinear propagation, attenuation that may be associated with bottom friction, local wave environment and other factors are still under study. Swell propagation and dispersion characteristics have been recently improved (Ardhuin et al. 2009b; Young et al. 2013; Gallet and Young 2014). The existence of swell affects the inversion of other oceanic parameters (Drennan et al. 1999). McWilliams et al. (2014) showed that the presence of swell amplifies and rotates Lagrangian-mean current.

However, these studies, especially the investigation of time evolution, often suffer from lack of detailed field observations of swell. The most reliable ways to do marine observation are by traditional devices, like mooring buoys. They have high temporal resolution, good accuracy, but are mostly fixed-point observations and cost a lot. Moreover, traditional devices are much affected by local sea states. Some areas have strong tides and large currents. Some areas experience harsh local wind. These conditions bring difficulties for the proper operations of traditional devices and cost high labor price to maintain the equipment and collect data. In contrast to relatively few dataset by traditional meanings, satellites obtain information over a large area with fine resolution, like altimeter and recently developed synthetic aperture radar (SAR) (e.g. Forget et al. 1995; Chen et al. 2002; Collard et al. 2009). However, satellite measurements are sparse in time and the observation time is fixed by satellite trajectory. In the past decades, wave forecast had progressed rapidly. Computation of swell is often included in the computation of total wave spectrum. Yet, swell is still the most difficult component in the entire spectrum to be predicted (Rogers 2002). The utilization of HFR can compensate some shortcomings of traditional and satellite devices. HFR provides ocean surface measurements continuously in time in a large area with good temporal and spatial resolutions and at low cost. Also, HFR has high tolerance of the local environment and the weather due to its relatively long radio wavelength. These advantages meet requests in marine environment monitoring, forecasting, marine warning and research.

While there is quite some amount of work on the assessment of HFR measurements of surface currents, much less inversion results and analysis can be found for ocean waves. The correspondence between long-period ocean waves, typically swell, and sea echo spectrum by HFR is relatively simple (Broche 1979; Lipa and Barrick 1979). Swell contributes to four spikes in the second-order Doppler spectrum. They are located around the two first-order Bragg peaks. Swell parameters

can be obtained through positions and amplitudes of these swell peaks. Forget et al. (1981) further studied the detailed characteristics of the contribution of narrowband unidirectional swell. Lipa et al. (1981) gave a limited number of swell cases. The computation of wave direction is the most inaccurate. Bathgate (2006) discussed the method to find perpendicular swell by comparing spectra in different radar beams. The application of HFR on the observation of swell needs further investigation. Wyatt (2000) found that one important reason for the inaccuracy of radar inversion is the unguaranteed quality of sea echo. Thus, quality control of Doppler spectra and assessments of radar inversions deserve more attention. The main objective of this thesis is to do inversion of swell parameters, including frequency, direction and waveheight for an extensive 13-month dataset using an automatic quality control and computation program. Using this dataset and a one-month dataset collected by SeaSonde, surface currents and wind directions are also calculated and presented.

The work contributes to more detailed field observations of coastal environment by utilization of high-frequency radar. The results in this thesis offer quantitative knowledge of swell. Better knowledge of swell information contributes to better understanding of other hydrodynamic processes in the coastal ocean surface and the study of erosion of the coast and structures. Moreover, operational use of HFR for swell observation is desired in carrying out safe navigation, rational exploitation of the ocean, etc.

1.5 Organization of the thesis

The thesis firstly reviews basic electromagnetic theory and its application on radar backscattering in Section 2. Methodologies for inversion of surface currents, wind directions and swell parameters are described. Section 3 describes the 13-month dataset collected in Brittany, France from September 1 2007 to September 30 2008. The processing of raw voltage radar signals and quality control of radar spectra are presented. Careful design of quality control programs is presented. Temporal coverage of qualified data is shown in maps. A set of automatic programs are established to compute ocean parameters. Results on ocean surface currents are presented in Section 4. Radial velocities and combined field vectors are derived. In addition to the WERA system, the thesis shows also results of a one-month dataset collected by SeaSonde in Qingdao, China. Section 5 reviews the application of HFR for wind direction. The thesis investigates the directional distribution of wind waves in the Iroise Sea using

different models. The main results on swell parameters (frequency, direction and waveheight) are presented in Section 6. Consistency of radar measurements is investigated by comparing frequency and waveheight results from both stations in overlapped area. For the assessments of radar-inverted parameters, buoy measurements and WAVEWATCH III (WW3) hind casts are employed. The conventions of using these two dataset are described. An improved constant direction method is proposed to reduce the scatter of radar measurement of swell waveheight. The combined use of both radar stations improves radar-derived results and solves ambiguity of swell direction derived from single radar station. In Section 7, the accuracy of radar observations are analyzed over a large number of samples. Random errors after the averaging of Doppler spectra are quantified. The contribution of radar measurement uncertainty to the total deviation between radar and buoy/model estimations is assessed. Summaries and perspectives are given in Section 8.

2 Methodologies

2.1 Basic backscatter theory

Radar cross section, S , is defined as the ratio of actually received backscattered power, P_r , to incident power density at the location of receive antenna, P_{di}

$$S = \frac{P_r}{P_i} \quad (2-1)$$

where

$$P_{di} = \frac{GP_t A_e}{(4p)^2 l_1^2 l_2^2} \quad (2-2)$$

with P_t the total radar transmitting power; G the antenna gain; l_1 the distance between the transmit antenna and target; l_2 the distance between target and the receive antenna; A_e the effective area of the receive antenna.

The attenuation of vertically polarized electromagnetic ground-wave caused by roughness of the sea surface was investigated by Barrick (1971). A time-varying ocean surface, $z(x, y, t)$, can be described by Fourier series

$$z(x, y, t) = \sum_{m,n,l=-\infty}^{\infty} P(m, n, l) e^{ia(mx+ny)-iWlt} \quad (2-3)$$

where P is the amplitude coefficient of Fourier component; $a = 2p/L$ with L the spatial period of the surface; $W = 2p/T$ with T the temporal period of the surface; $i = \sqrt{-1}$.

For ground-wave HFR, incident electromagnetic waves and backscattered radio waves interact with surface ocean waves with certain wavelength propagating in the plane of incidence. This effect of Bragg scattering is also called first-order effect or linear effect as mentioned in Section 1.3. The corresponding features in the HFR Doppler spectrum are two symmetrically located sharp peaks, called Bragg peaks. Radio wavelength, l , and Bragg wave length, L , following

$$l = 2L \cos q_0 \quad (2-4)$$

with q_0 the angle between radio wave and the sea surface. As HFR incidences at near grazing angle, q_0 is near 0. With the cosine function in the right approximately equal to 1, the length of Bragg wave is about half of radar wave length

$$L = \frac{I}{2} \quad (2-5)$$

The Doppler shift of Bragg peaks in Doppler frequencies in a radar Doppler spectrum is called Bragg frequency, f_B . It is determined by phase speed of Bragg waves, V , and radar wavelength

$$f_B = 2V / I \quad (2-6)$$

For the gravity waves, V and L satisfy the relationship

$$L = 2pV^2 / g \quad (2-7)$$

with g the gravitational acceleration. Combining the three equations above gives

$$f_B = \frac{1}{2p} \sqrt{2gk_0} \quad (2-8)$$

with k_0 the radar wavenumber. Then the Bragg frequency is determined only by the radar transmitting frequency and is proportional to the root mean square of radar frequency.

After Crombie discovered the Bragg scattering mechanism, Wait (1966) further pointed out that Bragg peaks amplitudes are related to the sea state. Barrick (1972a) extended the study of first-order solution for scatter for a perfectly conducting random surface. In deep water condition with no ocean current, he derived vertically polarized first-order radar cross section written as the average scatter cross section per unit area per rad/s bandwidth

$$s^{(1)}(2pf) = 2^6 p k_0^4 \sum_{m_1=\pm 1} S(-2m_1 k_0) d(f - m_1 f_B) \quad (2-9)$$

with f the Doppler frequency, k_0 the radar wave number vector, S the directional ocean wave spectrum, d the Dirac function, m_1 the sign indicator which is ± 1 . The signs indicate two first-order peaks symmetrically located, the Bragg peaks. Eq. (2-9) also demonstrates that the amplitudes of Bragg peaks are proportional to ocean wave spectrum at frequency of Bragg waves.

Using boundary perturbation theory in Maxwell's electromagnetic equation and Navier-Stokes hydrodynamic equations give the second-order solution. The second-order sea echo appears in a Doppler spectrum as four continuous side bands placed distinctly surrounding the two first-order Bragg peaks. This phenomenon is interpreted as the interaction between the incident radio wave and two trains of ocean waves. Ocean waves, which create second-order scattering, with wave number vectors \vec{K}_1 , \vec{K}_2 and frequencies F_1 and F_2 , are "bound" Bragg waves constrained by

$$\vec{K}_1 + \vec{K}_2 = -2\vec{k}_0 \quad (2-10)$$

The relationship between radio wave and ocean waves is shown in Fig. 2-1.

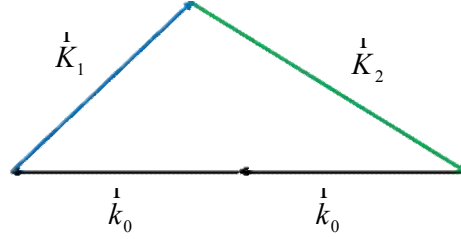


Fig. 2-1 The relationship between radar wave and the two ocean waves which cause second-order Bragg scattering.

This interaction creates the less significant continuous component around Bragg peaks in the Doppler spectrum. Barrick (1972b) derives the expression of second-order radar cross section per unit area:

$$S^{(2)}(2pf) = 2^6 p k_0^4 \sum_{m_1, m_2 = \pm 1} \int \int_{-\infty}^{\infty} |\Gamma|^2 S(m_1 K_1^p) S(m_2 K_2^p) d(f - m_1 F_1 - m_2 F_2) dK_2^p \quad (2-11)$$

with Γ the coupling coefficient, which is a sum of electromagnetic and hydrodynamic terms; m_2 is a sign indicator ± 1 . Different combinations of sign indicators (m_1 and m_2) envelope different regions in the Doppler spectrum, numbered by j :

$$f < -f_B \quad (j=1, m_1=-1, m_2=-1);$$

$$-f_B < f < 0 \quad (j=2, m_1=-1, m_2=1);$$

$$0 < f < f_B \quad (j=3, m_1=1, m_2=-1);$$

$$f > f_B \quad (j=4, m_1=1, m_2=1).$$

The spectral amplitudes are used in normalized form in order to remove potential unknown system gains and path losses in the received signal. The normalized second-order spectral energy is defined as the integration of second-order spectrum over the integration of its neighboring Bragg peak spectrum

$$R = \frac{\int_{f-d_{w2}}^{f+d_{w2}} S^{(2)}(f)df}{\int_{f-d_{w1}}^{f+d_{w1}} S^{(1)}(f)df} \quad (2-12)$$

with d_{w1} and d_{w2} denoting finite Doppler frequency widths over which the considered first- and second-order spectrum is integrated, respectively. If there is no frequency smearing, this quantity goes to the expression of the second-order radar cross section normalized by the energy of first-order Bragg peak.

A typical qualified hourly radar Doppler spectrum is shown in Fig. 2-2. Bragg peaks, at frequencies $\pm f_B$, and swell peaks, indicated in shadow, are the first- and second-order characteristics, respectively. The surrounding second-order continuum often exhibits sharp peaks at $\pm\sqrt{2}f_B$ and $\pm 2^{3/4}f_B$. These peaks, called second harmonic and corner reflection peaks, are caused by singularities in $S^{(2)}$ of hydrodynamic and electromagnetic origins, respectively (Barrick 1972b; Ivonin et al. 2006). Due to possible spurious instrumental peaks, the central part of the spectrum is masked. And only spectral amplitudes of 3 dB above noise level are considered (see Section 3.4 below).

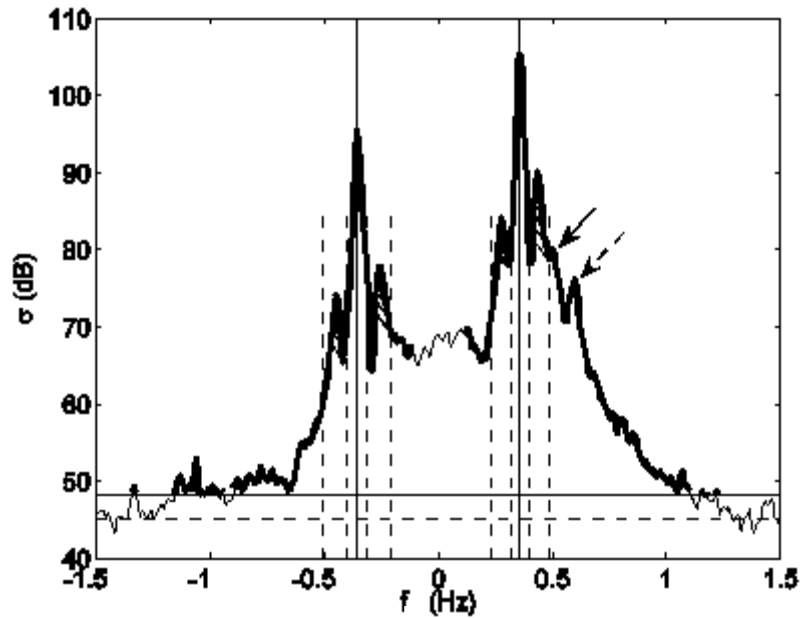


Fig. 2-2 A typical hourly-averaged Doppler spectrum after de-shifting procedure. The two solid vertical lines are $\pm f_B$. The eight dashed vertical lines envelope the four searching intervals for swell peaks. The identified swell peaks are shadowed. The

dashed horizontal line is the noise level, while the solid line indicates 3 dB above noise level. The spectrum considered for analysis is shown in heavy line. Arrows point second harmonic (full) and corner reflection (dashed) spectral peaks.

2.2 Methods for the inversion of surface current

It was shown in Section 2.1 that Bragg frequencies are determined by radar transmitting frequency. However, this is based on the assumption that there are no surface currents. However, in practice the measured Bragg peaks are often displaced from the ideal positions. This additional displacement of Doppler frequency is due to the existence of surface current and is called current-induced Doppler shift, Df . A positive Doppler shift indicates a radial current velocity component towards the radar; a negative Doppler shift indicates a radial current velocity component off the radar. Fig. 2-3 shows a case of positive Doppler shift caused by surface current. This Doppler shift applies to all the Doppler frequencies. In an experimental Doppler spectrum, Df is measured via the more energetic first-order peak. The radial current velocity is computed by

$$v_{cr} = \frac{1 Df}{2} \quad (2-13)$$

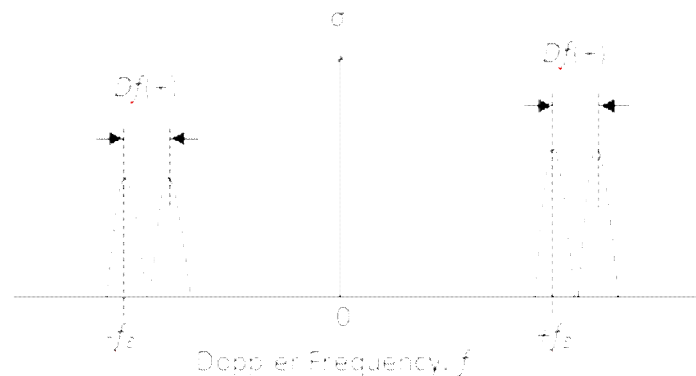


Fig. 2-3 Doppler shift (Df) induced by ocean surface current moving towards radar. The two dashed and solid curves show Bragg peaks in ideal positions and shifted by current, respectively.

While a single radar station measures only radial component, the combination of two or more radar stations gives surface current vector following the vector law, Fig. 2-4. In the figure, it is assumed that the real current moves in the direction a , with total velocity v_c . The radial components measured in two different radar beams at angles a_1 and a_2 , respectively, are v_{cr1} and v_{cr2}

$$v_{cr1} = v_c \cos(a - a_1) \quad (2-14)$$

$$v_{cr2} = v_c \cos(a - a_2) \quad (2-15)$$

The combination of these equations gives the direction of current

$$a = \arctan \frac{v_{cr1} \cos a_2 - v_{cr2} \cos a_1}{v_{cr2} \sin a_1 - v_{cr1} \sin a_2} \quad (2-16)$$

and the velocity of current in three forms

$$v_c = \frac{v_{cr1}}{\cos(a - a_1)} \quad (2-17)$$

$$v_c = \frac{v_{cr2}}{\cos(a - a_2)} \quad (2-18)$$

$$v_c = \frac{1}{2} \left[\frac{v_{cr1}}{\cos(a - a_1)} + \frac{v_{cr2}}{\cos(a - a_2)} \right] \quad (2-19)$$

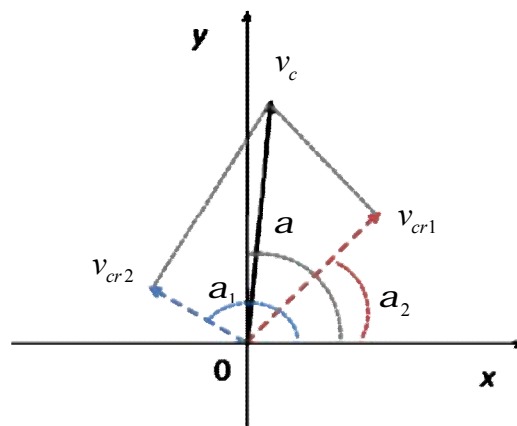
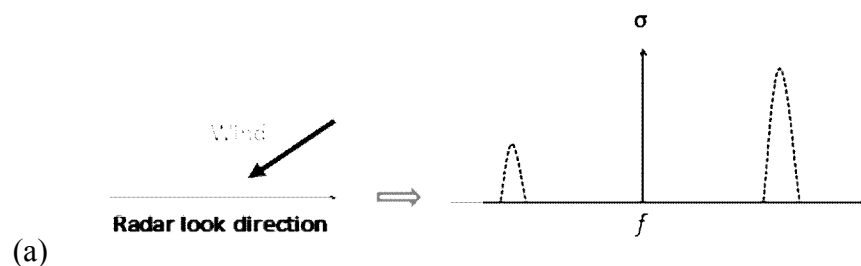


Fig. 2-4 Measurement of current vector using two radar stations.

Radar coverage is divided into small cells where current velocity is determined by least-squares method (Lipa and Barrick, 1983). Usually, the distance between two radar stations is designed to be 1/3-2/3 of the farthest distance of radar detection. At the same time the angle between normal radar beams should not be too small. Radar stations are required to be deployed in capes or islands far off land. However, in practice, the limitations of topography make it difficult to fully satisfy the conditions of installation. Accuracy of current measurement can be improved by increasing the number of radar stations.

2.3 Methods for the inversion of wind direction

Wind direction can be estimated using the spectral density of the two Bragg peaks through methods fitting directional ocean wave distribution models to radar measurements of spectral density of Bragg peaks (Long and Trizna 1973; Wyatt et al. 1997; Cochin et al. 2005; Gurgel et al. 2006). These approaches are based on two basic assumptions. One is that the surface waves are generated only by local wind and have reached equilibrium. The other is that the direction distribution model used in the description of Bragg waves is correct. Fig. 2-5 shows the correspondence of wind direction and energy of Bragg peaks. When the wind blows towards radar, energy of positive Bragg peak is larger than that of negative Bragg peak. When the wind blows off radar, energy of positive Bragg peak is less than that of negative Bragg peak. When the wind blows perpendicular to radar beam, the two Bragg peaks have sizable energy.



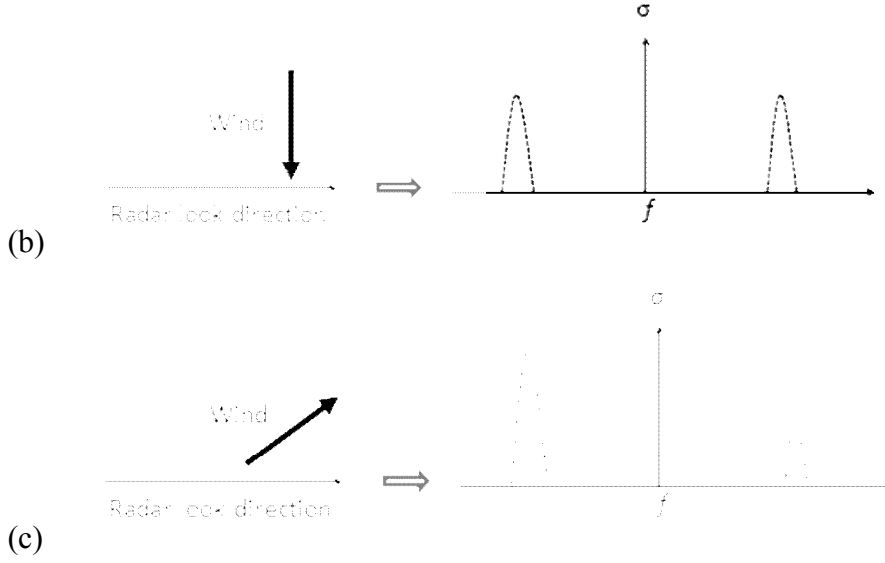


Fig. 2-5 The correspondence between surface wind direction and energy of Bragg peaks in the Doppler spectrum. (a) Up wind. (b) Cross wind. (c) Down wind.

Bragg peaks ratio is defined as the ratio of spectral energy density of positive and negative Bragg peaks, B^+ and B^- , respectively,

$$R_B = B^+ / B^- \quad (2-20)$$

Following Eq. (2-9), the ratio can be expressed by ratio of Bragg waves' energy.

$$R_B = \frac{s^{(1)}(2pf_B)}{s^{(1)}(-2pf_B)} = \frac{S(-2\hat{k}_0)}{S(2\hat{k}_0)} \quad (2-21)$$

with $S(\hat{K})$ the ocean wave spectrum for wave component with wave number vector \hat{K} (modulus K). Bragg waves are short waves with directions mainly determined by wind direction. The directional wind wave spectrum can be expressed by the multiplication of a non-directional spectrum, y , multiplied by a directional factor, G ,

$$S(\hat{K}) = y(K)G(K, q) \quad (2-22)$$

with q the relative direction of wave component \hat{K} with respect to direction of maximum energy which is usually the wind direction for wind waves.

There are several distribution forms of the directional factor proposed by previous research. They can be divided into two groups: one assumes that all wave components have a same form of directional distribution and that $G(q)$ is function of direction only; the other considers different directional distributions for different

wave components and that $G(K, q)$ is function of both wave number and direction. One classical model is the one proposed by Longuet-Higgins et al. (1963)

$$G(K, q) = G'(K) \cos^{2s} \left(\frac{q}{2} \right) \quad (2-23)$$

with $G'(K)$ a normalization function which makes the formula satisfy $\int_{-p}^p G(K, q) dq = 1$; s the spreading parameter which is a function of K . The spreading parameter describes the degree of dispersion of energy with direction. The bigger value of s indicates the more focus of wave energy around the wind direction. Tyler et al. (1974) proposed an improved model of Eq. (2-23) which allows a small wave energy flux against the wind direction

$$G(q) = G'(K) [a + (1-a) \cos^s \left(\frac{q}{2} \right)] \quad (2-24)$$

with a the fraction of wave energy travelling opposite to the prevailing wind. Cochin et al. (2005) applied the model of Eq. (2-24) into Eq. (2-21) and obtained

$$R_B = \tan^s \left(\frac{q}{2} \right) \quad (2-25)$$

The direction here is the relative direction of negative Bragg waves with respect to wind direction, i.e. the angle between radar look direction and wind direction. There is ambiguity in the relative direction. Stewart and Barnum (1975) also applied the cardioid directional distribution and obtained a same form of relationship as Eq. (2-25) with a spreading parameter as large. Using the original Longuet-Higgins model gives a similar relationship with spreading parameter equal to 1/2 of s in Eq. (2-25). These three are all cardioid-based models.

Donelan et al. (1985) studied 14 wave staffs and proposed a hyperbolic secant squared shaped directional distribution for the ocean wave spectrum

$$G(K, q) = \frac{b}{2} \operatorname{sech}^2(bq) \quad (2-26)$$

with b the directional spreading parameter which is a function of wave number and peak frequency. By this model, the Bragg peaks ratio is expressed as

$$R_B = \frac{\operatorname{sech}^2[b(p-q)]}{\operatorname{sech}^2(bq)} \quad (2-27)$$

Long and Trizna (1973) obtained the relationship for winds of a storm at long range over a large area

$$r_B = 20 \log \left(\frac{0.56 + 0.5 \cos 2q}{p} \right) + 34.02 \text{ dB} \quad (2-28)$$

with $r_B = 10 \log_{10}(R_B)$ the Bragg peaks ratio in dB. From tests during twelve days by OTH radar, Harlan and Georges (1974) proposed a linear relationship

$$q = 3.75r_B + 90^\circ \quad (2-29)$$

These directional distribution models are shown in Fig. 2-6.

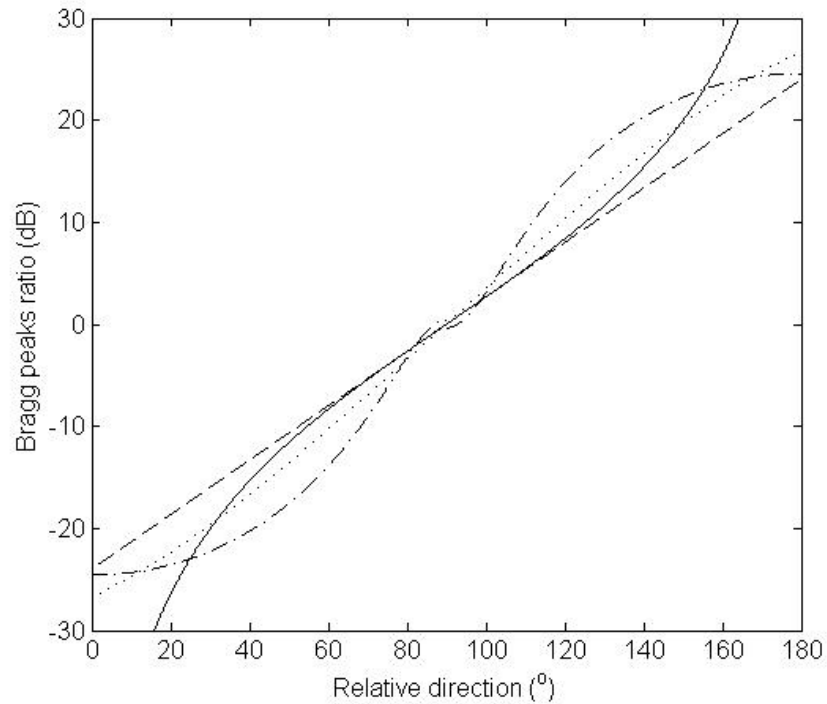


Fig. 2-6 Several models for Bragg peaks ratio as a function of relative radar look direction with respect to wind direction. Dashed line: linear model by Harlan and Georges (1974), Eq. (2-29). Dot dashed line: model by Long and Trizna (1973), Eq. 2-28. Dot line: Hyperbolic secant squared model by Donelan et al. (1985) with a spreading parameter of 1.2, Eq. 2-27. Solid line: cardioid model by Tyler et al. (1974) with a spreading parameter of 3.5 (Eq. 2-25).

It should be noted that the theoretical models (cardioid model or hyperbolic secant squared model) cannot be applied to frequencies above 1.5 times the peak frequency and below 0.6 times the peak frequency. Further investigations have concerned the computation of wind speed. Stewart and Barnum (1975) proposed a linear relationship between peak width and wind speed. They measured the slope and intercept from a limited number of experimental results. Dexter and Theodoridis (1982) proposed another way to invert wind speed from second-order Doppler spectra.

This approach is based on empirical relationship between wind and surface waves. Shen et al. (2012) recommended a hybrid of first- and second-order methods.

However, these models proposed by previous work are not sufficiently reliable for operational use and require validation for different directional distributions and wind conditions (Wyatt 2005). There are many factors contributing to the broadening of Bragg peaks other than wind velocity, such as noise. These factors are mostly unpredictable and all lead to inaccuracies of the derivation of wind velocity. Also, the measurement of wind is greatly related to the sea states. The correspondence between Bragg waves and wind varies for different wavelengths. Harlan and Georges (1994) showed that for wind speed of 8 m/s, Bragg waves with wavelength of 10 m need 36 min to fully adjust to a significant variation of wind direction.

2.4 Methods for the inversion of swell

Barrick (1977a) proposed an approximate approach to derive ocean surface non-directional wave spectrum after the work of Hasselmann (1971). His analysis is based on the study of the sea state by Phillips (1966) and Tyler et al. (1974). The total ocean wave spectrum can be expressed by Eq. (2-22). The non-directional wave spectrum can be expressed by (Phillips 1966)

$$y(K) = \frac{0.005}{2pK^4} \quad (2-30)$$

With a spreading factor of 2 in Eq. (2-23), the direction distribution factor takes the form (Tyler et al. 1974)

$$G(q) = \frac{4}{3} \cos^4\left(\frac{q}{2}\right) \quad (2-31)$$

Barrick (1977b) simplified the complex coupling coefficient in the radar cross equation into a weighting function, w ,

$$w(2pf_n) = \frac{\overline{8|\Gamma|^2}}{k_0} \quad (2-32)$$

with $f_n = f / f_B$ the Doppler frequency normalized by Bragg frequency. Thus the weighted second-order radar cross equation can be integrated over Doppler frequency

$$\int_{-\infty}^{\infty} \frac{\mathbf{s}^{(2)}(f)}{w(f/f_B)} df \approx 2^6 p k_0^6 h^2 S' \quad (2-33)$$

with h the root-mean-square (RMS) waveheight; S' a term related with ocean wave spectrum. Dividing the second-order spectrum by first-order spectrum, this term is eliminated and the equation for computing the RMS waveheight is derived

$$h^2 = \frac{\int_{-\infty}^{\infty} [S^{(2)}(f) / w(f / f_B)] df}{k_0^2 \int_0^{\infty} S^{(1)}(f) df} \quad (2-34)$$

Barrick (1977a) gives the closed form equation for total non-directional ocean wave spectrum

$$S_0(f_B | f_n - 1) = \frac{4S^{(2)}(f_B f_n) / w(f_n)}{k_0^2 \int_0^{\infty} S^{(1)}(f) df} \quad (2-35)$$

The mean wave period can be obtained by

$$T = \frac{2p \int_{0,1}^{1,\infty} [S^{(2)}(f_B f_n) / w(f_n)] df}{k_0^2 \int_{0,1}^{1,\infty} [|f_n - 1| S^{(2)}(f_B f_n) / w(f_n)] df} \quad (2-36)$$

Barrick (1977b) demonstrated both by theoretical analysis and by experimental results that this approach reached reasonable accuracy after the approximation adopted. Results showed that the threshold of 1 can be replaced by 0.3 to improve the accuracy of significant waveheight to 23% and the accuracy of mean wave period to 12%. Fig. 2-7 shows that in the normalized Doppler frequency range of 0.5 - 1.5 Hz, the weighting function is close to 1. Barrick (1977b) also showed that the accuracy varies with radar look direction.

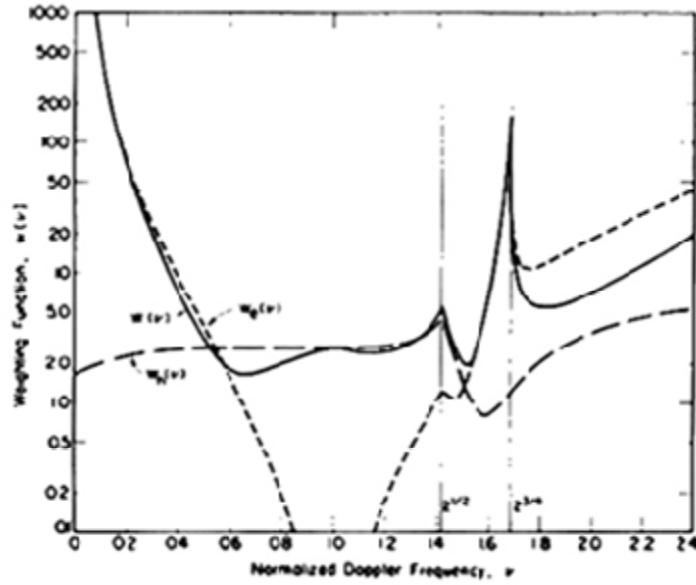


Fig. 2-7 Weighting function versus normalized Doppler frequency given by Barrick (1977b). Solid line is the total weighting function; short dashed line is the contribution of electromagnetic coupling coefficient; long dashed line is the contribution of hydrodynamic coupling coefficient.

The correspondence between Doppler spectrum and ocean wave spectrum is very complex as shown above. However, the swell case is more straightforward. For a typical swell with frequency of 0.08 Hz, the correspondent normalized Doppler frequency in Fig. 2-7 obtained by our radar system is 0.78 and 1.22, within the interval where the weighting function is nearly constant. When there is a single swell coming from offshore, the ocean wave spectrum can be considered as the summation of local wave spectrum, S_w , and the swell spectrum, S_s . Assuming the swell unidirectional and narrow-banded, the swell spectrum can be expressed by an impulse function

$$S_s(\vec{K}) = h_s^2 d(\vec{K} - \vec{K}_s) \quad (2-37)$$

with h_s the RMS waveheight of swell, and \vec{K}_s the swell wave number vector with module K_s . Integrating the Dirac function gives the total swell energy

$$\iint_{-\infty}^{\infty} S_s(\vec{K}_s) d\vec{K}_s = h_s^2 \quad (2-38)$$

Assuming $\vec{K}_2 = m_2 \vec{K}_s$, the integration equation (2-11) becomes

$$S^{(2)}(2pf) = 2^7 p k_0^4 h_s^2 |\Gamma|^2 S(2k_0 - K_s) d(f - m_1 F_1 - m_2 F_s) \quad (2-39)$$

with F_s the swell frequency; F_1 can be obtained from the constraint of wave numbers.

2.4.1 Swell frequency

The Doppler frequencies of the swell peaks are obtained by solving the Dirac function:

$$f_1 = -f_B (1 + F_s^4 / f_B^4 - 2F_s^2 \cos q_s / f_B^2)^{1/4} - F_s \quad (2-40)$$

$$f_2 = -f_B (1 + F_s^4 / f_B^4 + 2F_s^2 \cos q_s / f_B^2)^{1/4} + F_s \quad (2-41)$$

$$f_3 = +f_B (1 + F_s^4 / f_B^4 - 2F_s^2 \cos q_s / f_B^2)^{1/4} - F_s \quad (2-42)$$

$$f_4 = +f_B (1 + F_s^4 / f_B^4 + 2F_s^2 \cos q_s / f_B^2)^{1/4} + F_s \quad (2-43)$$

with q_s the angle between swell propagation direction and radar beam, called relative swell direction, Fig. 2-8.

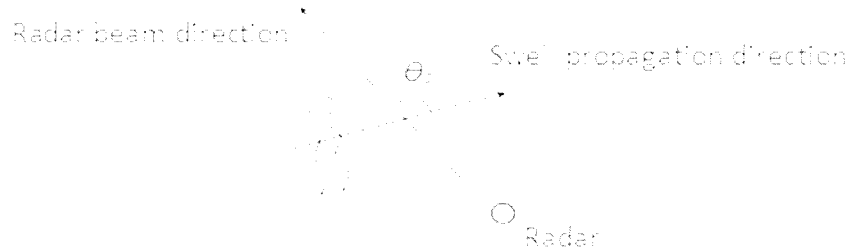


Fig. 2-8 Relative swell direction.

Forget et al. (1981) expanded the expressions and simplified them:

$$f_1 = -f_B + \frac{F_s^2}{2f_B} \cos q_s - F_s \quad (2-44)$$

$$f_2 = -f_B - \frac{F_s^2}{2f_B} \cos q_s + F_s \quad (2-45)$$

$$f_3 = f_B - \frac{F_s^2}{2f_B} \cos q_s - F_s \quad (2-46)$$

$$f_4 = f_B + \frac{F_s^2}{2f_B} \cos q_s + F_s \quad (2-47)$$

These four equations have two unknowns, swell frequency and direction. Straightforward combinations of the four equations above yield solutions of the two unknowns independent of each other:

$$F_s = \frac{1}{4}(\Delta f^+ + \Delta f^-) \quad (2-48)$$

$$q_s = \cos^{-1} \left[\frac{8f_B(\Delta f^+ - \Delta f^-)}{(\Delta f^+ + \Delta f^-)^2} \right] \quad (2-49)$$

with Δf^- and Δf^+ the frequency differences between the swell peak positions on the negative and positive parts of the Doppler spectrum, respectively, i.e. $\Delta f^- = f_2 - f_1$, and $\Delta f^+ = f_4 - f_3$.

2.4.2 Swell waveheight

Swell peak energy is used in normalized form in order to eliminate multiplicative gains and losses. The normalized energy is defined as the ratio of the swell peak energy to that of its neighboring Bragg peak. The expressions of R for $j=1\sim 4$ swell peaks are given by

$$R = \frac{\int_{f-2df}^{f+2df} \mathbf{S}^{(2)}(f) df}{\int_{f-2df}^{f+2df} \mathbf{S}^{(1)}(f) df} = 2h_s^2 |\Gamma|^2 C \quad (2-50)$$

with df the resolution of Doppler frequency, and C a residual term related to the spectrum of the ocean wave background, typically wind waves.

$$C = \frac{S_w(-2m_1 k_0 - m_1 m_2 K_s)}{2^6 p k_0^4 S_w(-2m_1 k_0)} \quad (2-51)$$

At HF radar frequencies the swell wavenumber satisfies $K_s \ll k_0$. Using the Pierson-Moskowitz wave spectrum model we obtain with good approximation

$$C \approx (1 + (K_s / k_0)^2 / 4 + m_1 K_s \cos q_s / k_0)^{-2} \quad (2-52)$$

Lipa and Barrick (1986) once considered C as a constant equal to 1.

Eq. (2-50) implies that R is theoretically valued by three parameters: F_s and q_s in the expression of Γ and C , and h_s . Figure 2-9 shows the relationship between R and each of the three parameters, given typical values of the other two parameters. The simulated R_1 (R_2) shows similar features as R_3 (R_4). Fig. 2-9 (a) shows that the left pair (R_1 and R_3 , located left to neighboring Bragg peaks) decrease with swell frequency while the right pair (R_2 and R_4) increase. The dependences of R upon F_s are almost linear. Swell peaks' energy increases with swell waveheight following a parabolic function. h_s is generally the major contribution to R when it exceeds 0.25 m. R decreases when swell direction changes from parallel to perpendicular to radar beam. The left pair shows a higher (lower) rate of variation than the right pair when swell moves off (towards) the radar. There is a singularity when swell moves across radar beam (Ivonin et al. 2006). The singularity in cross swell direction affects larger range for shorter swell cases. For this reason, we ignored relative swell direction ranging from 65° to 115° in our computations.

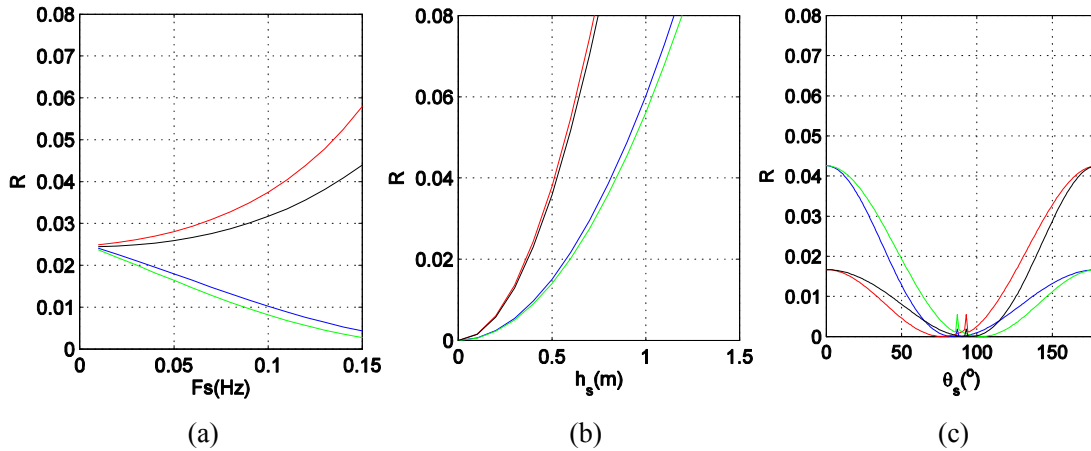


Fig. 2-9 Normalized swell peak energy (unit: dB) as function of (a) swell frequency, with $q_s = 160^\circ$ and $h_s = 0.5m$. (b) swell RMS waveheight, with $F_s = 0.08Hz$ and $q_s = 160^\circ$. (c) swell relative direction, with $F_s = 0.08Hz$ and $h_s = 0.5m$. Colors of blue, red, green and black denotes simulated $R_1 \sim R_4$, accordingly.

Given measurements of normalized swell peak energy, r , Eq. (2-50) provides a method to estimate the swell waveheight from single swell peak. Lipa et al. (1981)

proposed a least-squares method. The sum of squares of residuals between r and the theoretical prediction R writes

$$Q = \sum_{j=1:4} (r_j - R_j)^2 \quad (2-53)$$

Values of r were obtained by integrating over five spectral points in the vicinity of the swell peaks and dividing the result by the energy of the neighboring Bragg peak. With four qualified swell peaks available, a least-squares fitting of theoretical and measured peak energy was performed to invert swell waveheight. Lipa et al. (1981) proposed such kind of a maximum-likelihood analysis to solve both h_s and q_s at the same time.

However, we found in practice that inversion of two unknowns often leads to outliers. There are at least three reasons for this: (i) multiple solutions to the problem; (ii) R is more sensitive to H rather than to q_s ; (iii) uncertainty in the measurement of r . Instead, h_s is considered as the only unknown and q_s is determined by other methods, like Eq. (2-49). The least-squares minimization approach requires that the partial derivative of Q with respect to h_s is zero, which yields

$$H_s^2 = \frac{8 \sum_{j=1:4} r_j |\Gamma_j|^2 C_j}{\sum_{j=1:4} |\Gamma_j|^4 C_j^2} \quad (2-54)$$

with $H_s = 4h_s$ the significant waveheight of swell.

The ability of HFR for measurement of direction is quite limited. Figure 2-10 investigates the influence of the inaccuracy of radar-inverted relative swell direction, q_{sr} , on radar-inverted swell significant waveheight, H_{sr} , for different swell conditions. Real relative swell direction, $q_{s,true}$, varies from 0° to 180° . Input values of $F_{s,true}$ and $H_{s,true}$ are 0.08 Hz and 2 m, respectively. Generally, the figure shows that an overestimation (underestimation) of the input of q_s in Eq. (6) leads to an underestimation (overestimation) of H_{sr} measurement. For example, for the swell case with true relative direction of 140° , the variation of q_{sr} from 130° to 160° leads to $\pm 20\%$ of uncertainty in H_{sr} .

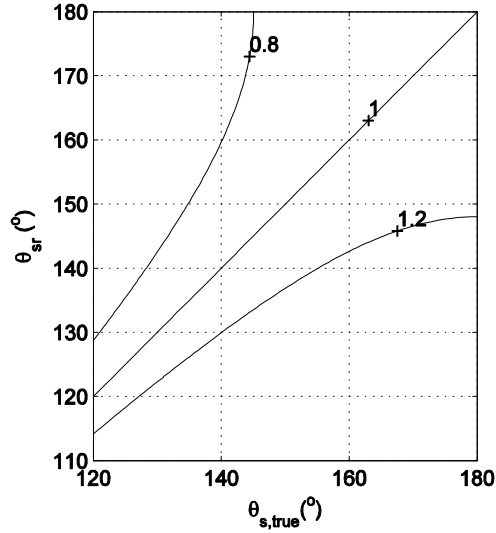


Fig. 2-10 Accuracy of inverted swell significant waveheight with respect to values of relative swell direction under different conditions of swell direction. Swell frequency takes a typical value of 0.08 Hz. Contours show inverted swell significant waveheight normalized by its input value.

It is noteworthy that the validity of Eqs. (2-9, 2-11) is submitted to the validity of the small perturbation theory underlying these equations. This requires that the RMS swell waveheight is smaller than $1/k_0$ (Lipa et al. 1981). In practice, a factor of 0.3 instead of 1 offers the highest significant wave height which can be measured using the second-order perturbation theory

$$H_{s,\max} = 1.2/k_0 \quad (2-55)$$

For our radar system with transmitting frequency of 12.35 MHz, the radar ability for swell significant waveheight is $H_{s,\max} = 4.6$ m.

2.4.3 Relative swell direction

There are two approaches to obtain relative swell direction using spectra from single radar station. The first one calculates q_s from swell peaks' Doppler frequencies using Eq. (2-49) and is called POS method. The second one is a least-squares fitting method and is called LS method. In the LS method, results from Eqs. (2-48, 2-54) are substituted in Eq. (2-53) and q_s is then the only unknown to be solved.

Fig. 2-11 shows an example of the variation of the residual term Q with q_s .

Swell parameters are $F_{s,true} = 0.08$ Hz, $H_{s,true} = 2$ m, $q_{s,true} = 140^\circ$. Radar observation of this swell, r , is simulated by Eq. (2-49). The method finds a “flat” minimum in the right place. Studies of different swell conditions showed that the more nearly parallel the swell direction is with respect to radar beam, the less evident the minima of Q behaves in Fig. 2-11. This is because of the fact that q_s functions in cosine form in the expression of coupling coefficient. Similar feature is found in Fig. 2-9 (c).

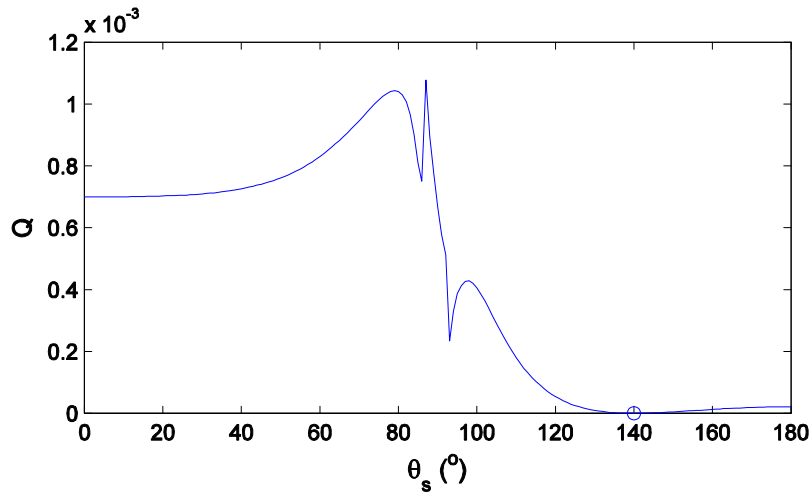


Fig. 2-11 Residual term Q (Eq. 2-53) as function of q_s in the LS method under a typical swell condition with $F_{s,true} = 0.08\text{Hz}$, $H_{s,true} = 2\text{ m}$, $q_{s,true} = 140^\circ$. The circle shows the solution found by the least-squared method.

However, a 180° ambiguity exists in q_s because of the cosine functions in the theoretical relationships. For overlapped radar coverage, two radar measurements are available. The two are collected nearly simultaneously (less than 20 min, Section 3.1). It is thus possible to solve the ambiguity and obtain absolute swell direction, q_{sa} .

The methods for the inversion of swell direction are based on the assumption of the unique unidirectional property of the swell (Dirac function). However, the directional spreading of swell might be complicated. To look at the impact of swell directional spreading, we have performed simulations of the Doppler spectra using the simulator developed by Grosdidier et al. (2014). It is observed that that the broadening of the swell directional spreading contributes to amplify only slightly the energy of the swell peaks (r) in the Doppler spectrum. This leads to just a small increase of swell waveheight computed by Eq. (2-54). Varying swell parameters (direction,

waveheight and wave number) doesn't change this conclusion. An eventual azimuthal spreading of the swell spectrum does not significantly affect our estimation of swell waveheight. This holds for spreading angles lower than 40° .

3 Radar data processing

3.1 Locations and radar parameters

The study area is the Iroise Sea, West of France, Fig. 3-1. It locates at the east of the Atlantic Ocean. It is subject to frequent storms generated in the central vast ocean, especially in winter. Water depths vary gradually from 50m to 150 m. In front of station R2, there is a group of islands, Molène archipelago. To its northwest, there is a bigger isolated island, Ushant Island. There is a 2 km wide strait, Fromveur strait, between the Molène archipelago and the Ushant Island. In the southern part, there is Sein archipelago to the west of station R1.

The radar system consists of two monostatic HF radars on the west coast of Brittany, deployed by SHOM (Oceanographic Division of the French Navy). The radars collect data over the Iroise Sea. Individual radar stations locate at Cape Garchine (site R1) and Cape Brezellec (site R2), Fig. 3-1. The two stations separate 50 km from each other, with an angle of 41° between their central radar beams. There is sufficient overlapped common coverage.

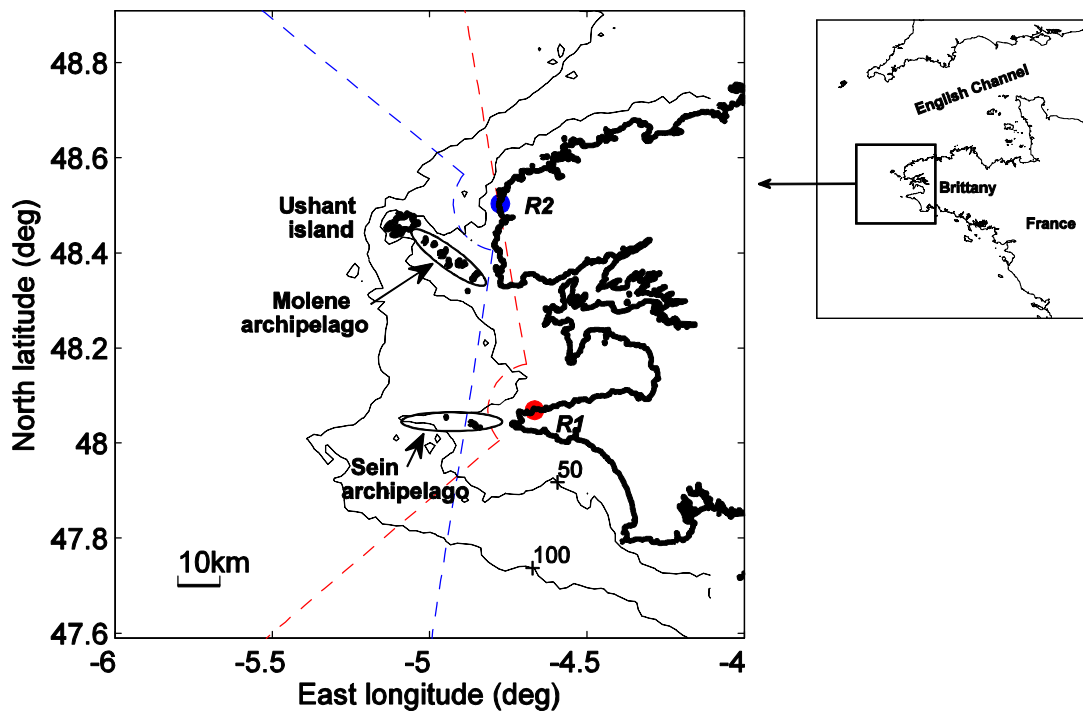


Fig. 3-1 Location of radar sites. Red and blue dashed lines envelop the azimuthal coverage. Dashed arcs indicate the first range of R1 and R2, respectively. Isobaths of

50 m and 100 m are shown.

The radars are WERAs (Wellen Radar) designed by Gurgel et al. (1999) and manufactured by Helzel Messtechnik GmbH (Germany). The radar system has been collecting radar data continuously in the Iroise Sea since 2006. They have operationally provided observations of sea surface currents at high temporal and spatial resolutions (e.g., Ardhuin et al. 2009a; Muller et al. 2010; Sentchev et al. 2013). Important radar parameters are described in Table 3-1.

Items	station R1	station R2
Central frequency (MHz)	12.34	12.35
Range resolution δ_r (km)	1.5	
Azimuth resolution (°)	5	
Number of processed range cells	23	
Number of processed azimuth cells	25	
Number of chirps	2048	
Chirp duration (s)	0.26	
Acquisition time per hour (min)	10, 30, 50	00, 20, 40
Period of database	September 1, 2007 – September 30, 2008	

Table 3-1 Radar parameters chart.

The receiving array is parallel to the shore line and consists of 16 equally spaced antennas aligned over 150m. Radars transmit frequency-modulated continuous wave chirps. Both radar transmitting frequencies vary very little around 12.35 MHz. The 3-dB aperture is 9° for the beam normal to the antennas array. There are three acquisitions for both radars within every hour: 10 min, 30 min, 50 min for station R1; 0 min, 20 min, 40 min for station R2. Each acquisition includes 2048 chirps with chirp duration of 0.26 s. Contrary to other HF radar techniques, typically the CODAR technique, the WERAs provide a narrow beam, which is allowed by the long

receiving antenna array and by the use of the beam-forming processing technique. Processed radar ranges extend from 11 km to 149 km every 6 km; Azimuths are processed every 5° from -60° (clockwise) to 60° (counterclockwise) with respect to the central radar beam. The dataset used in this thesis expands from September 1, 2007 to September 30, 2008.

3.2 Beam forming

WEAR system operates up to 16 receive antennas. With 16 antennas, WERA allows the beam forming technique. The antenna configuration is linear as received signals come from a semicircle from the coast. Beam forming weights and combines phase-shifted signals of antennas, creating constructive interference in the desired direction.

Effect of beam forming with our radar system by theoretical calculation based on the antennas positions is shown in Fig. 3-2. On the normal beam, the side lobes contribute little to the received signals. On the radar beam at 50° (60°) to normal beam, the comparable contributions come from side lobe at 80° (60°) to the specific beam, Fig. 3-3. For station R2, the impact of side lobes becomes severe on radar beams at over 50° , because side lobes bring information from the open ocean surface in the north where it is supposed to have other energetic swell events.

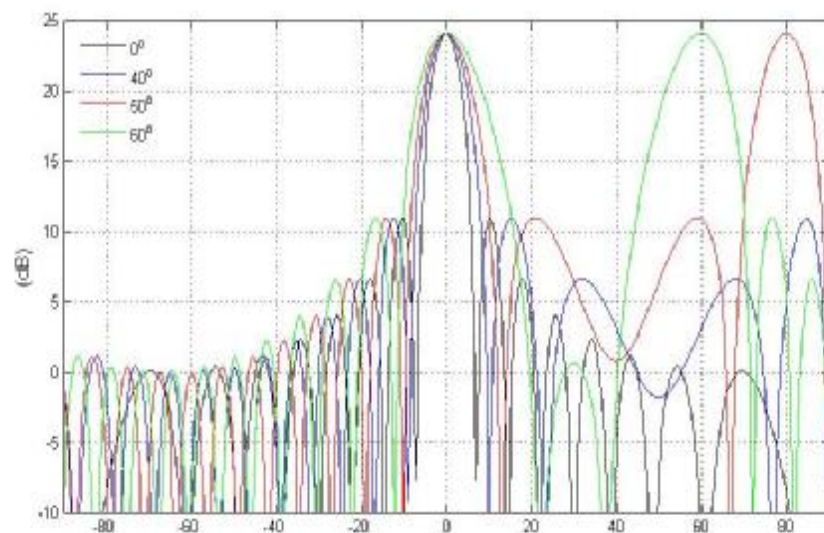


Fig. 3-2 Array pattern for the 16-element WERA system. Black, blue, red and green curves show patterns on radar beams of 0° , 40° , 50° and 60° with respect to the

normal beam, separately. Each pattern is shifted by the relative direction of the beam to locate its central lobe at 0° in the figure.

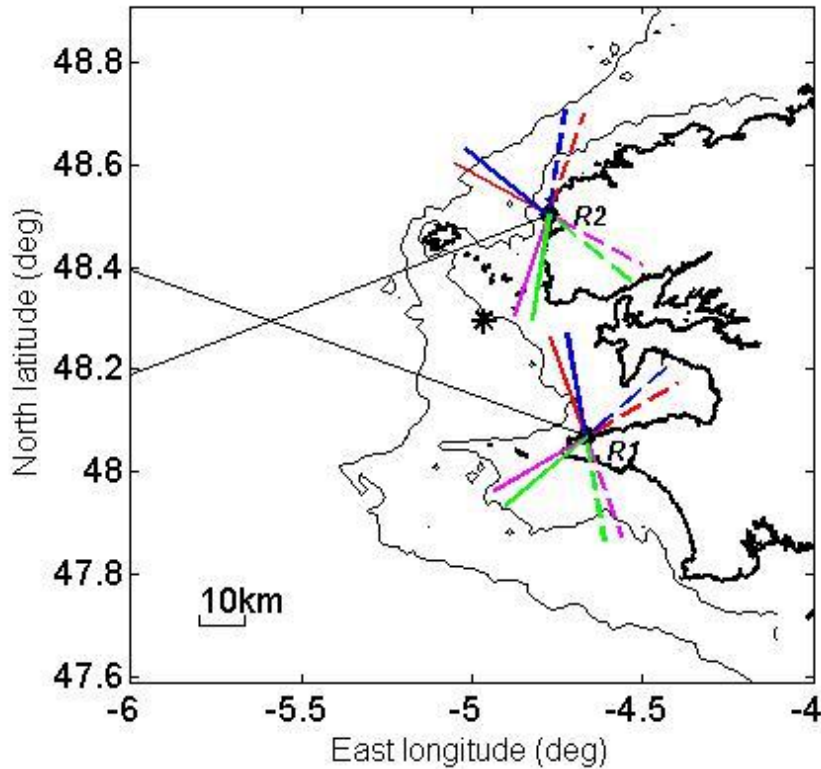


Fig. 3-3 Directions of significant side lobes in the map. Black lines show the normal beams. Blue, red, mauve and green solid lines indicate radar beams at -60° , -50° , 50° and 60° with respect to the normal beams. Dashed lines show the directions of corresponding significant side lobes.

3.3 Averaging of Doppler spectra

Due to randomness of the ocean surface and the electromagnetic scattering, there are lots of fluctuations in the measured radar signals. It is then necessary to perform appropriate smoothing or averaging in order to emphasize the desired spectral features for certain aims. Barrick and Snider (1977) demonstrated that the sea echo voltage spectrum obeys c^2 distribution after averaging. If radar transmit frequency is greater than 10MHz Doppler spectra from different range cells which separate more than 3 km are statistically independent. It is suggested that at least 10 spectra are

incoherently averaged in practice for the following analysis of the spectra. Based on these previous studies, this thesis processed spatial and temporal averaging for Doppler spectra.

The raw sea-echo record for each acquisition consists of 2048 chirps and spans 532.48 s. We divided it into $N_s = 4$ consecutive subseries and obtained initial Doppler spectra using fast Fourier transform (FFT). It was illustrated in Barrick and Snider (1977) that the Doppler spectra samplings are uncorrelated when the duration of signals is greater than 25 s. Thus the first step of averaging was done by incoherent summation of the spectra calculated from these subseries. The duration of each subseries was $T_t = 512 \times 0.26 = 133.12$ s, giving a Doppler frequency resolution

$$df = \frac{1}{T_t} = 0.0075 \text{ Hz} \quad (3-1)$$

To eliminate spatial dependence between neighboring radar cells, the second averaging process was performed over $N_c = 4$ neighboring range crowns. This gives an effective range resolution of $\delta = 4\delta_r = 6$ km and 23 range cells per azimuth.

Finally, concerning swell characteristics, a temporal averaging is performed to minimize wind wave characteristics in the spectra. Wind waves are often studied in an interval of 20 min while an interval of 1 hour is often considered for the study of swell. Thus, a number of $N_h = 3$ qualified spectra per hour were summed up to produce hourly spectra (Table 1).

In total, the averaged spectrum results from $N_{sum} = N_s \times N_c \times N_h = 48$ incoherent summations. Assuming Gaussian statistics for real and imaginary parts of voltage signal output (Barrick 1980), spectral amplitudes have 96 degrees of freedom.

However, surface currents may vary during this period, especially in this coastal region which is known to be dominated by intense tidal currents. Assuming the local current of 0.5m/s in average, the local semidiurnal tide rotates the current by up to 180 degrees. That gives 0.07 Hz additional Doppler shift during one hour which is far larger than the range resolution 0.0075 Hz. This covers 9 samplings in the Doppler spectrum. As the averaging should be done referring to Bragg peaks, it is necessary to remove the influence of such variability before doing averaging. A surface current contributes to a frequency shift of the whole Doppler spectrum by some Doppler shift Df . Experimentally, Df was estimated by measuring the difference between the Doppler frequency of the more energetic Bragg peak and its theoretical value (Eq. 2-8). Thus, before hourly summations, each spectrum was translated along the

frequency axis by $-Df$ to fix Bragg peaks onto their theoretical frequency positions (so-called de-shifting procedure). We measured the Doppler shift using the mean value measured from both Bragg peaks. The averaging of Doppler spectra was then implemented over a constant Doppler frequency scale.

We studied the number of qualified single spectra within 59 km to radar stations, i.e. 200 radar cells, during the 13-month period. There are 90% hours with at least one qualified Doppler spectrum. A percentage of 65% averaging used three qualified spectra; 21% used two qualified spectra; 14% used only one spectrum. Our work considered the averaged spectra with all three single spectra for the following processing and interpretation of surface parameters. Fig. 3-4 shows examples of the hourly averaging processing of spectra. The four examples are taken from four representative radar cells of station R1, including one closest radar cell on the beam normal to the receiving array, two on side beams and one in the central area of radar coverage.

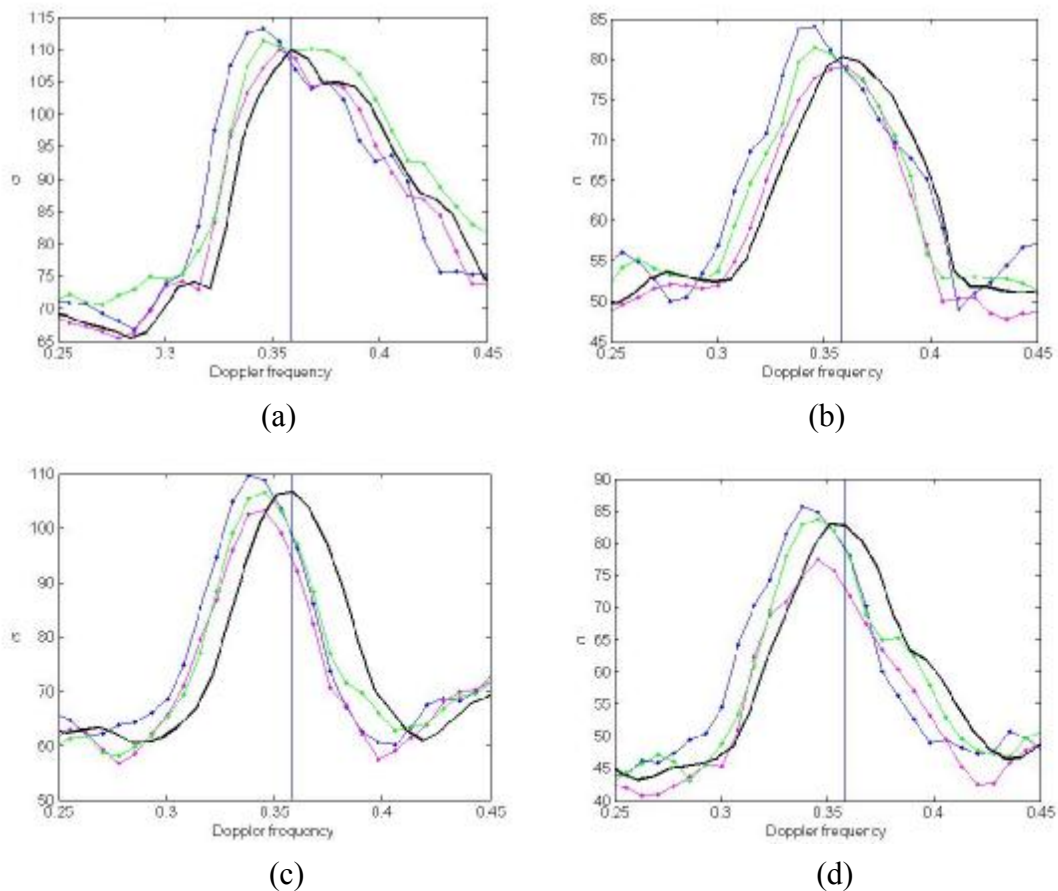
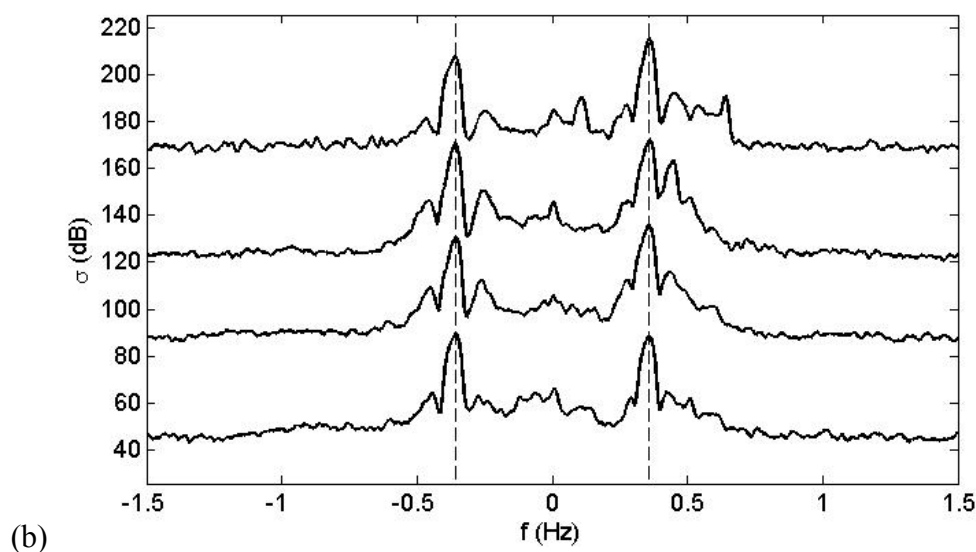
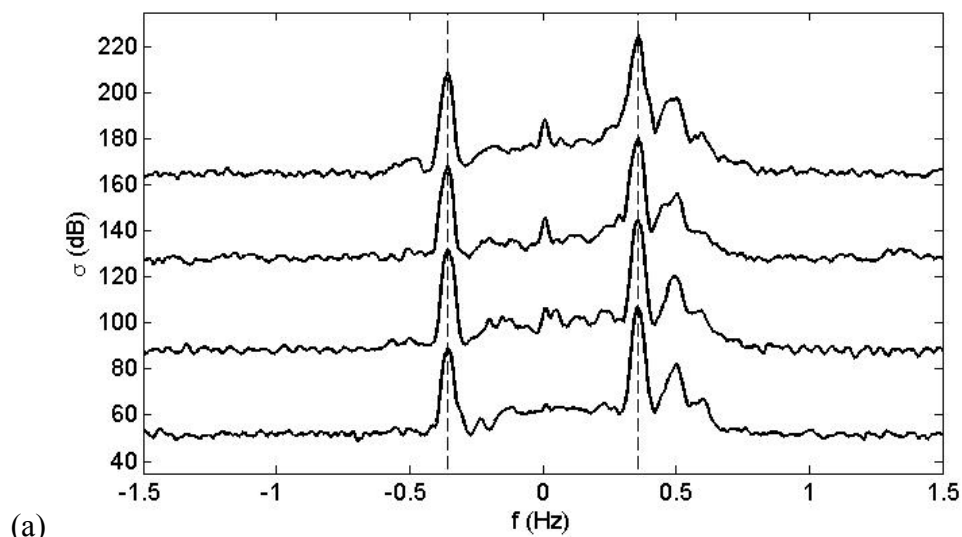


Fig. 3-4 Hourly averaging of Doppler spectra (unit: dB) on September 1, 2007 on

four radar cells: (a) R1 (11 km, 0°); (b) R1 (23 km, -60°); (c) R1 (23 km, 0°); (d) R1 (23 km, 60°). Blue, magenta and green lines show part of the single spectrum around positive Bragg peaks at 10 min, 30 min and 50 min, separately. Black line shows the de-shifted and hourly averaged spectrum. Perpendicular line indicates Bragg frequency.

Samples of hourly spectra are shown in Fig. 3-5. They come from a representative radar cell R1 (23 km, 0°). There is an increase of the amplitudes of second-order continuum from fall to winter (Fig. 3-5 a-d). This can be explained by the increase of wave energy generated in winter storms. Fig 3-5 (d) show spectra saturated by very high sea state which exceeds the ability of radar measurement.



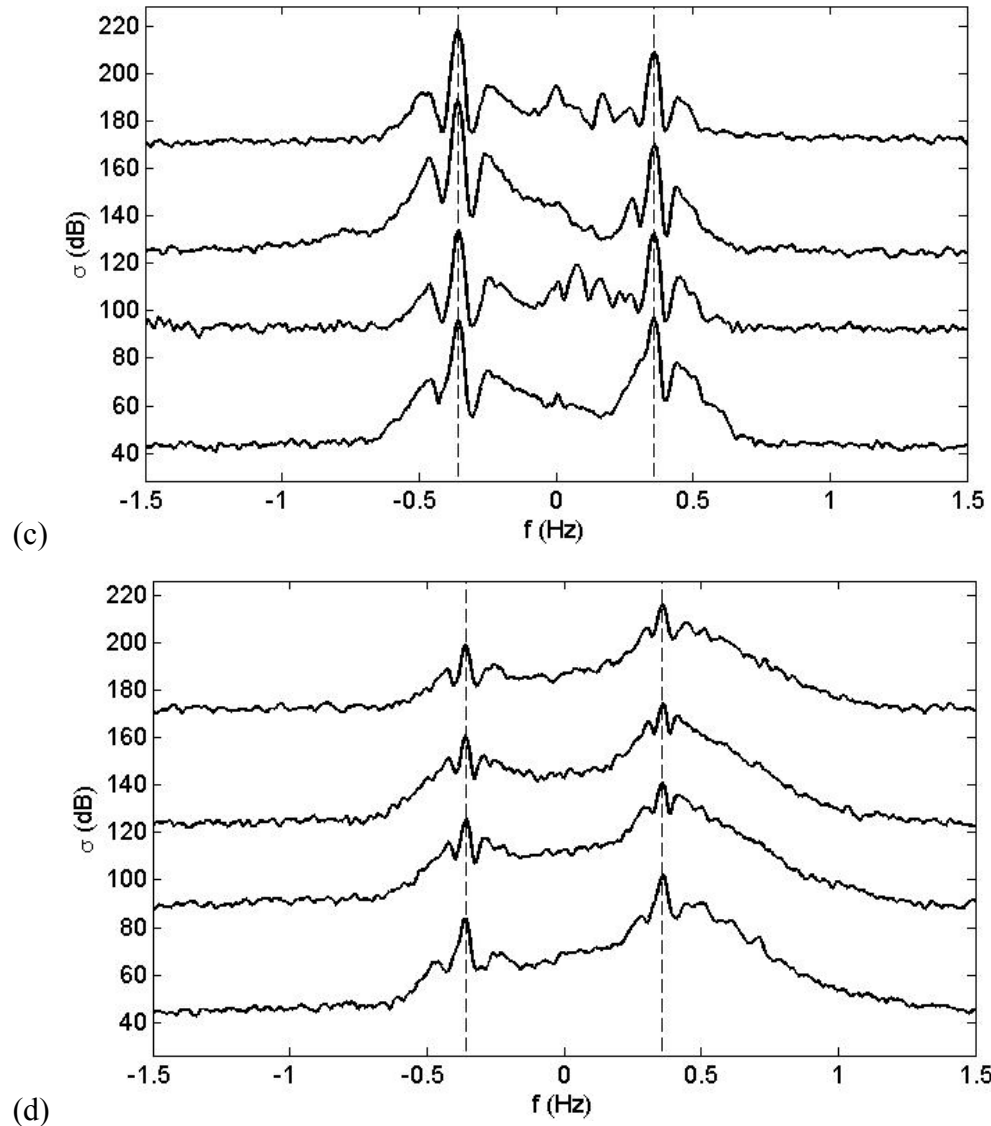


Fig. 3-5 Samples of the processed hourly Doppler spectra. Every four spectra are artificially spaced by 40 dB. From bottom to top, they are at 0:00 and 12:00 of the first two days of: (a) September 2007; (b) October 2007; (c) November 2007; (d) December 2007.

3.4 Quality control

Radar data are always contaminated with noise of instrumental and environmental origins and sometimes disturbed by unexpected targets such as ships. In addition, in case of high sea states, swell peaks in the Doppler spectrum can be masked by the broadening of Bragg peaks which is probably due to wind waves contribution (Grosdidier et al. 2014). These spectra are not qualified for the inversion

of ocean dynamic parameters, as they tend to pollute the inverted results and the evaluation of radar measurement ability. Also, rejection of bad data will greatly save computer resources of computation. In order to select physically meaningful Doppler spectra and, among them, those spectra showing swell signatures, several constraints were implemented on hourly spectra. This thesis finds a set of constraints through the study of radar cross section theory and Doppler spectra characteristics. We then seek to set proper thresholds and build a whole quality control program on hourly Doppler spectra.

(1) Background noise is inevitably included in radar spectra. Sea echo with low signal-to-noise ratio (SNR) is vulnerable to intense inner or environmental signals which may not be predictable. Those seriously affected spectra should be excluded from the automatic interpretation of spectra. In the past, thresholds based on the study of general radar equipment noise level were frequently applied. A quantity of -10 dB or -15 dB below spectral peak can be chosen as a reference (Sekhon and Srivastava 1971). The mean energy of sea echo spectra can be used as a limitation to filter abnormal spectra which have either too high or too small energy. This method is effective but it cut out potential measurements of very energetic or weak swell. Considering that the composite power of different kinds of noise might differ from time to time and from area to area, we seek to keep the most of observations by calculating the noise level for each specific hourly spectrum. The thesis applies the objective determination technique of Hildebrand and Sekhon (1974) under white noise assumption.

Based on the assumption of white noise, the average power spectral density equals standard deviation:

$$\frac{\overline{x^2} - \bar{x}^2}{\bar{x}^2} = \frac{1}{N_{sum}} \quad (3-2)$$

with x the spectral density of white noise. In the computation, sampling points of a Doppler spectrum were ranked from small to large. The sampling points with lower energy satisfying Eq. (3-2) were considered the background noise. Concerning the standard deviation of noise, effective spectral amplitudes were required to be over 3 dB above noise level. Fig. 3-6 show samples of noise level on three different radar cells on a same radar beam. The attenuation of effective signals is clearly seen from near coast to outer sea. The first-order signals can be easily observed even offshore while the second-order signals are more sensitive to the distance of propagation.

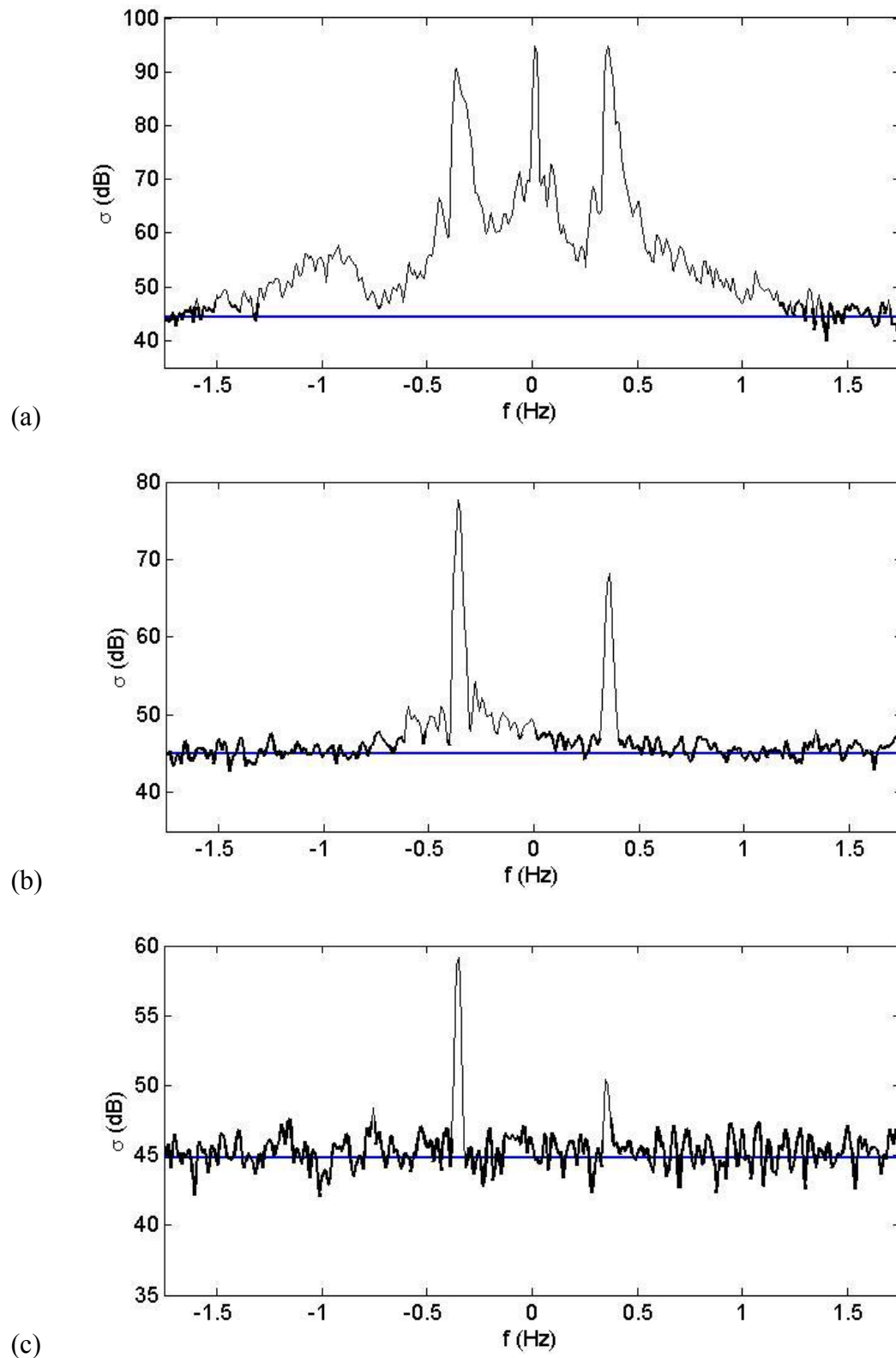


Fig. 3-6 Noise levels of hourly Doppler spectra at 0:00 October 1, 2007 for radar cells: (a) R1 (11 km, 0°); (b) R1 (71 km, 0°); (c) R1 (131 km, 0°). The blue horizontal line indicates the identified noise level. Thin curve shows the hourly radar spectrum.

Thick curve indicates spectrum under noise level plus 3 dB.

(2) Both negative and positive Bragg peaks were required to appear in the Doppler spectrum. Their amplitudes were required to be 6 dB above noise level. As de-shifting of a spectrum referred to the more energetic Bragg peak between the two, the summation right after could bring abnormal peaks in the hourly spectrum. Improper Bragg frequencies in the hourly spectrum must be filtered out through verification of Bragg peaks' displacement. The first-order cross section equation gives the theoretical displacement between the two Bragg frequencies

$$f_+ - f_- = 2f_B \quad (3-3)$$

A tolerance of $\pm 2df$, i.e. two resolution intervals, was given to the measured distance between them in a hourly spectrum.

(3) Although some interpretation can be done using two or three swell peaks only, a number of exactly four swell peaks were required to appear in one radar spectrum. Second-order radar cross section shows that the Doppler frequencies of the four swell peaks satisfy

$$f_1 + f_2 = -2f_B \quad (3-4)$$

$$f_3 + f_4 = 2f_B \quad (3-5)$$

As in the law above, a deviation of $\pm 2df$ was tolerated for both distances.

(4) The swell spectral maxima are looked for within four intervals on each side of the two Bragg peaks. These intervals, which correspond to the swell periods given in introduction, are determined from two criteria. The first one requires

$$\left| |f_j| - f_B \right| > 6df \quad (3-6)$$

to prevent the swell peaks from being absorbed in the Bragg peaks. The value of 6 was fixed according to the statistical properties of the half power spectral peak widths. The width thresholds for Bragg peaks and swell peaks are $4.2df$ and $6.2df$, respectively (see threshold law after). Eq. (3-6) imposes the distance between a swell peak and its neighboring Bragg peak to be larger than half the sum of their widths, $5.1df$.

The second one requires

$$\left| |f_j| - \sqrt{2}f_B \right| > 3df \quad (3-7)$$

to prevent the swell peaks from being confused with the harmonic peaks. The right term in Eq. (3-7) was chosen to be larger than half the 5-point interval (see the 5-point law after). According to Hasselmann's prediction (1971) and Forget et al. (1981), $|f_j|$ is approximately equal to $f_B - F_s$. Then Eq. (3-6) gives $F_s > F_{s\min} = 0.045$ Hz. Eq. (3-7) gives $F_s < F_{s\max} = 0.126$ Hz. Inside each interval, a swell peak is identified as the more energetic peak of the first two maxima which are closer to the neighboring Bragg line.

(5) To increase the robustness of peak identification, a spectral peak is defined as consisting of 5 sampling points: the maximum and two spectral points with monotonically decreasing amplitudes on each side of the maximum. A 5-point weighting method gives the frequency estimate

$$f_j = \frac{\sum_{e=-2}^{+2} (f_j + edf) s_e^{(2)}}{\sum_{e=-2}^{+2} s_e^{(2)}} \quad (3-8)$$

with $s_e^{(2)}$ the measured second-order spectral amplitude at Doppler frequency $f_j + edf$, Fig. 3-7. This number of 5 was suggested by a statistical investigation which showed that, by average, spectral swell peaks can be specified by $N_{1/2} \approx 5$ points above half power level (-3 dB with respect to peak maxima).

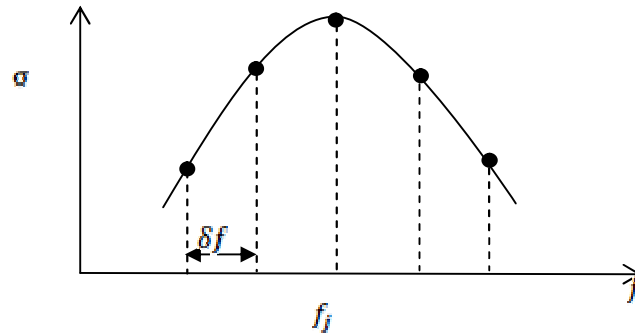
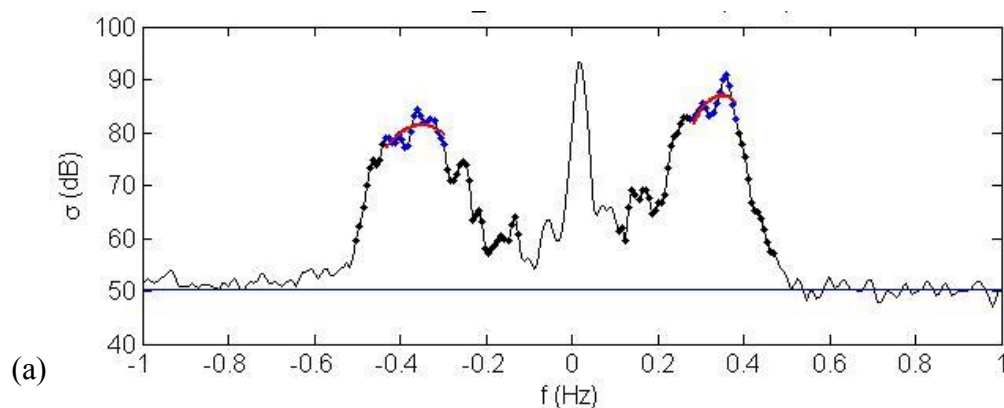


Fig. 3-7 The 5-point weighting method for a spectral peak.

(6) Some spectra show more than four qualified peaks in the searching intervals of swell peaks. This phenomenon might be explained by the existence of two or more swell on the ocean surface. However, in those cases the less energetic swell often fails

to make an exact number of four corresponding spectral peaks in the Doppler spectra. Instead, there are often one or two peaks available. Such isolated peaks can also be created by feedback of ships. The hourly summation could also bring in abnormal peaks when the de-shifting of single spectrum referred to the wrongly identified Bragg peak maximum. For these reasons, the thesis identified and studied only the most energetic swell component. In each searching interval, we looked into the two closest peaks near the Bragg peak and took the more energetic one as the identified swell peak.

(7) Thresholds were imposed on the half-power width of Bragg and swell peaks, respectively, assuming these peaks are Gaussian shaped. For Bragg peaks, a Gaussian fitting was performed onto spectral amplitudes larger than one tenth of the maximum value. For a swell peak, the fitting considered the 5 points which constitute the peak. Although there is no reason that the peaks are Gaussian shaped, this criterion does help to exclude a significant number of severely distorted radar spectra. The width threshold was set to 0.0318 Hz for Bragg peaks (71% of the total number of detected Bragg peaks) and to 0.0485 Hz for swell peaks (90% of the total number of detected swell peaks). Fig. 3-8 shows samples of filtered broadened Bragg peaks. These cases were often observed on radar cells on outer radar beams. Two reasons help explain. One is that the radar antenna receives large contributions from side lobes on these beams. The other reason is the uncertainties after hourly summation.



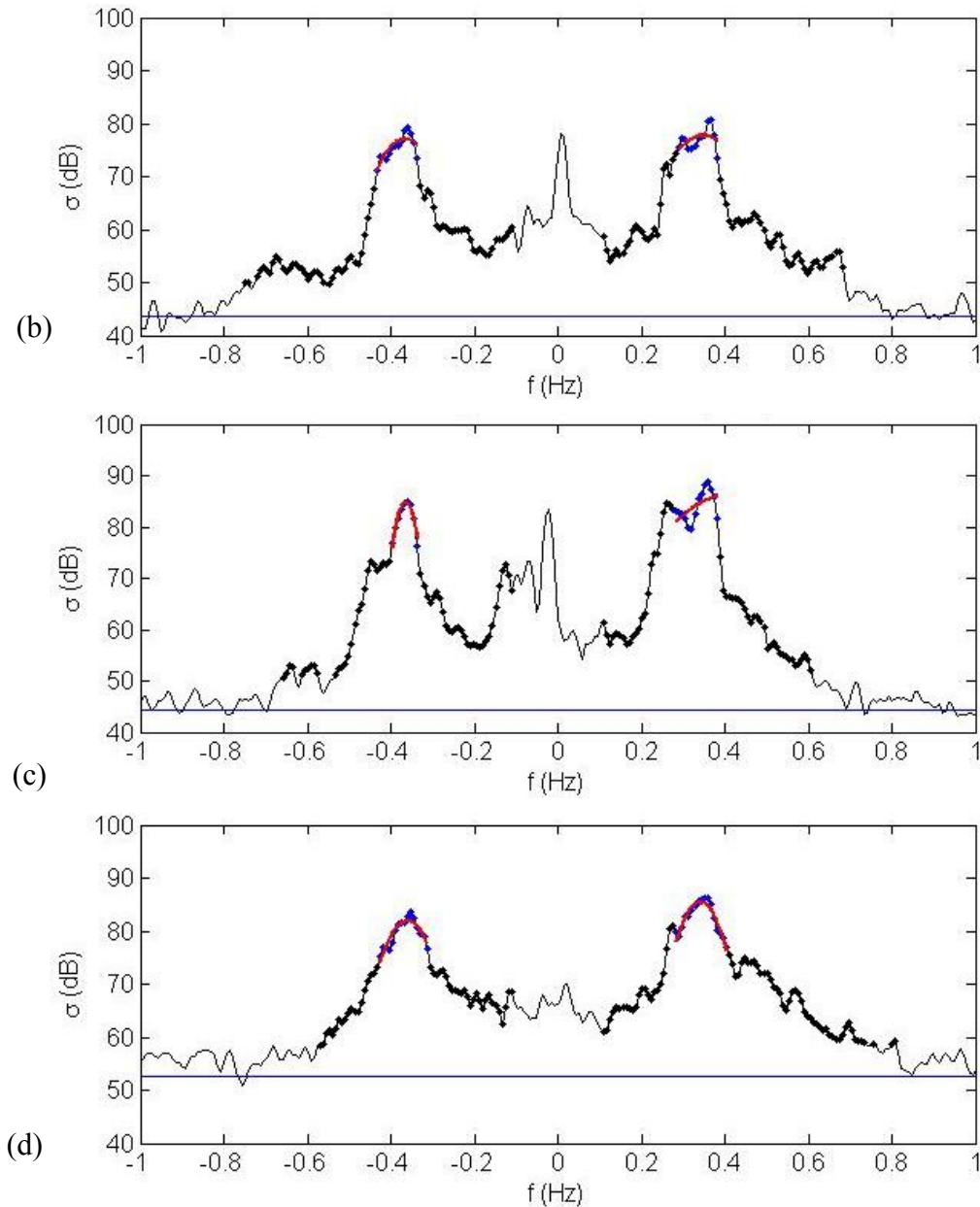


Fig. 3-8 Broadened Bragg peaks. The blue points are the sampling points considered in the Gaussian fitting which is indicated in red. Thin black curve is the Doppler spectrum. Black points show effective spectrum 3 dB above noise. Blue horizontal line is the noise level.

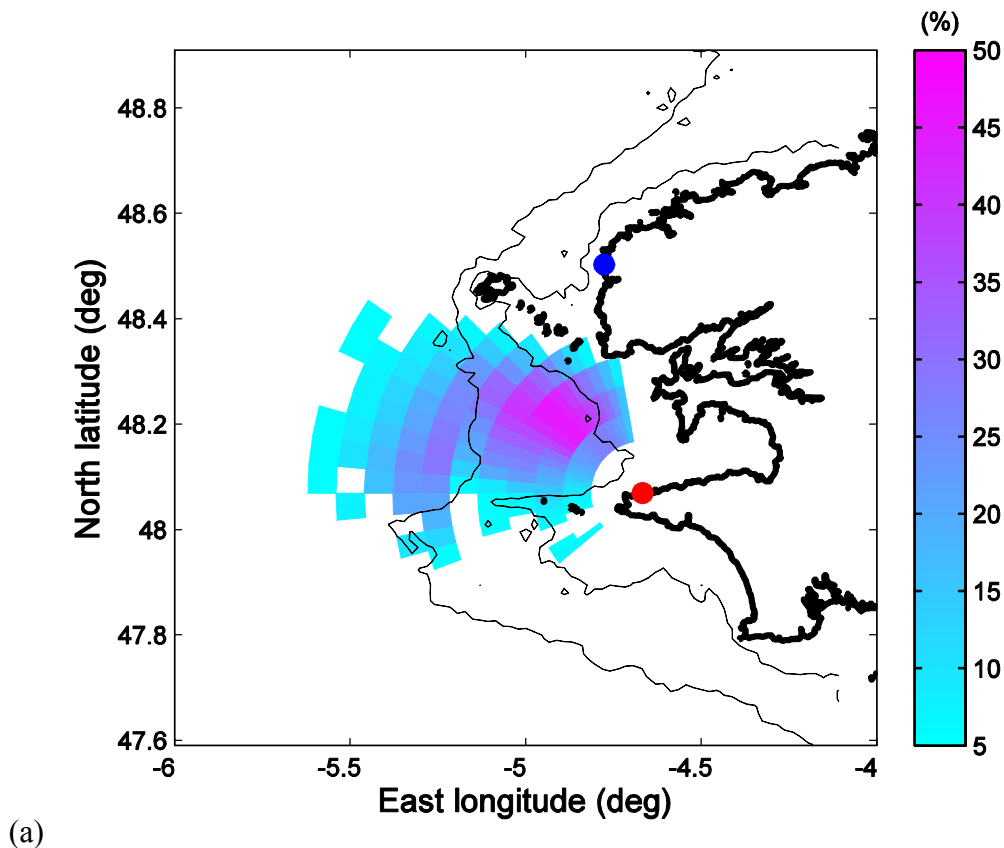
3.5 Statistics of qualified spectra

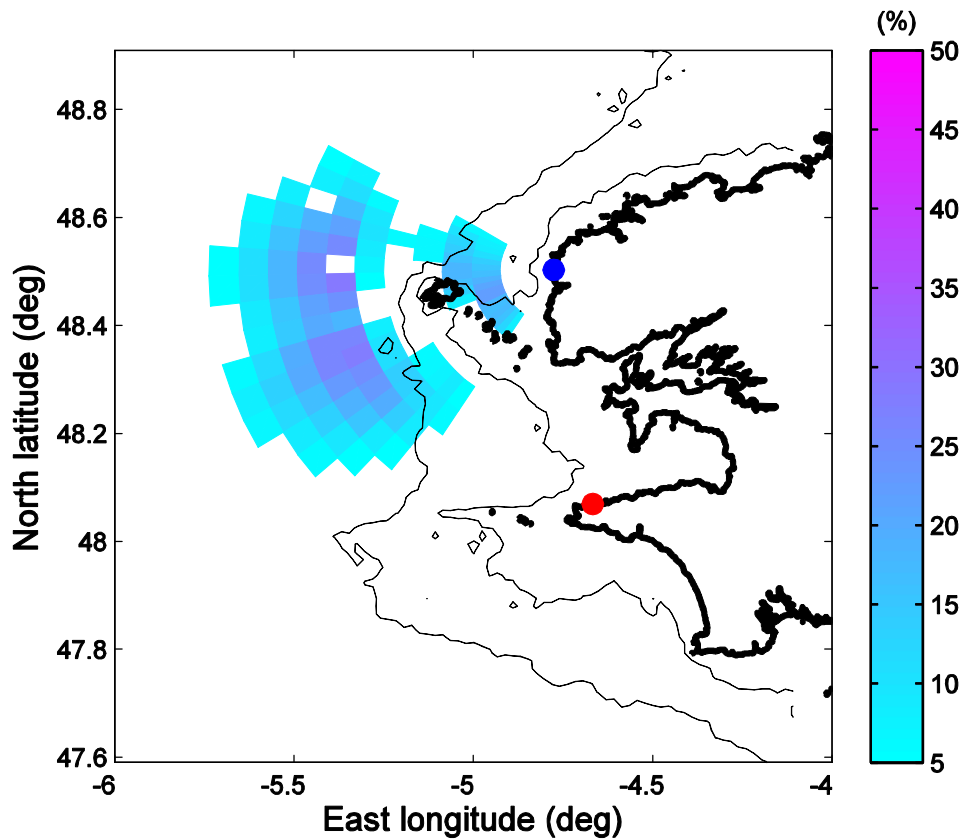
The temporal data coverage (TDC) of measured swell frequency is shown in Fig. 3-9. For each radar cell, TDC is quantified by the ratio, expressed in percentage, of the number of inverted F_s over the total number of hours during the whole 13-month period (9504 hours). For both radars, the decrease in TDC at far ranges is due to the

decrease of the signal to noise ratio (SNR) caused by the attenuation of radar signal with distance. Radar cells with TDC values less than 5% (475 samples) are not shown.

For station R1 (Fig. 3-9 a), TDC values greater than 20% (1900 samples) are associated with radar cells ranging from 11 km and 47 km, i.e. at the first several ranges. There is a decrease of the amount of qualified spectra in the downright part of Fig. 3-9 (a), especially in the vicinity of Sein archipelago. This can be interpreted as shallow water effects which are responsible for wave breaking there. Such breaking conditions are known to profoundly distort the Doppler spectrum from the standard form (Broche and Forget 1993). The farthest radar cell with over 5% of qualified measurements over the 13 months locates 65 km to station R1.

For station R2 (Fig. 3-9 b), TDC values greater than 20% were found from 11 km to 17 km and from 41 km to 47 km. We observed that R2 experienced some shadowing by Ushant island and Molène archipelago, which results in a decrease of TDC, or even an absence of data, in the third to fifth ranges.





(b)

Fig. 3-9 Temporal data coverage (TDC) of qualified radar Doppler spectra with four swell peaks. (a): TDC of station R1. (b): TDC of station R2.

3.6 Summary

This thesis processed radar data from two WERA systems during a period ranging from September 1, 2007 to September 30, 2008. With 16 antennas, the received signals were processed by beam forming technique. Acquisition was performed every 20 min by each radar station. Time series of voltage radar signals were cut into subseries to give Doppler spectrum via FFT. These spectra were averaged to give single radar spectrum. Hourly spectra were obtained through spatial and temporal averaging of single spectra. After these processing, wind wave characteristics were greatly inhibited and swell features were reinforced. In all, a number of 48 independent spectra were summed up, leading to 96 degrees of freedom for each sampling point.

Proper quality control was applied on hourly spectra, including noise level, positions of Bragg and swell peaks, peak widths, searching intervals, etc. These criteria were derived according to theoretical analysis and statistical studies. We have

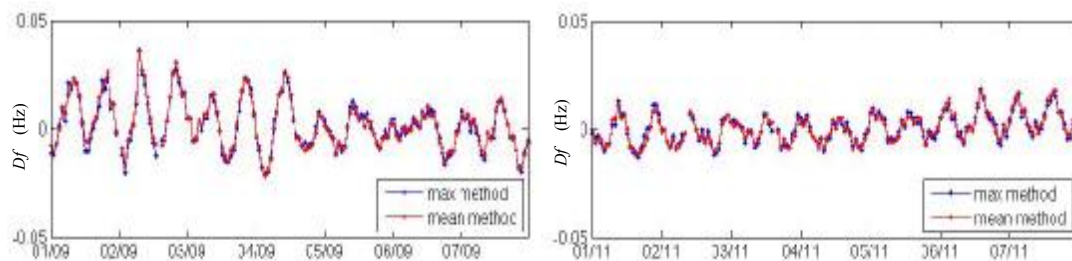
knowledge of the number of qualified hourly spectra over the radar coverage for the interpretation of second-order continuum concerning swell. Most effective measurements were found in a distance of about 25 km. For both stations, temporal data coverage greater than 20% (1900 samples) appear in the distance of 11 km - 47 km from station; TDC greater than 5% (475 samples) can reach 65 km from station. Data collected from station R2 suffers from impacts of islands. A larger number of observations come from station R1.

4 Results of surface currents

Radial current velocities were calculated from single radar spectrum every 20 min by measuring the Doppler shift of Bragg peaks, noted as v_{cr1} and v_{cr2} for stations R1 and R2, respectively. Total current vectors were obtained by combining radial velocities using method described in Section 2.2, noted as \vec{v}_{cr} .

4.1 Radial current velocities

Doppler shift induced by surface current was measured from the experimental Doppler frequencies of Bragg peaks. There are two approaches to do the measurement. One refers to the Doppler shift of the more energetic Bragg peak. The other refers to the mean shifting of both Bragg peaks. Fig. 4-1 compares the two approaches in time series. Examples are taken from radar cell R1 (23 km, -15°) at 10 min every hour in sequentially selected six months. Each time series lasts the first week of the month. During the 13-month period, the RMS difference between the two is 0.0027 Hz. Assuming both measurements are white noise within the interval of Doppler frequency resolution ($df = 0.0075$ Hz), the RMS difference between the two is expected to be $\sqrt{12}^{-1} df$, i.e. 0.0022Hz. Most of the time, the difference between the two measurements is negligible. This illustrates that the less energetic Bragg peak is also trustful most of the time. From a statistical point of view, this thesis used the second method to determine surface current induced Doppler shift and to do the de-shifting of spectra.



(a) September 2007

(b) November 2007

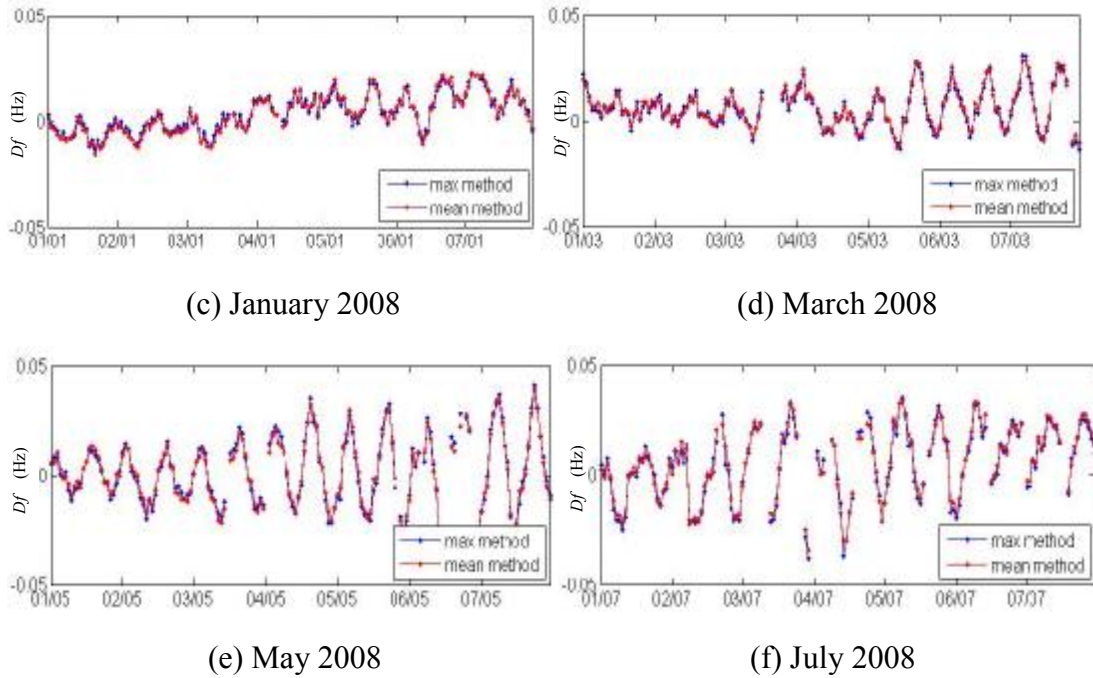


Fig. 4-1 Comparison between two ways of determining current-induced Doppler shifts in six months. Blue dot: Df measured from the more energetic Bragg peak. Red dot: mean Df measured from both Bragg peaks.

The radial current is proportional to Doppler shift indicated by Eq. (2-16). Fig. 4-2 (a) shows the inverted radial current velocity corresponding to Fig. 4-1 (a). Fig. 4-2 (b) gives the FFT analysis of the whole one year time series of radial velocities from the same radar cell. The analysis shows the most significant frequency at 0.0806 h^{-1} , i.e. 12.4 h. This significant period of local current variation coincides with the period of local tide which is mainly constituted by the semi-diurnal constituent.

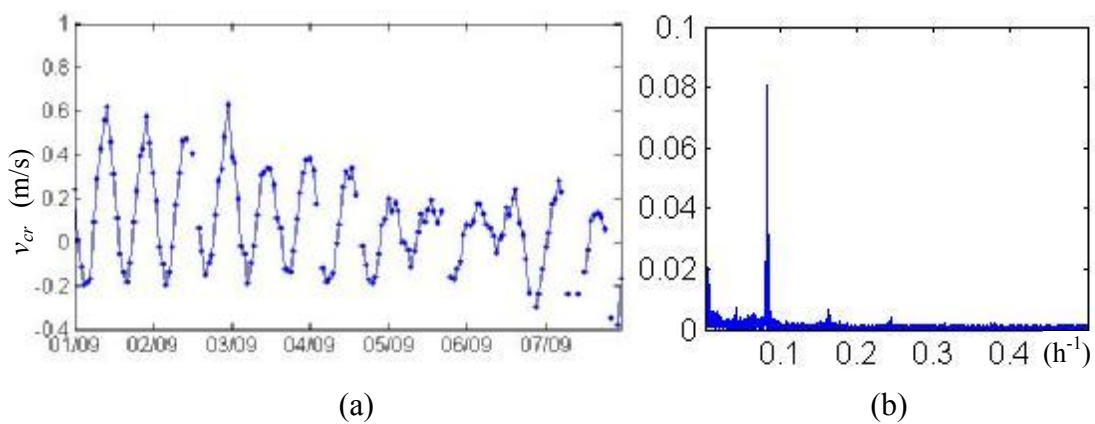


Fig. 4-2 Radial current velocities inverted from Doppler shift. (a) Time series

during one week corresponding to Fig. 4-1 (a). (b) FFT analysis for the whole one year period on the same radar cell.

Radial current field shows radial velocity components over the whole radar coverage. Samples from two radar stations at adjacent moments are shown in Fig. 4-3. These examples show velocities of less than 1 m/s, generally speaking. The gaps near islands show the damages of radar spectra by influences of islands.

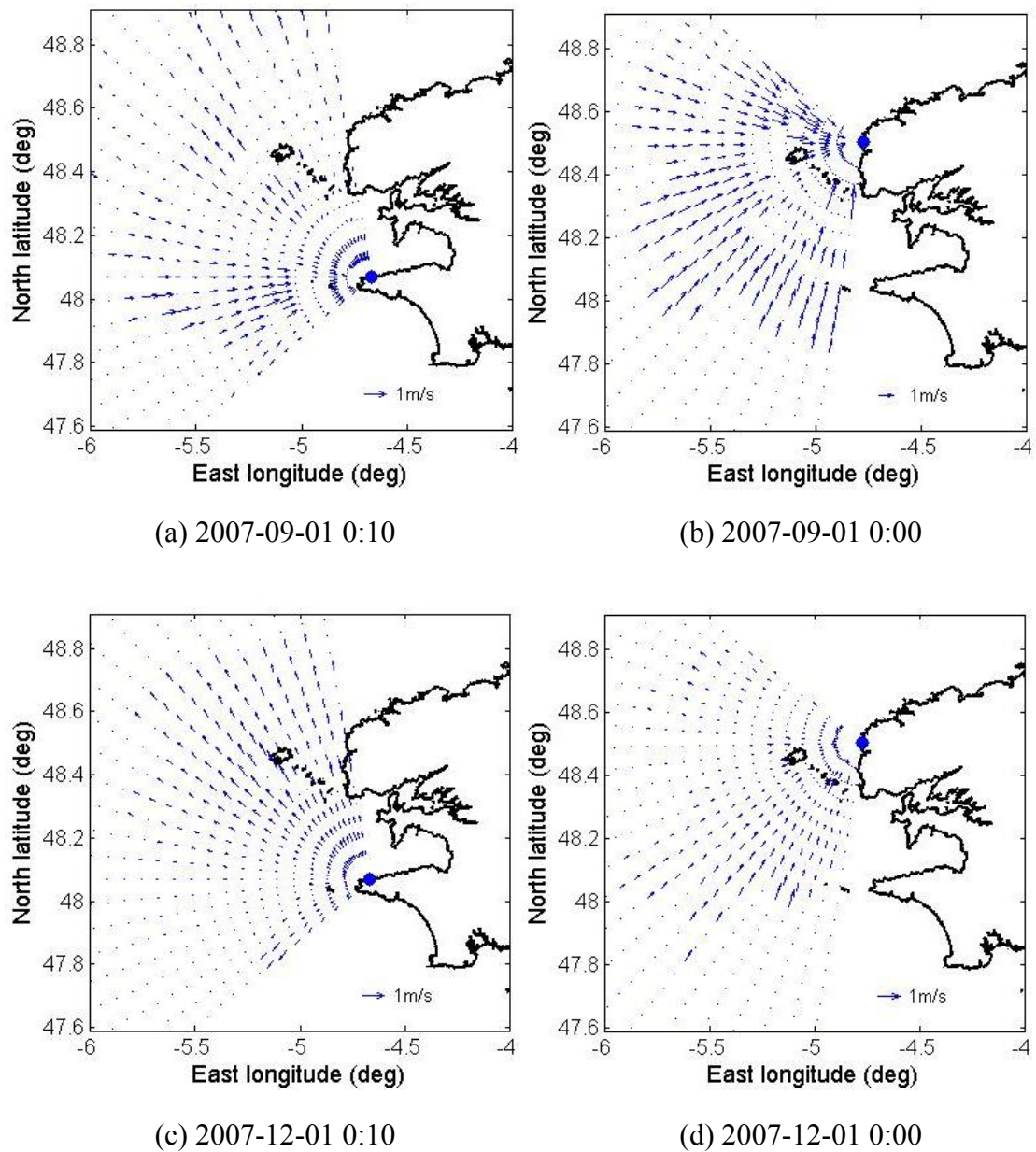
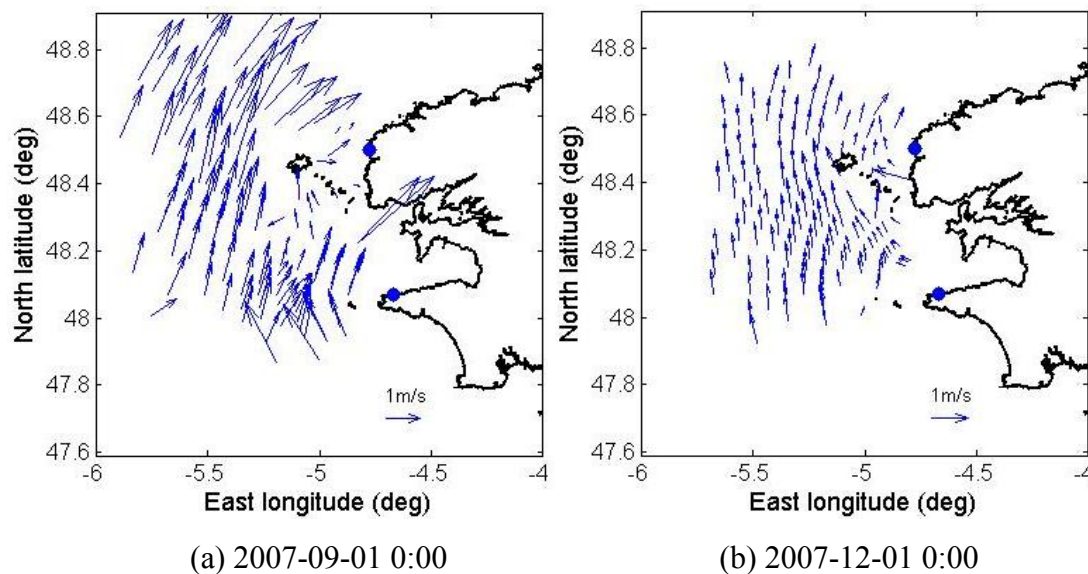


Fig. 4-3 Samples of radial current velocity fields. (a) and (b) are obtained by station R1. (b) and (d) are obtained by station R2.

4.2 Total current vectors

Current vectors were computed on common radar cells following the method described in Section 2.2. A common radar cell consists of two radar cells from each radar station separating less than 3 km. The surface current field is supposed not to vary much in the plane within several kilometers, as it is dominated by tide. The up to 20 min delay between measurements from two stations was neglected.

Samples of current field are shown in Fig. 4-4 in every three months. The four examples show flow moving from southwest to northeast, from right south to north, from southeast to northwest, and from northwest to southeast, separately. All these cases show that the flow rotates slightly around the Ushant Island, Molène archipelago and the mainland. Currents vary not much on the outer region off the coast. They show more obvious variations around islands and archipelagos. The local surface environments around islands are indeed complex. Another potential explanation is that the land influences propagation of electromagnetic signals.



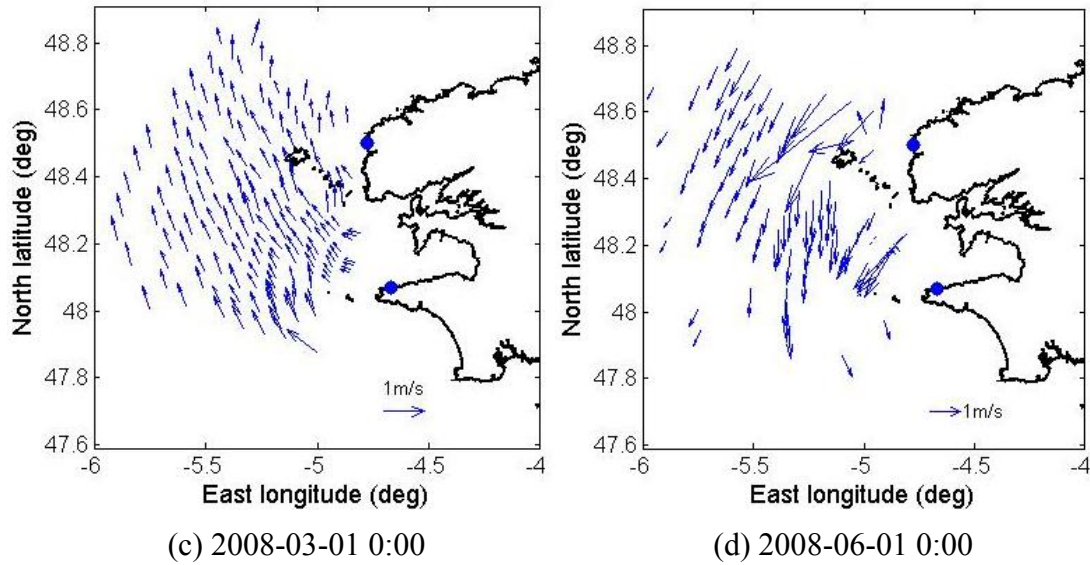


Fig. 4-4 Total current vector fields on common radar cells at the beginning of four months.

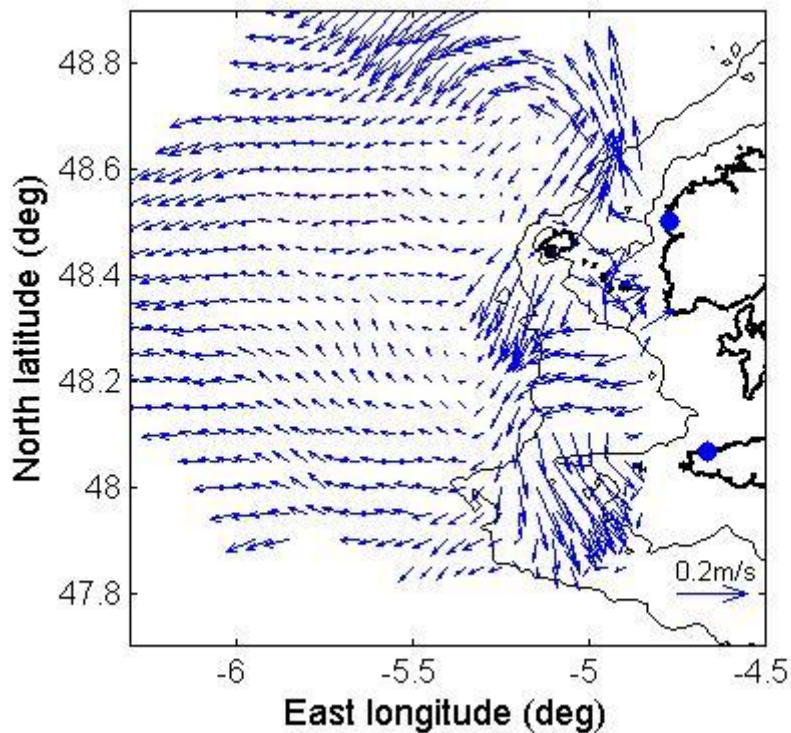


Fig. 4-5 One-year (Sep 1, 2007 – Aug 31, 2008) averaged surface current field in the Iroise Sea. Thin curves show bathymetry contours of 50 m and 100 m.

The mean flow pattern in a one-year period from September 1, 2007 to August

31, 2008 is shown in Fig. 4-5. Both horizontal and vertical velocity components are linearly interpolated on regular grids of 0.05° in longitude by 0.05° in latitude. Original measurements on radar cells with over 720 samples, i.e. effective hourly measurements in one month, are taken into the interpolation. In the region far off the land, the current velocities are generally less than 10 cm/s. At longitude interval of -6° to -5.5° , the flow pattern shows currents towards southwest from the northeast and currents towards northwest or from the south. Farther west, currents flow nearly towards west. Near shoreline, currents have much larger velocities. In some patches near the islands, currents exceed 20 cm/s. The flow moves towards northeast in the north of Ushant Island and moves southwest in the south of the island. In the western region near Sein archipelago currents move along the bathymetry towards southeast.

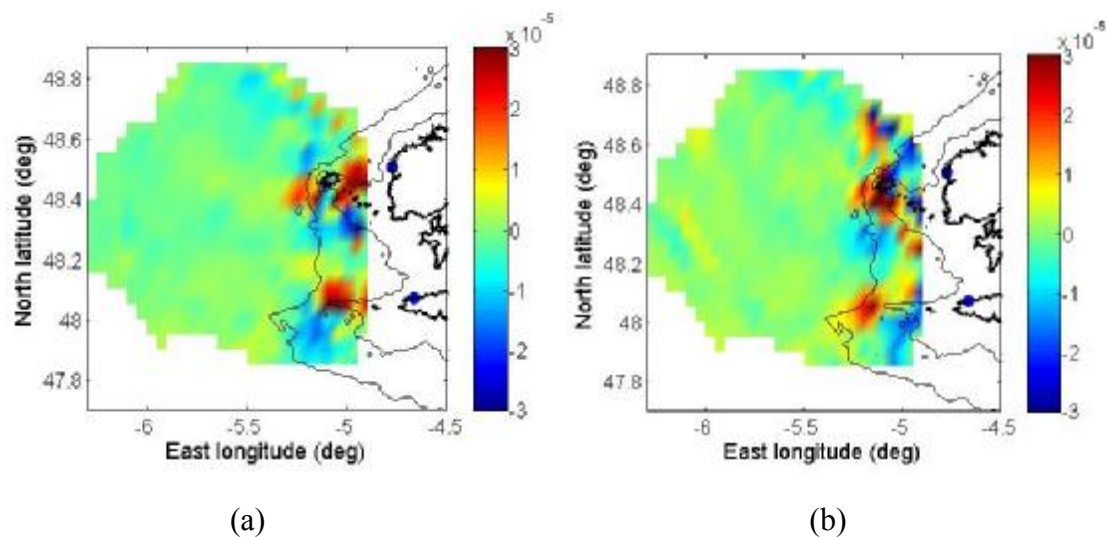


Fig. 4-6 Vorticity (a, unit: s^{-1}) and Divergence (b, unit: s^{-1}) of the mean current field in Fig. 4-5.

The dynamics of the one-year mean flow are further investigated by vorticity ($dv/dx - du/dy$) and divergence ($du/dx + dv/dy$) in Fig. 4-6. Vorticities are not evident except regions near islands. High positive vorticity appears in the southeast of Ushant Island, west of Molène archipelago and north of Sein archipelago. Evident negative vorticity appears in the south of Molène and Sein archipelagos. In Fig. 4-6 (b), the divergence (warm colors) and convergence (cold colors) are observed mainly near islands, too. Strong divergences are observed in the south of Ushant Island and in

the west of Sein archipelago.

Temporal variations of the total current vector can be investigated on single radar cells. Examples are shown in Fig. 4-7. Vectors are plotted every 6 hours in one month. The pair of common radar cells are R1 (41 km, -20°) and R2 (35 km, 25°) with longitudes and latitudes (-5.068° , 48.295°) and (-5.086° , 48.290°), respectively. The two radar cells separate 1.5 km.

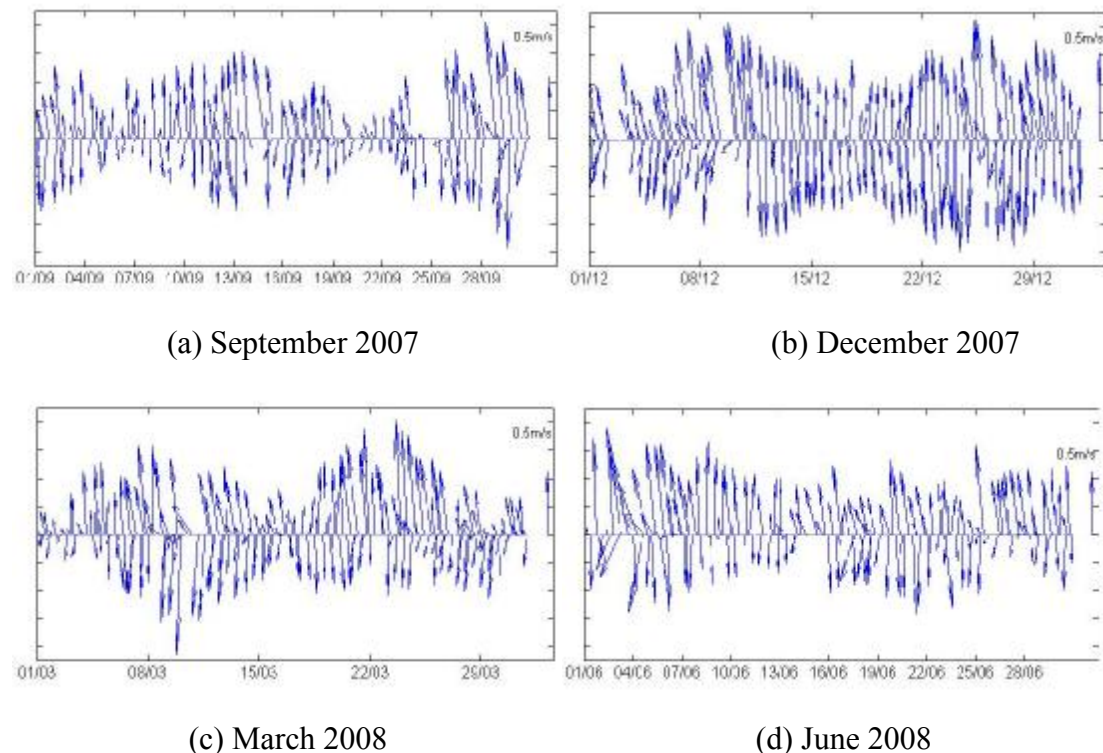


Fig. 4-7 Time series of total current vector at a mean location of (-5.07° , 58.3°) in four sequentially selected months in 2007. The perpendicular vector at the right end of each axis shows legend of 0.5 m/s.

The technique of current inversion is rather mature. More work on the study of currents by HFR in the Iroise Sea are presented Sentchev et al. (2013), Muller et al. (2009), Ardhuin et al. (2009a), etc. Accuracy of surface currents by HFR is discussed in many other studies. For example Le Boyer et al. (2009) used measurements of currents provided by surface drifters and ADCP for a period of 7 months to show that the discrepancies in velocity measured by HFR compared to other instruments are generally under 0.15 m/s in the majority of situations. It is notable that the part of

discrepancies can also come from the methodological differences of different devices. Different instruments define “surface velocity” in distinct ways.

4.3 Currents by SeaSonde

Two SeaSondes were installed to monitor the coastal region off Qingdao in 2008, Fig. 4-8. The study area locates in the southeast of Qingdao, on the west of Yellow Sea. The water depth is rather shallow (about 25 m) except the northwest area (over 35 m) near the strait to Jiaozhou bay. The two radar stations locate at Dagongdao and Xuejiadao, respectively, separating 22 km from each other. An area of about 400 km² is covered by the combination of the two stations. The data processing program combined radial velocities obtained from both radar stations and provides total current vector field per hour on regular grid of 0.5 km by 0.5 km using radial velocities within a 1 km² area. Lu et al. (2008) observed that the tidal velocity reached 1 m/s near the strait. Zhao et al. (2011) studied the spatial and temporal structures of the Qingdao coastal flow. This thesis reviews and extends these studies.

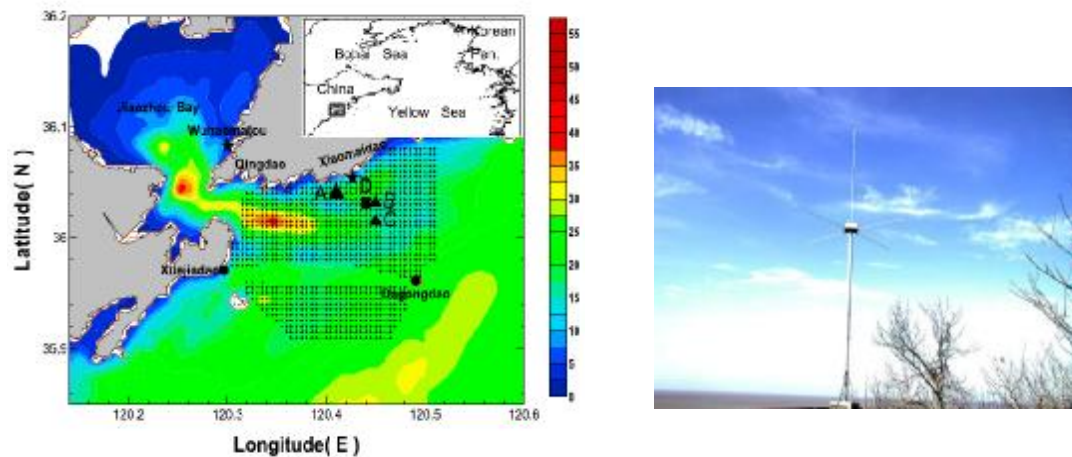


Fig. 4-8 Study area off Qingdao. (a) Locations of SeaSondes (from Zhao et al. 2011). Contours show water depths in meters. Small crosses show regular radar grids. (b) SeaSonde antenna in the field.

This thesis used the continuous and relatively high quality observations of surface currents during August, 2008. A statistics of the effective measurements is shown in Fig. 4-9. The area around radar baseline provided few robust measurements

as the two radar beams are nearly parallel. Most of the grids experienced temporal data coverage of over 90%.

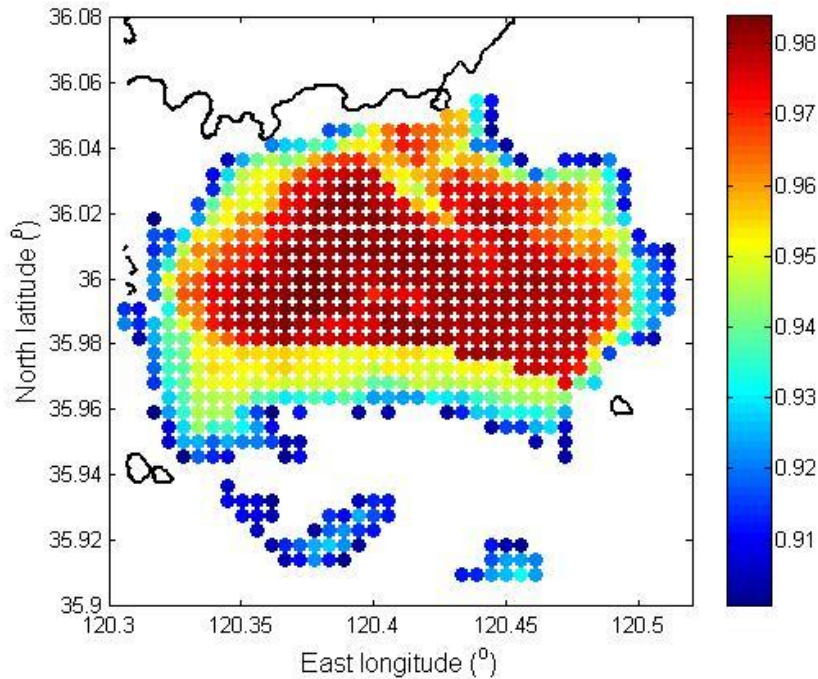


Fig. 4-9 Temporal data coverage for the observation of total current vector in August 2008. Colors show the percentage of over 90% on regular grids.

Examples of hourly current field are shown in Fig. 4-10. The time is evenly chosen every 6 hours on the first day of August. At 0:00, the currents flow towards shoreline coming from southwest. The flow separates into two branches in the north: one passes through the strait and entered Jiaozhou Bay; the other continues northeast along the shoreline. After 6 hours, the flow field turns back its direction with currents flow from northeast to southwest. Currents enter the strait with rather large velocities. At 12:00, currents move northward again. However, in the north, there is a region with southward flow which is then slowed by the island of Dagongdao and is rushed to the north by the big flow from southwest. At 18:00, fast currents flow out of Jiaozhou Bay through the strait. They spread out to the north along shoreline and to the open ocean south.

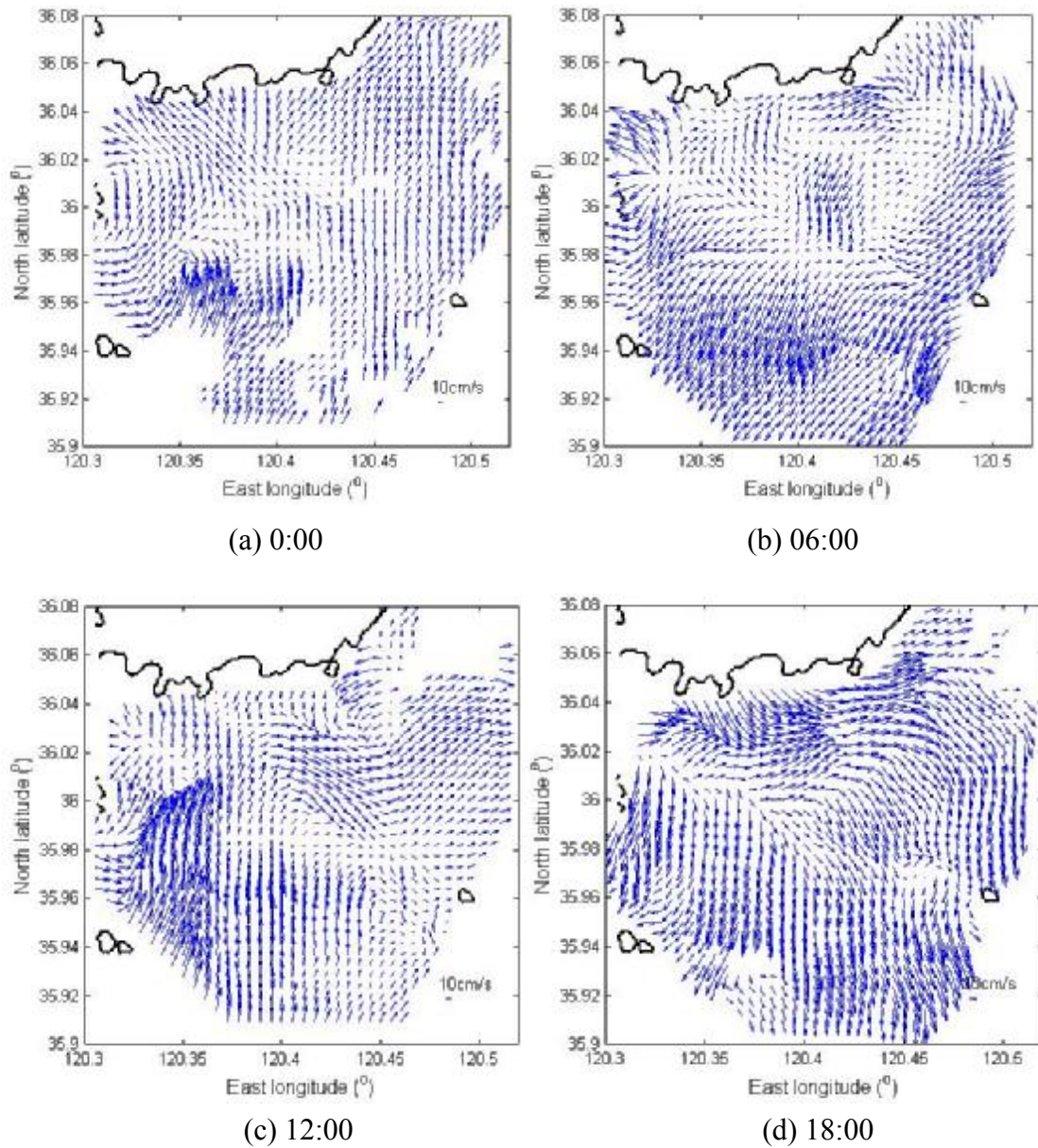


Fig. 4-10 Hourly current fields at four moments on August 1, 2008.

The averaged total current vector field in August 2008 is shown in Fig. 4-11 (a). Grids with over 50% temporal data coverage are considered. Averaged velocities are about 15 cm/s for most of the region. The mean flow rotates in a clockwise way. The eddy is clearly observed in Fig. 4-11 (b) by streamlines. There is a rotation center in the central area of radar coverage.

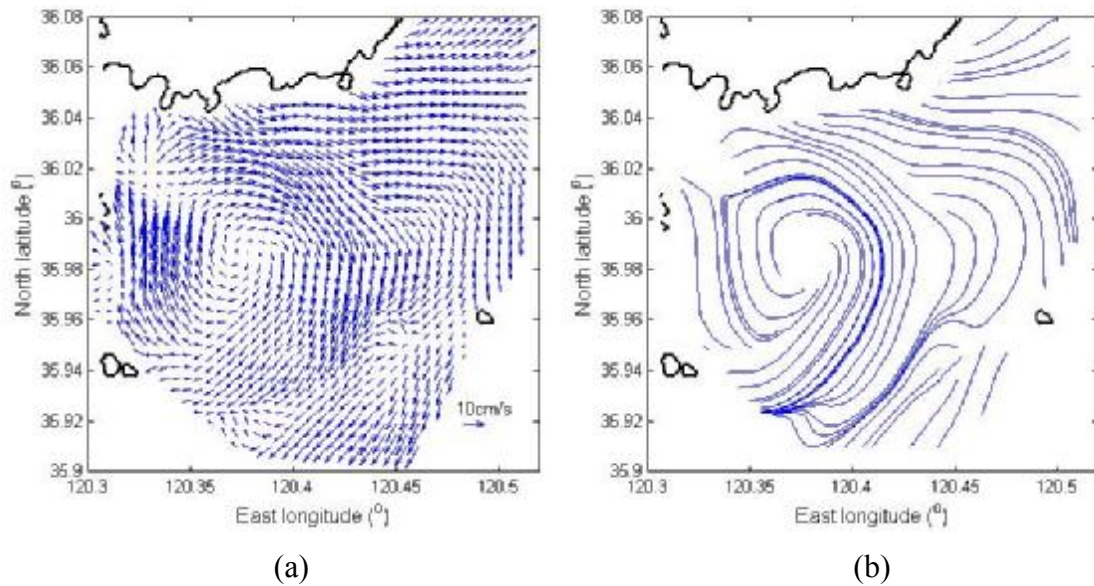


Fig. 4-11 Averaged flow field in August 2008. (a) Current vectors on grids. (b) Streamlines.

The dynamics of the flow in this region were investigated. Vorticity of the mean flow field in August are computed on the spatially gridded radar coverage, Fig. 4-12. Warm colors indicate positive vorticity while cold colors indicate negative vorticity. There is a patch of high negative vorticity in the southwest of the region where the flow shows anti-cyclonic curvature. In the northeast, there is an area with relatively high positive vorticity. The flow tends to exhibit cyclonic curvature but turn its way after. This shift of direction is probably caused by the constraint of topography. In the northwest, in the entrance of the strait, there is a region with high negative vorticity. This variation of direction can be explained by two reasons: one is the rushing power of the water from the strait; the other is the variation of the shoreline.

Characteristics of divergence and convergence of the mean flow field are shown in Fig. 4-13. Warm colors indicate divergence while cold colors indicate convergence. High divergence appears at the entrance of the strait. In its south, there is a region of high convergence. Farther south, there appears another region of high divergence. In other regions, which are more close to outer ocean, divergence/convergence is much less obvious.

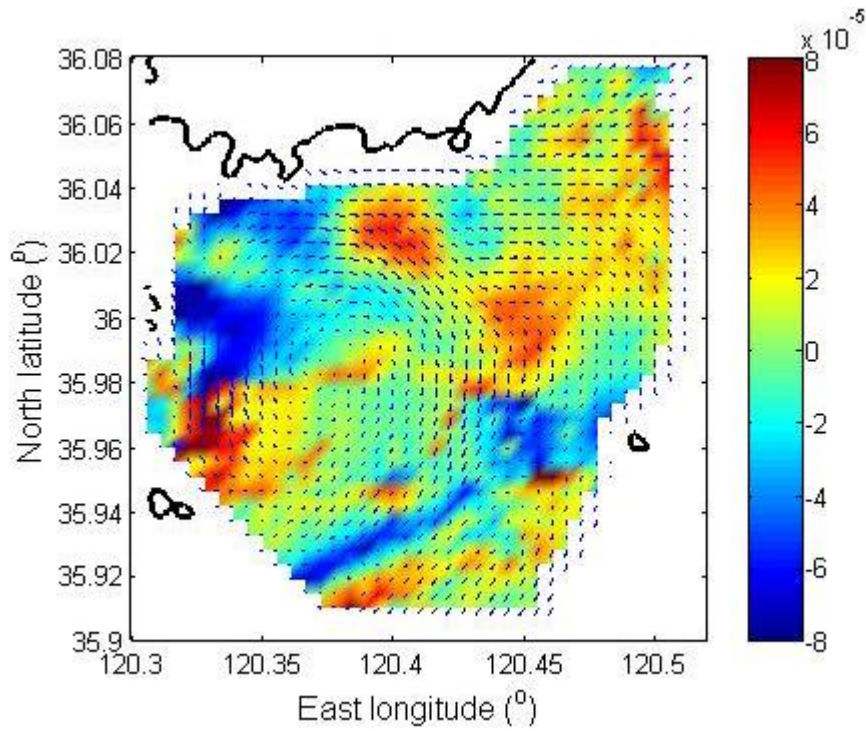


Fig. 4-12 Vorticity pattern of the mean flow field in August 2008. Warm (cold) colors indicate positive (negative) vorticity (unit: s^{-1}).

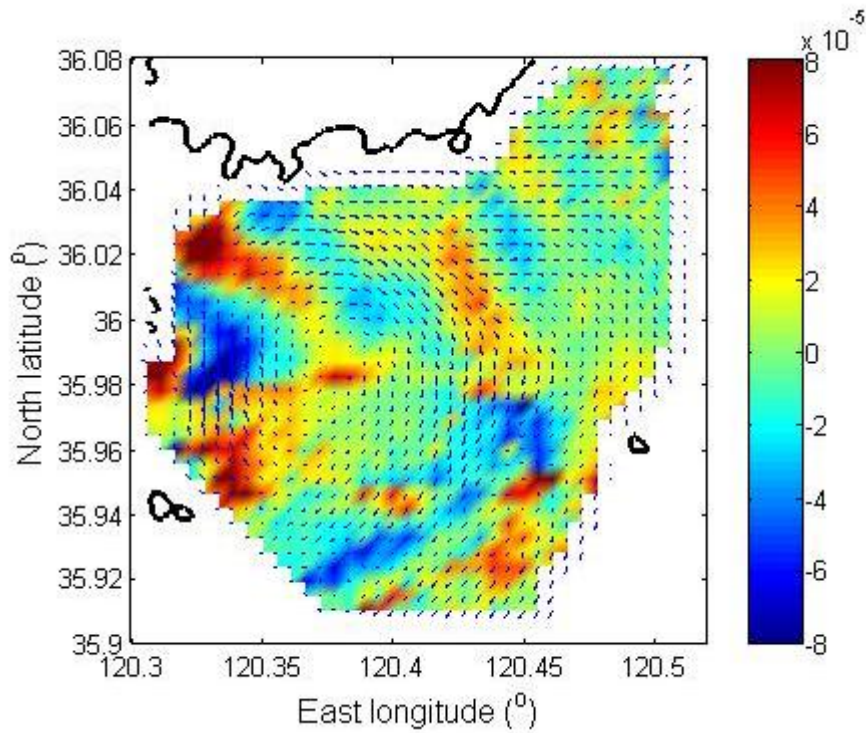


Fig. 4-13 Divergence/convergence pattern of the mean flow field in August 2008. Warm (cold) colors indicate divergence (convergence) (unit: s^{-1}).

4.4 Summary

Ocean surface currents by HFR from one French WERA system and one Chinese SeaSonde system were investigated. Radial velocities obtained from the WERA system were computed by measuring the mean Doppler shift of both Bragg peaks in single radar spectra. Measurements from two stations were combined to provide surface current maps at intervals of 20 min which is determined by different acquisition times of the two stations. The HFR system in the coastal area off Qingdao, China, consisted of two SeaSonde provides total current velocities at 1 h interval.

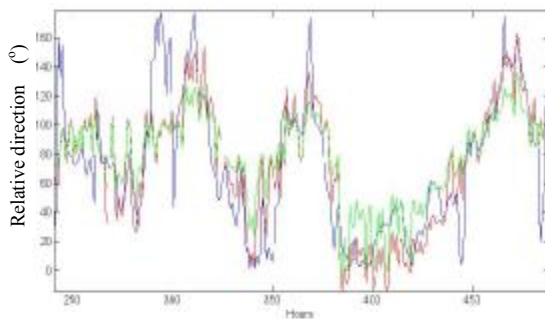
Both spatial patterns and temporal variations of surface current field were presented. Currents near coast show more complex features and higher velocities than outer sea. Results show that surface currents are highly correlated with local tides. Vorticity and Divergence were investigated for the one-year averaged total current vector field off Brittany and the one-month averaged total current field off Qingdao. There is a clockwise eddy in the mean current field off Qingdao.

5 Results of wind directions

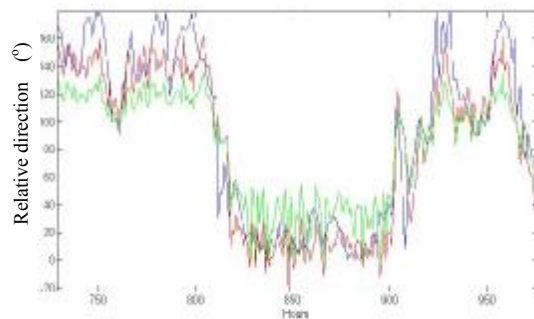
5.1 Radar inverted relative wind direction

Wind directions were measured from the single Doppler spectra collected every 20 minutes using models described in Section 2.3. Samples were taken from all the radar cells every three hours, from September 1 2007 to September 30 2008, at 30 min for station R1 and at 20 min for station R2, respectively. The maximal spectral density of both Bragg peaks were used as measurement of B^+ and B^- to provide Bragg peaks ratio. As data from station R1 are less influenced by islands, the thesis presents mainly measurements from station R1 in this section.

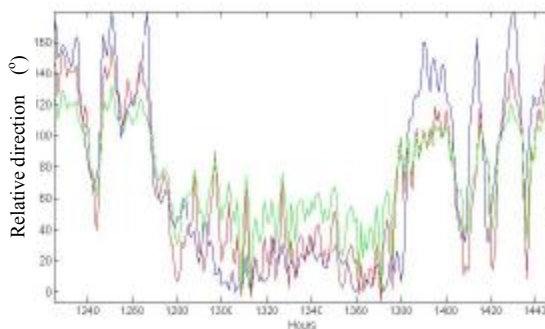
Examples of radar-inverted relative wind direction by empirical methods described in Section 2.3 are shown in Fig. 5-1. The period spans six months from October 2007 to August 2008. The radar cell is R1 (35 km, 0°). WW3 model estimations (blue curve) are used for comparison (see Section 6.1.3). In the figure, results using the model of Harlan and Georges (1974) agrees better with model data.



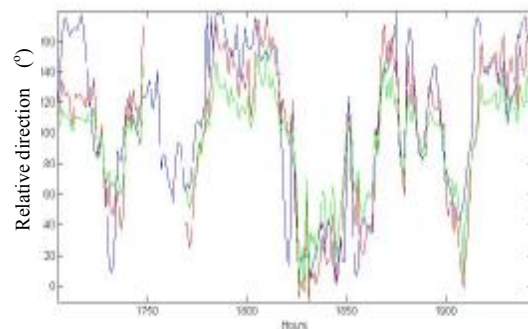
(a) October 2007



(b) December 2007



(c) February 2008



(d) April 2008

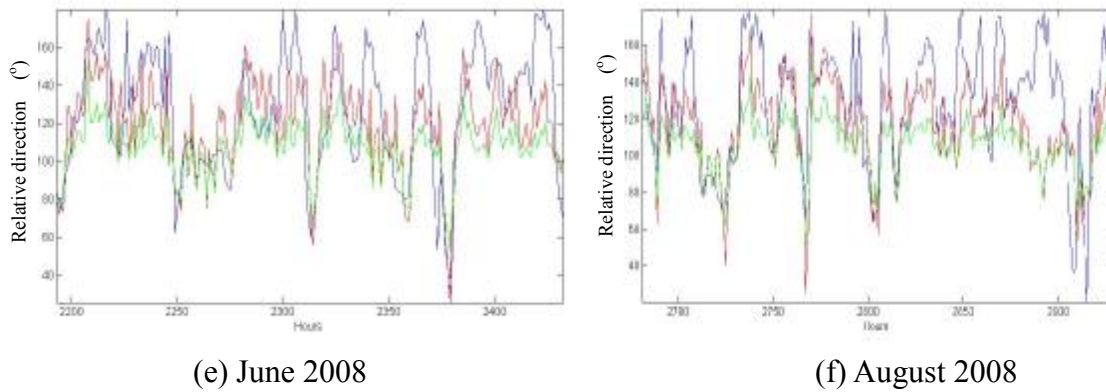
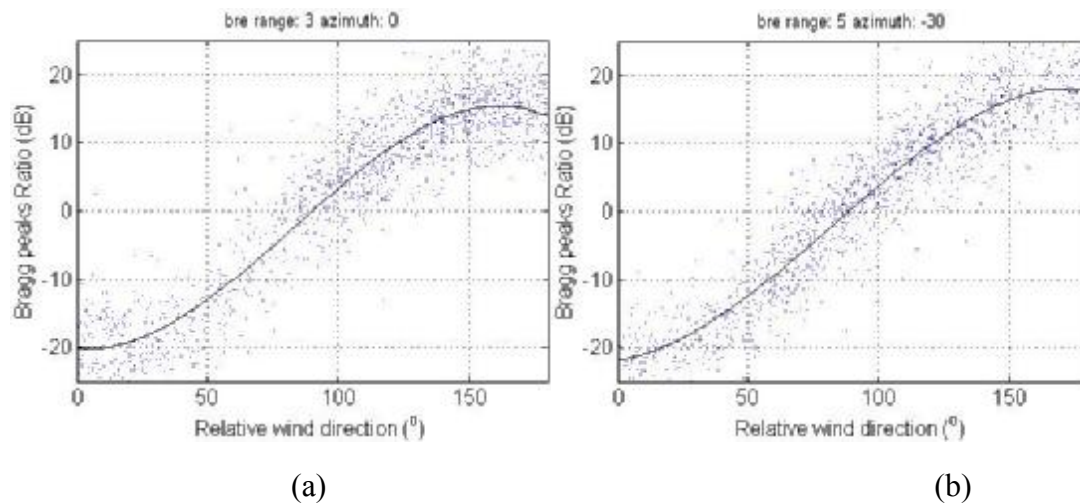


Fig. 5-1 Time series of relative wind direction. Blue curve: model estimation. Green curve: radar-inverted results using method of Long and Trizna (1973). Red curve: radar-inverted results using method of Harlan and Georges (1974).

5.2 Measurement of spreading parameter

The correspondence between radar measured Bragg peaks ratios (r_B) and model estimated relative wind directions during the whole period on several representative radar cells are shown in Fig. 5-2. Positive ratios are observed for downwind cases while negative cases are observed for upwind cases. The absolute value of the Bragg peaks ratio is larger when the radar look direction is more parallel to wind direction, either up wind or down wind. A preliminary analysis using cubic polynomial fitting is shown in each figure to show the distribution of samples.



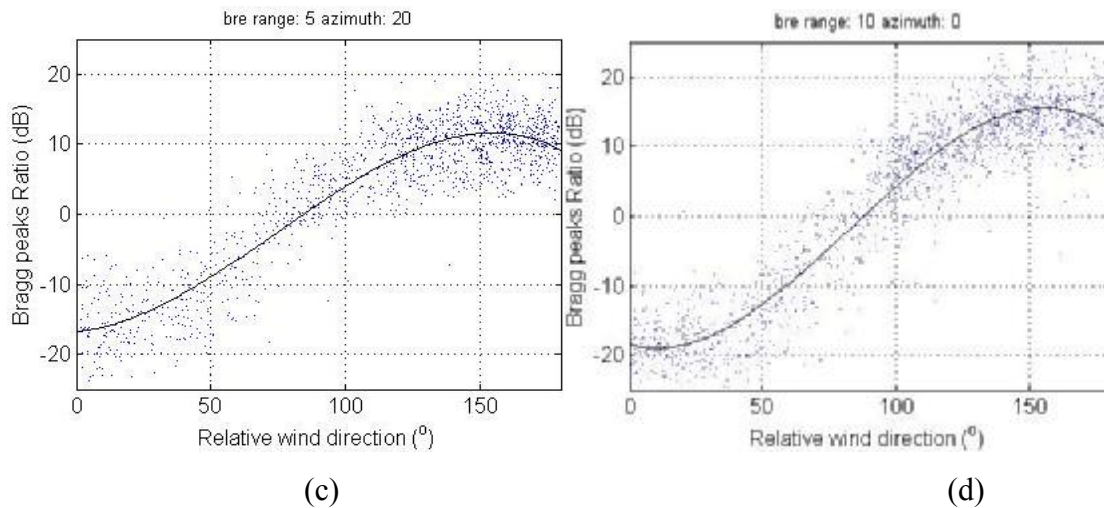
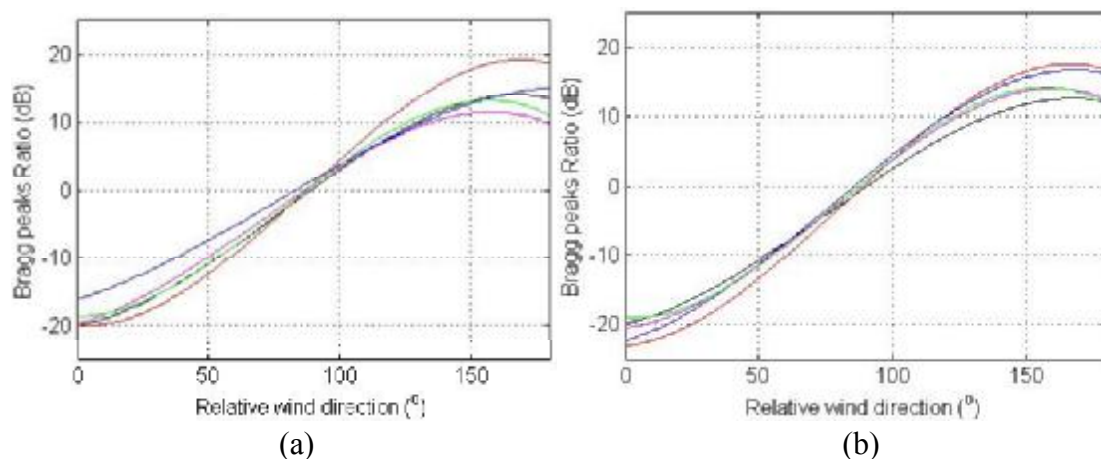


Fig. 5-2 Measurements of the correspondence between Bragg peaks ratio (in dB) and relative wind direction with respect to radar look direction during September 1 2007 - September 30 2008. Solid curve shows cubic polynomial fitting of the samples. (a) R1 (11 km, 0°); (b) R1 (23 km, -60°); (c) R1 (23 km, 0°); (d) R1 (23 km, 60°)

The variations of distribution of samples at different ranges on a same radar beam are shown in Fig. 5-3. The beams presented are spaced by 15°. At shorter ranges (black and red curves, for example), most of the fitting curves are more flat than other curves at farther ranges. The curve at middle range of 53 km (blue curve) seems to be more consistent than others for different radar beams.



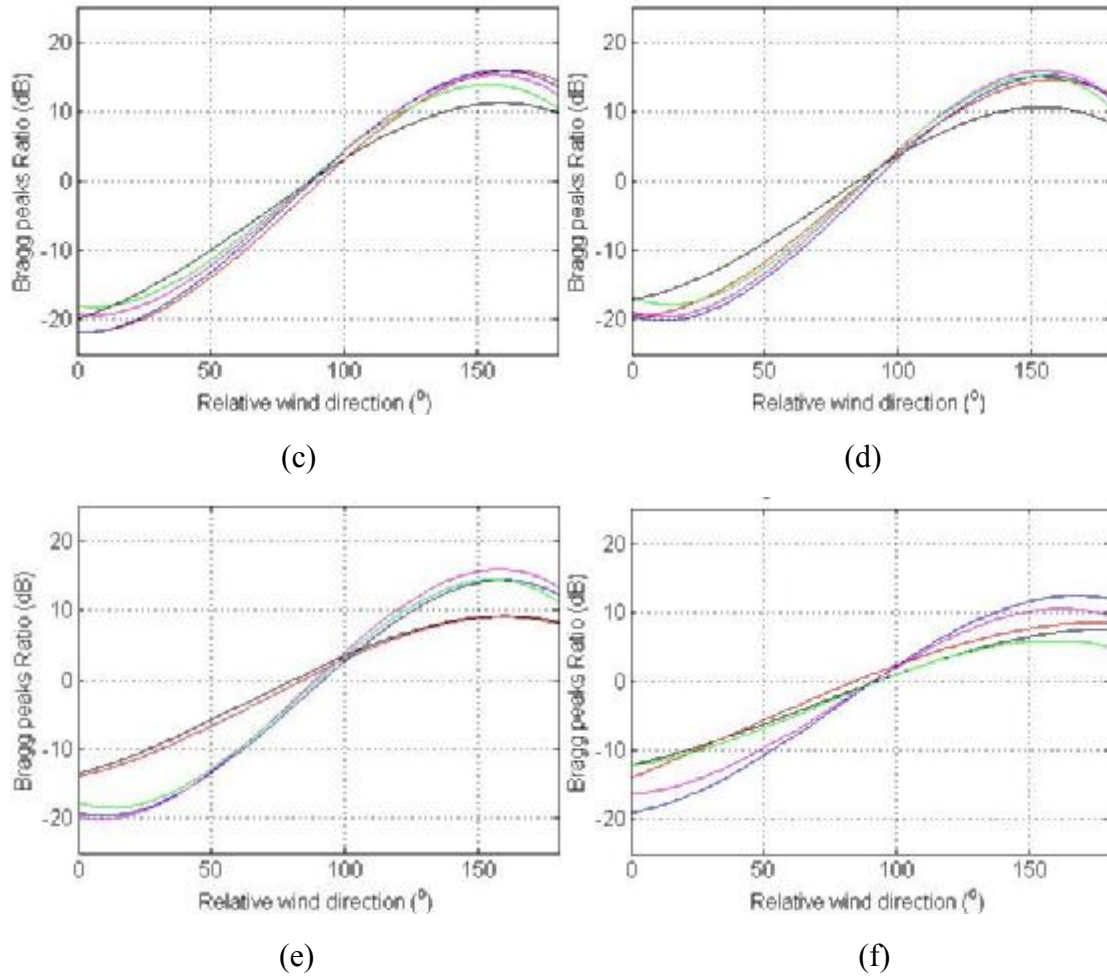


Fig. 5-3 Cubic polynomial fitting of samples of Bragg peaks ratio as function of relative wind direction at different ranges (black: 11 km; red: 23 km; blue: 53 km; mauve: 65 km; Green: 83 km) on one radar beam. (a) -35° to normal beam. (b) -20° to normal beam. (c) -5° to normal beam. (d) 10° to normal beam. (e) 25° to normal beam. (f) 40° to normal beam.

Model of Eq. (2-25) based on cardioid directional distribution and model of Eq. (2-27) with hyperbolic secant squared shape of the ocean wave spectrum were applied to compute the spreading parameter. Statistics of the results of the spreading parameter computed at the radar cell near buoy location is shown in Fig. 5-4. A mean value of the spreading parameter in the cardioid model of Eq. (2-25) is 3.92, computed by the most frequently observed 90% of samples. A mean value of the spreading parameter in the hyperbolic secant squared model of Eq. (2-27) is 1.14, computed by 90% samples in the middle part. The corresponding angular distributions ($G(q)$) for Bragg waves are shown in Fig. 5-5. The coefficient a in Eq. (2-24) takes

the value of 0.025 estimated by Cochin et al. (2005).

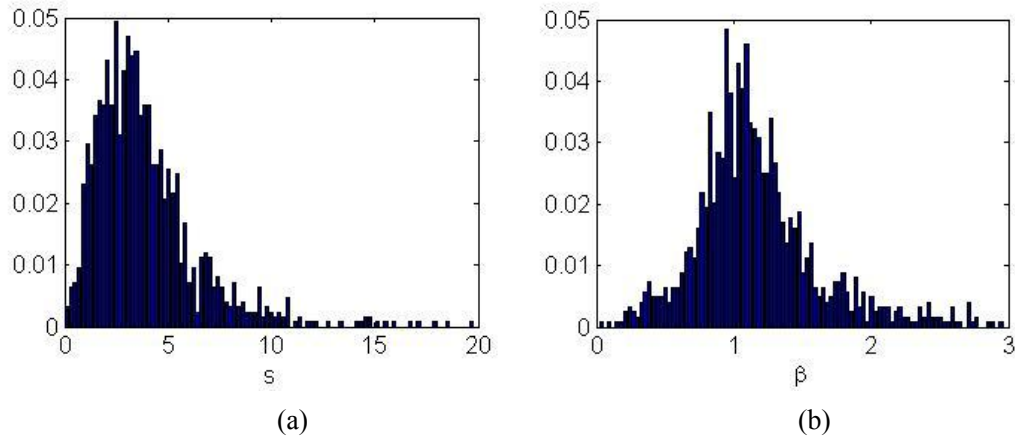


Fig. 5-4 Histograms of spreading parameters by two directional distribution models. (a) cardioid model, Eq. (2-25). (b) Hyperbolic secant squared model, Eq. (2-27).

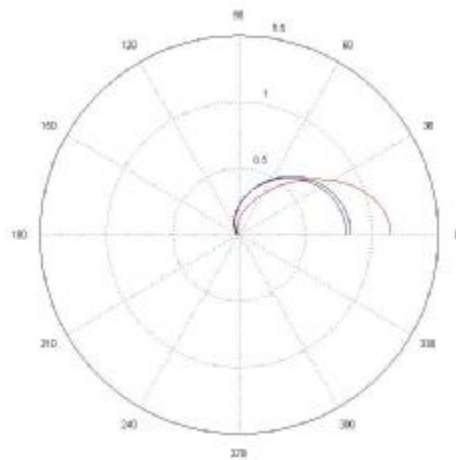


Fig 5-5 Angular distributions for Bragg waves in the Iroise sea estimated by different models. Black: Longuet-Higgins et al. (1963) (Eq. 2-23), with $s = 1.96$; Blue: Tyler et al. (1974) (Eq. 2-27), with $s = 3.92$; Red: Donelan et al. (1985) (Eq. 2-26), with $b = 1.14$.

An example of the fitting curves by cardioid and hyperbolic secant models to measurements of Bragg peaks ratio on radar cell R1 (35 km, 0°) is shown in Fig. 5-6.

Spreading parameters apply the mean values presented in Fig. 5-3. The figure shows that Dolenan model gives a better fit than the cardioid model.

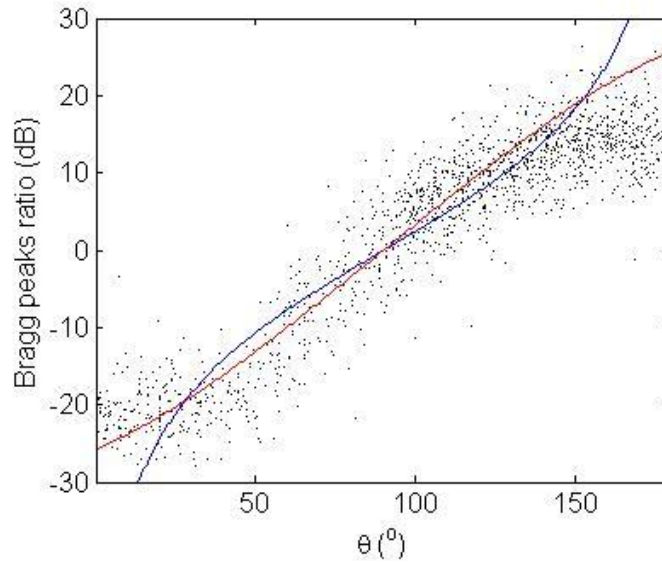


Fig. 5-6 Fitting curves of radar measurements of Bragg peaks ratio versus model provided relative wind direction. Samples are shown in black dots. Blue and red curves are the fitting curve using models of Eq. (2-25) and Eq. (2-27), respectively.

5.3 Summary

Radar measurements of Bragg peaks ratio were used to obtain relative wind direction with respect to radar look direction, using empirical methods proposed by Long and Trizna (1973) and Harlan and Georges (1974). Both methods give results with the same variation with model data. Results from the latter method agree better with model values.

The spreading parameter in the directional distribution was measured using cardioid model (Cochin et al. 2005) and hyperbolic secant squared model (Donelan et al. 1985). The former model gives a mean spreading parameter of 3.92 for the Iroise Sea. The latter model gives a mean spreading parameter of 1.14.

6 Results of swell

The thesis focuses on swell parameters inverted from HFR. Swell frequency, direction and significant waveheight are derived using the methodologies described in Section 2.4. It is pointed out in Section 3.4 that the lower and upper limits of our WERA system measurement ability are 0.045 Hz and 0.126 Hz, respectively (Section 3.4).

6.1 Swell frequencies

6.1.1 Consistency of both radar measurements

There is a large overlapped area between the two radar stations (Fig. 3-1). Pairs of radar cells from both stations separating less than 3 km are considered as common radar cells. There are 313 pairs of common cells out of the total number of 575 cells for each station. Because of different distances to the receiving antennas, different radar bearings and different circumstances in paths of radar signals, the ultimate measurements obtained by both radar stations at the same location may vary from each other. Thus the thesis verified the consistency of radar measurements between the two stations on common radar cells.

Radar-inverted swell frequencies are noted as F_{sr1} and F_{sr2} , for station R1 and R2, respectively. Results from all common cells during the whole 13-month period are compared in Fig. 6-1, with regression analysis listed in Table 6-1. There are 10839 samples, less than that presented in Wang et al. (2014) as further quality control were implemented (Section 3.4). Scatterplot (Fig. 6-1 a) shows that the two measurements agree well with each other in general. Outliers exist mainly in high frequency range. Fig. 6-1 (b) shows the comparison in intervals. Frequencies are divided into intervals of 0.03 Hz wide from F_{smin} to F_{smax} . The histograms show relative numbers of samples, which are the absolute numbers in intervals divided by a constant of 24000 to fit the figure. The statistical values presented in the figures are at intervals with relative number of samples of over 5%. The histograms show that the most frequently observed swell frequency is in the range 0.07-0.09 Hz, centered at about 0.08 Hz. Standard deviations (STD) of F_{sr1} and F_{sr2} are computed separately in frequency intervals. Values of STD are shown in crosses centered at the equal line. In the range with larger number of samples, values of STD are smaller. Both measurements have

similar STDs for all the frequency intervals with R2 showing a slightly larger STD than R1. However, the observed STD values tend to increase with F_s . Fluctuations at high F_s values are interpreted as the consequence of the decrease in the number of samples. However, at low swell frequency the scatter is quite small even with fewer samples.

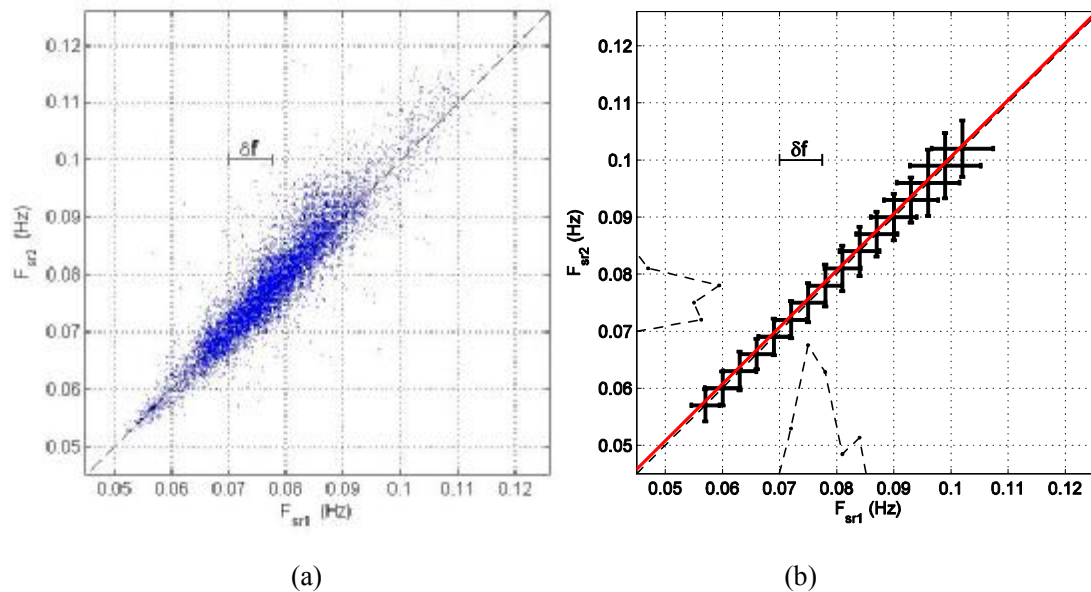


Fig. 6-1 Comparison of swell frequencies measured by two radar stations at common cells during the whole 13-month period. (a) Scatterplot. (b) Statistical analysis in 0.003 Hz intervals. Dashed diagonal line is of equal frequency. Red solid line shows the perpendicular regression line. Horizontal and Vertical lines of error crosses depicts \pm STD of F_{sr2} (F_{sr1}) centered at centers of intervals. Dashed curves with dots are histograms for F_{sr1} (y-axis) and F_{sr2} (x-axis), respectively, divided by a constant of 24000 to fit the figure.

The regression analysis shown in Fig. 6-1 (b) and listed in Table 6-1 uses an improved way of perpendicular regression. The linear regression way calculates the deviation between points and the regression line and finds a least-squares resolution. However, there is a subject choice of the y-variable and x-variable. It gives different results with exchange of the two variables. The perpendicular regression way considers the uncertainties in both measurements. It computes the perpendicular distance from points to the line and finds the least-squares resolution. Both swell

frequency estimates agree well with a regression line close to the ideal equal line and a high correlation coefficient close to 1. The slope of the regression line is very close to the equal line. They are highly correlated with each other. The standard deviation of difference from the regression line (STD_L) is introduced to quantify the general measurement error (Yoshikawa et al. 2006). STD_L is 0.0035 Hz.

a (Hz)	b	R_e	RMSD(Hz)	STD _L (Hz)	n	p_1 (%)	p_2 (%)
0.00	1.00	0.92	0.0036	0.0035	10839	76	95

Table 6-1 Perpendicular regression analysis of F_{sr1} and F_{sr2} . a , b are coefficients of the regression equation ($y = a + bx$). R_e is the correlation coefficient. RMSD is the root-mean-square difference. STD_L is STD of y -variable from regression line. n is the number of samples. p_1 (p_2) is the proportion of samples inside \pm STD_L (± 2 STD_L) from regression line.

The exact values of STDs of F_{sr1} and F_{sr2} in intervals are listed in Table 6-2 and plotted in Fig. 6-2. STDs of both stations, STD1 and STD2, are about 0.003 Hz – 0.004 Hz for low frequency swell cases (<0.01 Hz). For high frequency cases, STDs are larger. STD1 reaches a maximum value of 0.0062 Hz for the interval of 0.00975-0.0105 Hz. The difference between STD1 and STD2 are always smaller than 0.001 Hz. Most of the samples appear in the intervals from 0.0705 Hz to 0.0795 Hz. STDs in these intervals are both small. In the extreme intervals, STDs are relatively large, especially the high-frequency range (≥ 0.01 Hz).

F_{si} (Hz)	STD1 (Hz)	N1	STD2 (Hz)	N2	STD1-STD2 (Hz)	STD1/ F_{si} (%)	STD2/ F_{si} (%)
0.057	0.0025	157	0.0028	129	0.0003	4.33	4.94
0.060	0.0031	146	0.0030	176	-0.0001	5.19	4.97
0.063	0.0029	300	0.0034	241	0.0005	4.67	5.38
0.066	0.0030	647	0.0027	698	-0.0003	4.47	4.05

0.069	0.0027	953	0.0032	989	0.0005	3.95	4.64
0.072	0.0028	1351	0.0033	1270	0.0005	3.82	4.52
0.075	0.0030	1321	0.0034	1621	0.0004	4.06	4.56
0.078	0.0030	1427	0.0037	1508	0.0007	3.79	4.74
0.081	0.0032	1128	0.0040	1162	0.0008	3.92	4.94
0.084	0.0035	1074	0.0043	1232	0.0008	4.18	5.15
0.087	0.0036	859	0.0039	835	0.0003	4.16	4.51
0.090	0.0040	627	0.0041	471	0.0000	4.47	4.50
0.093	0.0047	477	0.0039	302	-0.0008	5.08	4.22
0.096	0.0055	202	0.0058	113	0.0003	5.71	6.04
0.099	0.0062	114	0.0057	88	-0.0004	6.24	5.79
0.102	0.0054	89	0.0049	96	-0.0004	5.27	4.85

Table 6-2 Values of STD of swell frequencies measurements in intervals. F_{si} is the center value of frequency intervals. STD1 and STD2 are STDs of F_{sr1} and F_{sr2} , respectively. N1 and N2 are numbers of samples in each interval.

Fig. 6-2 shows that absolute value of STD of radar measurements increases with swell frequency, while the relative STD (divided by swell frequency) is larger for low- and high-frequency swell and is smaller for moderate swell. The variation of relative STD divided by center values of frequency intervals varies between 3.5% and 6.5%. Measurements from station R2 gives larger uncertainty indicated by both STD and relative STD. This can be partially explained by the locations of common cells. Ushant Island and Molène archipelago in the north of the overlapped area interrupt the propagation of radar signals transmitted and received by station R2, whereas most of the overlapped area is an open ocean for station R1 with less influences of archipelago.

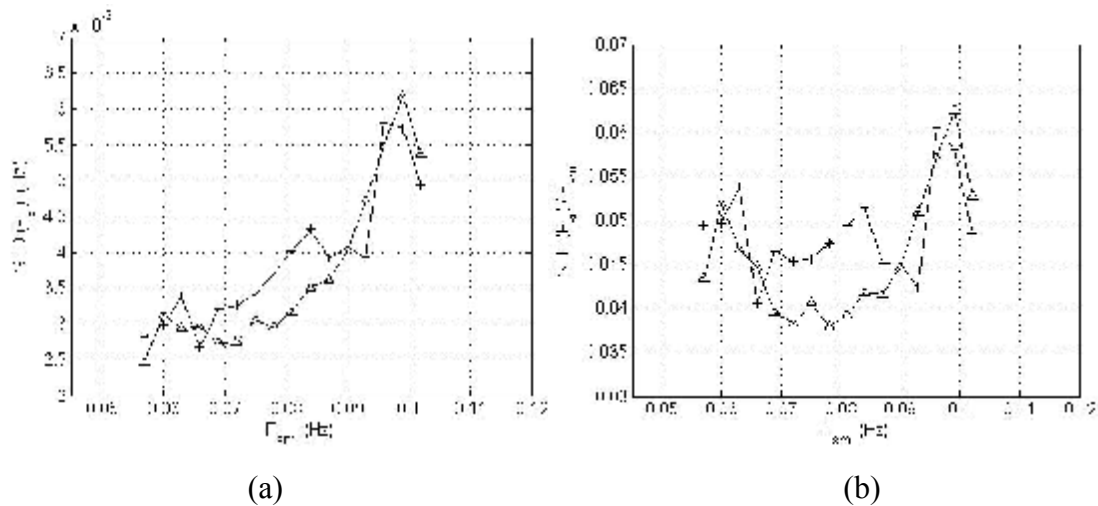


Fig. 6-2 Comparison of uncertainties of swell frequency measurements by the two stations at common cells during the 13-month period. (a) Standard deviations of F_{sr1} (triangle) and F_{sr2} (cross) in 0.003 Hz intervals of F_{sm} . (b) Relative standard deviations of F_{sr1} (triangle) and F_{sr2} (cross) normalized by central value of intervals.

These results demonstrate the consistency of both radar measurements both in mean value and in STD. One consequence is that, for swell frequency measurement, the two radars can be used in a complementary way in case of failure of one of them or, more generally, for the improvement of F_s estimate.

6.1.2 Comparison with buoy data

Radar inverted swell frequency (F_{sr}) are compared to buoy measured swell frequency (F_{sb}). Buoy data comes from “Pierres Noires” mooring ($-4^{\circ}58'1''$, $48^{\circ}17'42''$, see Fig. 1). This is the only available buoy data to compare with our radar measurements. The location is shown in Fig. 6-3. The water depth for the buoy mooring is 50.3 m. The closest radar cell of station R1 locates 1.14 km from the buoy at R1(35 km, -30°); the closest radar cell of station R2 locates 0.74 km from the buoy at R2 (29 km, 35°). However, data from station R2 suffers from island shadowing.

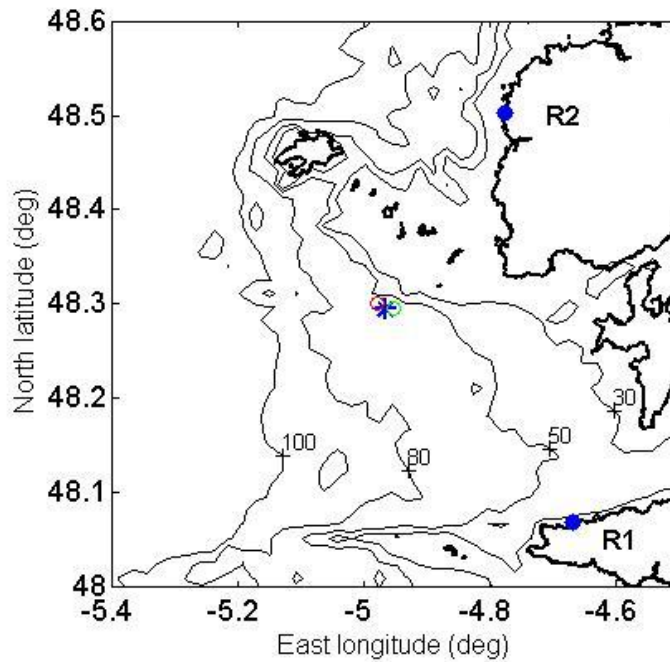
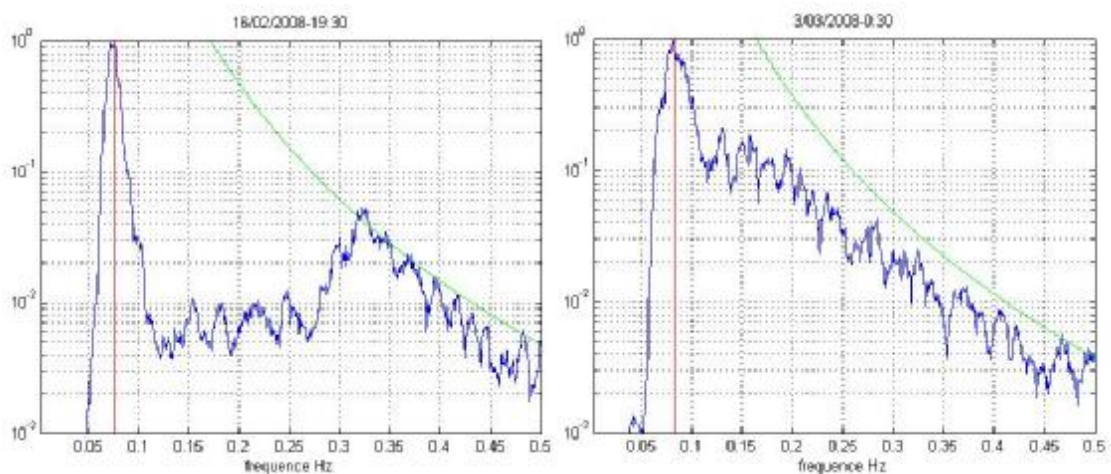


Fig. 6-3 Location of buoy (blue star). Green and red circles are the closest radar cells of station R1 and R2, respectively, to the site of buoy. Isobaths show water depths of 30 m, 50 m, 80 m and 100 m.

Buoy data available for comparison with radar results spans from February to July, 2008. The non-directional ocean wave spectrum was computed every half an hour, Fig. 6-4. The thesis identified the spectral peak by the one-dimensional method which uses a criterion on the wave frequency (Portilla et al. 2009). The range of swell frequency was determined according to the capability of the HF radar technique, 0.045 - 0.126 Hz.

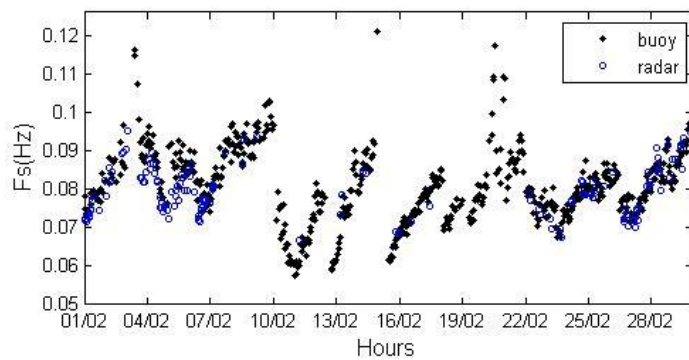


(a) 2008-02-16 19:30

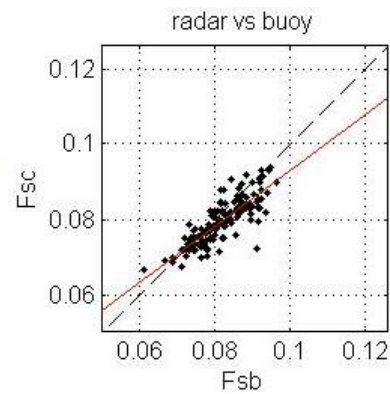
(b) 2008-03-03 0:30

Fig. 6-4 Ocean wave spectra measured by buoy (blue curve). Green curve is the simulation of non-directional PM spectrum. Red vertical line shows the identified swell spectral peak.

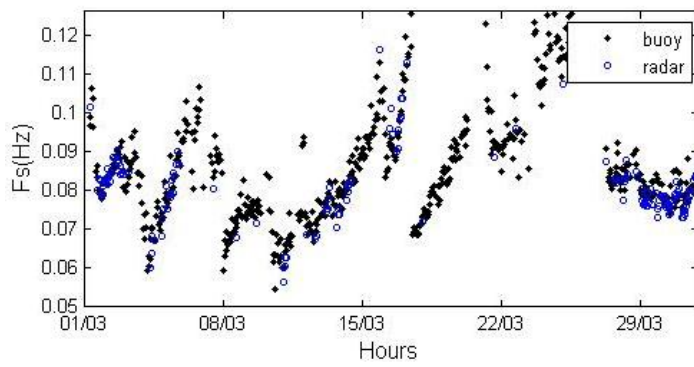
Comparisons of radar-inverted and buoy-measured swell frequencies are shown in Fig. 6-5 with linear regression analysis listed in Table 6-3. Time series and scatterplots show good agreements with the two measurements when F_{sr} is available. Regression lines illustrate that F_{sr} are generally lower than F_{sb} . Radar measures most of the swell cases during February - March when buoy data show low to moderate swell frequencies. From May to July, swell frequencies are in the higher range indicated by buoy while radar presents much less measurements than before. This is correlated with occurrences of winter storms in the Atlantic Ocean. These facts imply that radar works better for low to moderate frequency swell. The efficiency of HFR decreases significantly for high frequency swell. In general, RMSD increases while number of samples decreases from February to July.



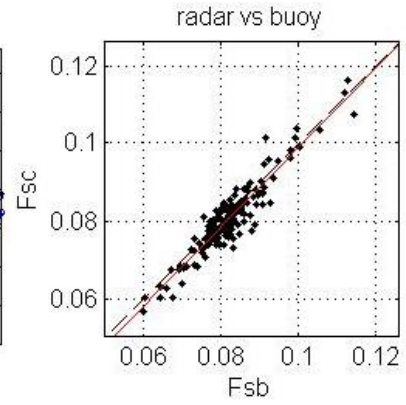
(a) February



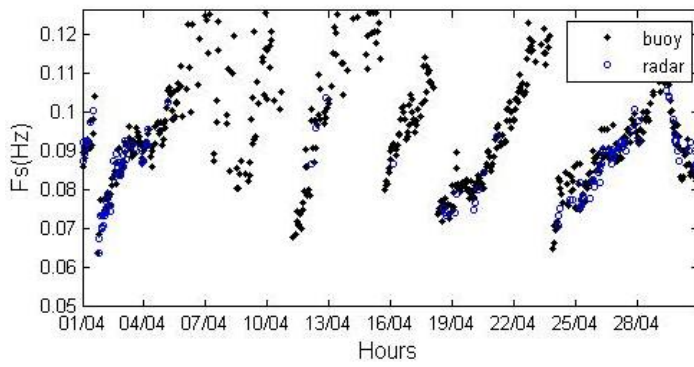
(g) February



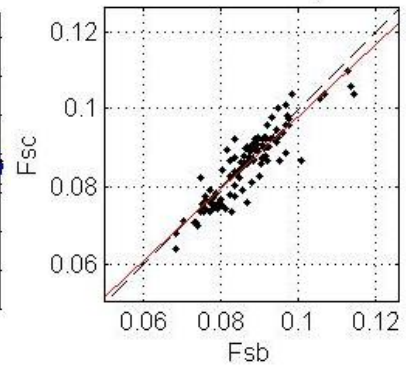
(b) March



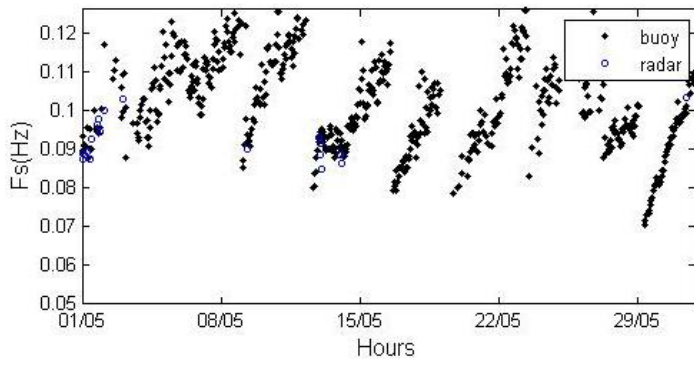
(h) March



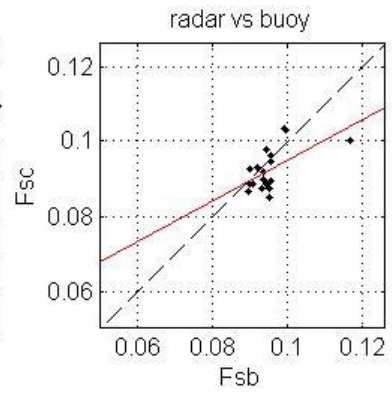
(c) April



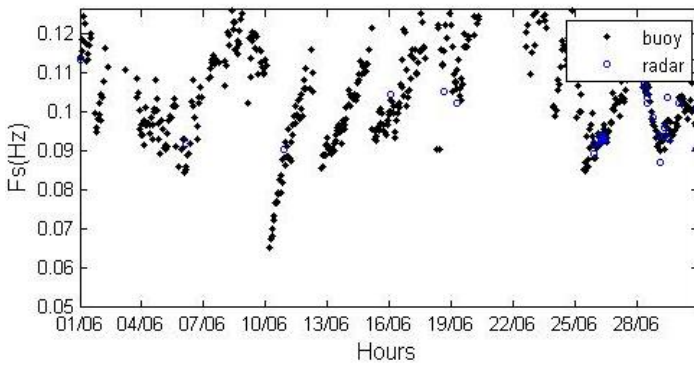
(i) April



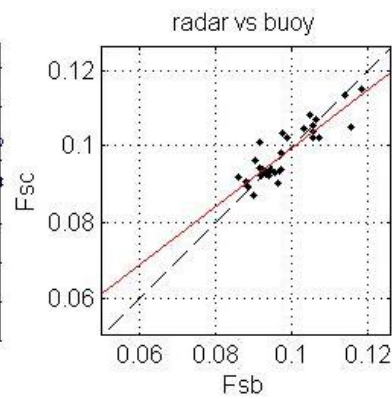
(d) May



(j) May



(e) June



(k) June

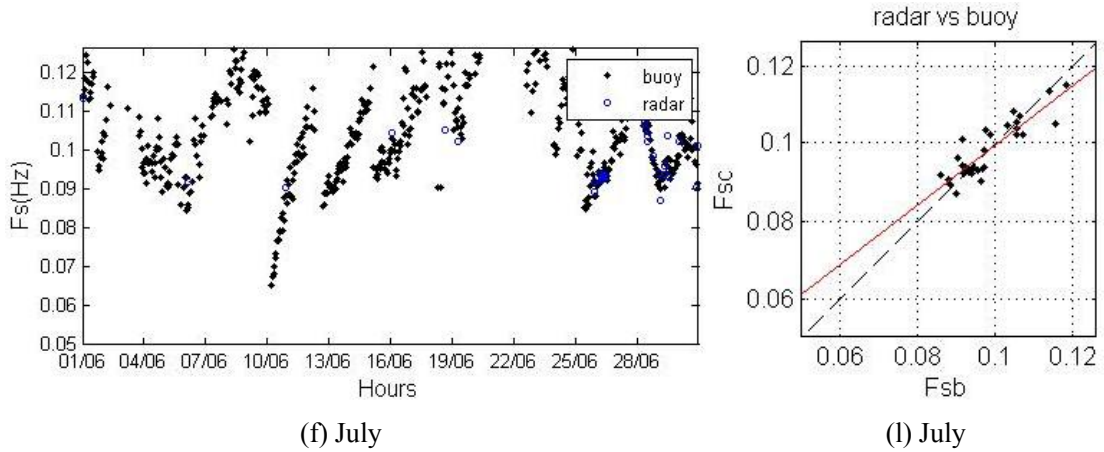


Fig. 6-5 Comparisons between radar and buoy measurements of swell frequency by month in 2008. (a-f): Time series. Black dots are buoy measurements. Blues circles are radar-inverted results. (g-l): Scatterplots. Red line shows the linear regression line.

2008	a (Hz)	b	R_e	RMSD(Hz)	STDL(Hz)	n
February	0.02	0.74	0.83	0.0045	0.0034	132
March	-0.00	1.02	0.94	0.0036	0.0033	154
April	0.00	0.94	0.90	0.0041	0.0040	108
May	0.04	0.54	0.59	0.0058	0.0045	19
June	0.02	0.77	0.88	0.0040	0.0036	30
July	0.01	0.88	0.87	0.0078	0.0070	35

Table 6-3 Linear regression analysis of radar and buoy measurements of swell frequency by months in 2008. Parameters are the same as in Table 6-1.

Scatterplot of radar measurements and buoy measurements during the whole 6-month period is shown in Fig. 6-6. There are 478 samples in all. Most swell cases have frequencies of 0.07 – 0.1 Hz. There are more (less) cases with F_{sr} lower (higher) than F_{sb} . There are three outliers at buoy frequency of 0.091 Hz, 0.109 Hz and 0.114 Hz, where radar measurements are much lower. With most swell cases observed in the frequency range of 0.07 - 0.1 Hz, radar and buoy measurements agree with each other quite well and the scatter is not large. In low frequency range of 0.05 -

0.07 Hz, the two measurements agree well but there are very few samples. In the high frequency range with F_{sb} over 0.01 Hz, the two measurements are much more scattered than other ranges and severe outliers appear. The parameters the linear regression line in the figure is listed in Table 6-4. The correlation between the two measurements is high with correlation coefficient of 0.92. The RMSD and STDL are in the scale of half Doppler frequency resolution (0.0075 Hz).

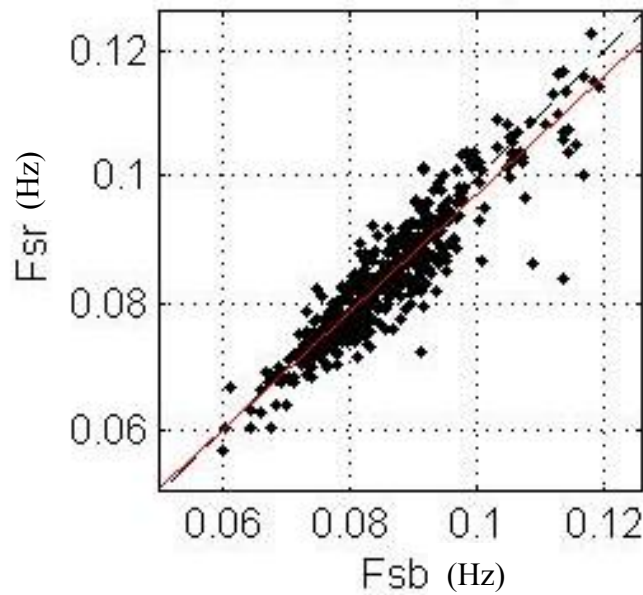


Fig. 6-6 Scatterplots of radar and buoy measurements of swell frequency during February - July, 2008.

a (Hz)	b	R_e	RMSD(Hz)	STD(L)(Hz)	n	p_1	p_2
0.00	0.93	0.92	0.0045	0.0041	478	73%	96%

Table 6-4 Linear regression analysis of radar and buoy measurements of swell frequency during February - July, 2008. Parameters are the same as in Table 6-1.

6.1.3 Comparison with model data

Model estimated swell frequency calculated by the wave model WAVEWATCH III (Tolman 2008), F_{sm} , were used to compare with radar inverted results (F_{sr}) on

common radar cells over the period considered. This dataset has large spatial and temporal coverage, which is consistent with the radar database. Model parameterization corresponds to Ardhuin et al. (2010). The model database is available online (<ftp://ftp.ifremer.fr/ifremer/cersat/products/gridded/wavewatch3/HINDCAST/>). The partition scheme divides the ocean surface waves into first, second and third energetic wave components (e. g. Hanson and Phillips 2001; Portilla et al. 2009). We considered two parameters of the partitions, namely $F_p^{(1)}$, the peak frequency of the first most energetic wave system (wind sea most the time) and $F_p^{(2)}$, the peak frequency of the second most energetic wave system (primary swell). The swell frequency value used for comparison with radar derived F_s values is the value of $F_p^{(1)}$ or $F_p^{(2)}$ falling in our defined range of swell frequencies (F_{smin} to F_{smax}). If both frequencies are in the interval, $F_p^{(1)}$ is taken.

One example of the wave systems and radar measurements in time series is shown in Fig. 6-7. The radar cell lies 29 km from R1 along the normal beam direction. The first two most energetic wave systems are shown in comparison with radar measurements. Most of the time, F_{sr} agrees well with the second energetic wave frequency $F_p^{(2)}$. The exceptional points appear only on days 25 and 27 when F_{sr} corresponds to $F_p^{(1)}$, as $F_p^{(1)}$ belongs to the frequency region of F_{smin} to F_{smax} . This figure illustrates that our selection criterion of swell frequency from model partition data is reasonable. It is noteworthy that each identified swell event (depicted in slash lines) experiences a quasi-linear increase of frequency with time. This phenomenon is observed most of the time in our data and can be interpreted by the dispersive nature of ocean waves: the velocity of ocean waves generated by a distant storm and measured at a fixed location decreases, and then frequency increases, linearly with time (Hanson and Phillips 2001).

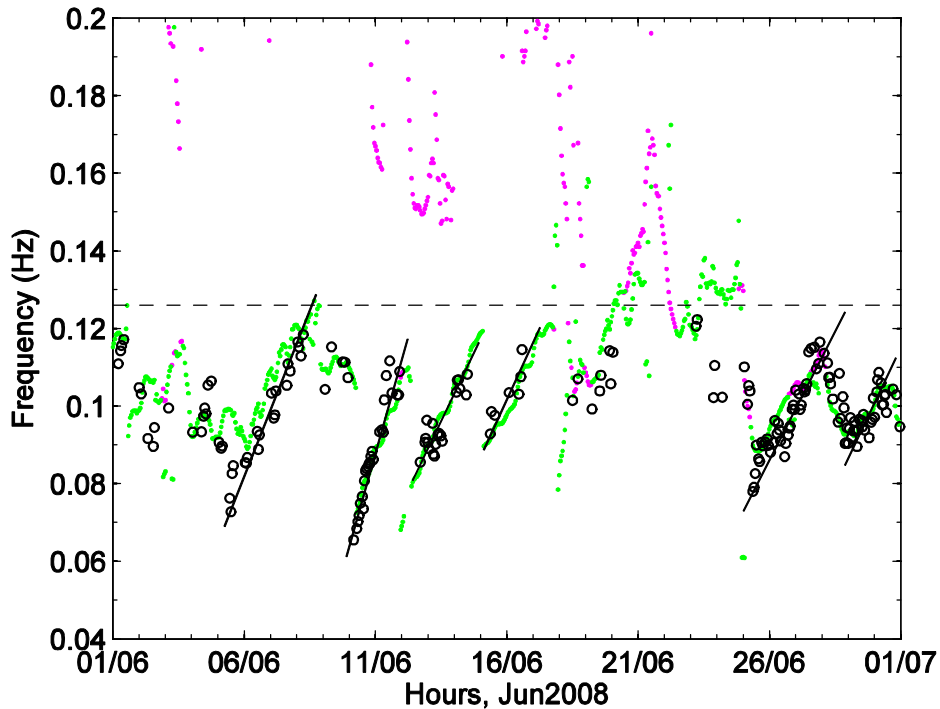
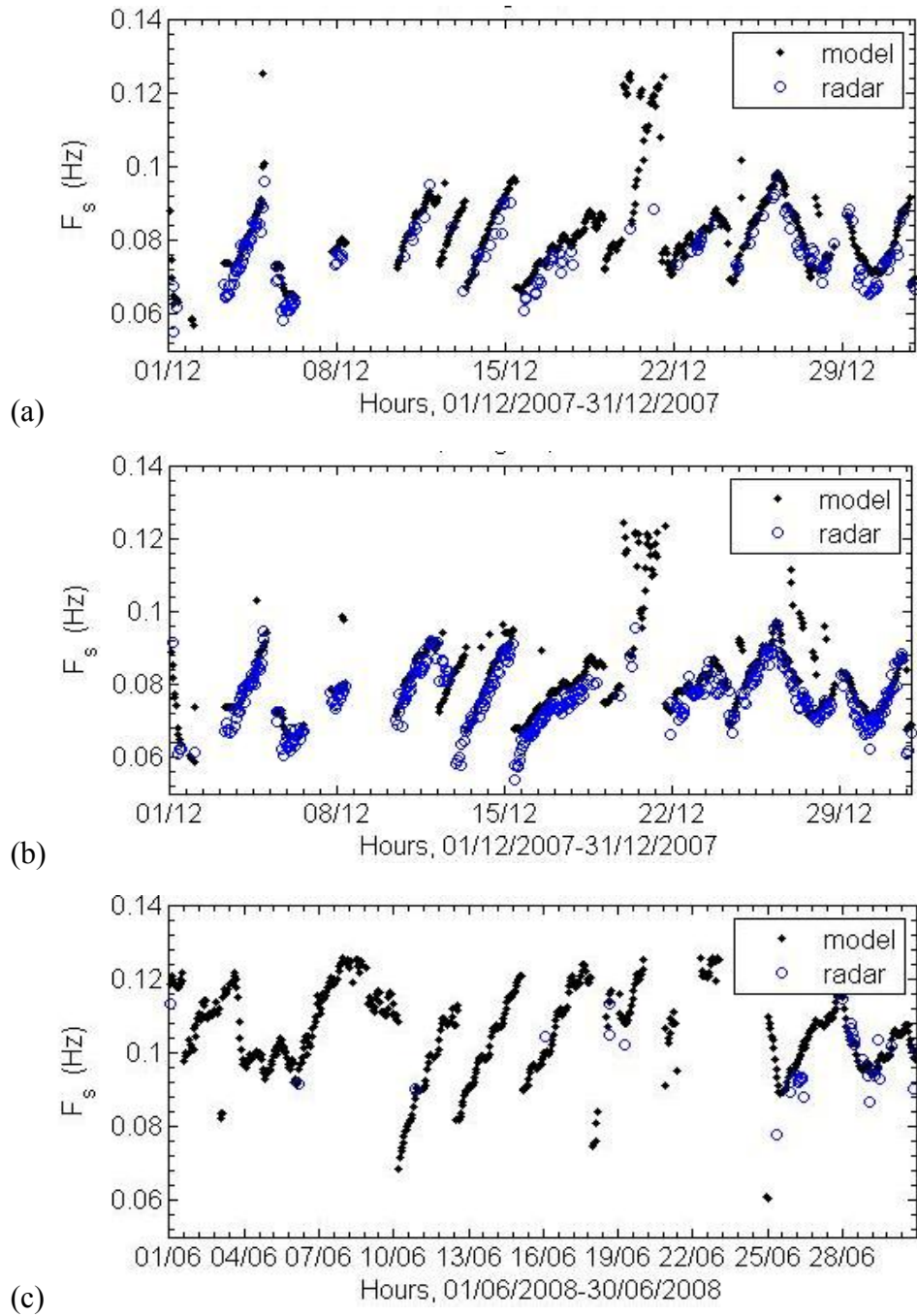


Fig. 6-7 Time series of radar (open circle) and model (magenta dot: $F_p^{(1)}$, green dot: $F_p^{(2)}$) estimated swell frequency in June 2008 at radar cell R1 (29 km, 0°). Solid lines mark out swell events. Dashed horizontal line shows swell frequency upper limit of 0.126 Hz.

Comparisons between radar estimates and selected model estimates of swell frequency are shown in time series in Fig. 6-8. These examples come from two radar cells in two specific months. One cell is the near radar cell to the location of buoy (Fig. 6-8 a, c). The other is a representative cell R1 (23 km, -15°) with large temporal data coverage (Fig. 6-8 b, d). The two months are selected one in winter, December 2007, and the other in summer, June 2008. In both months, measurements from the nearer radar cell agree very well with model estimations, with plenty of samples. There are fewer samples from the farther radar cell. Longer path definitely brings larger losses of the power of electromagnetic waves due to attenuation. In winter, the farther radar cell measures a good number of samples and the measurements agree well with model values. There are few measurements in summer time in 2008 on the farther radar cell. During that time, radar measurements obtained in the nearer cell also reduce agreement with model estimates. It is observed from model values that swell frequencies are generally much higher in June 2008 than in December 2007. The

increase of swell frequency might be one of the potential reasons for the decline of radar measurements as discussed in Section 6.1.2. The annual trend is better seen in Fig. 6-8 (e).



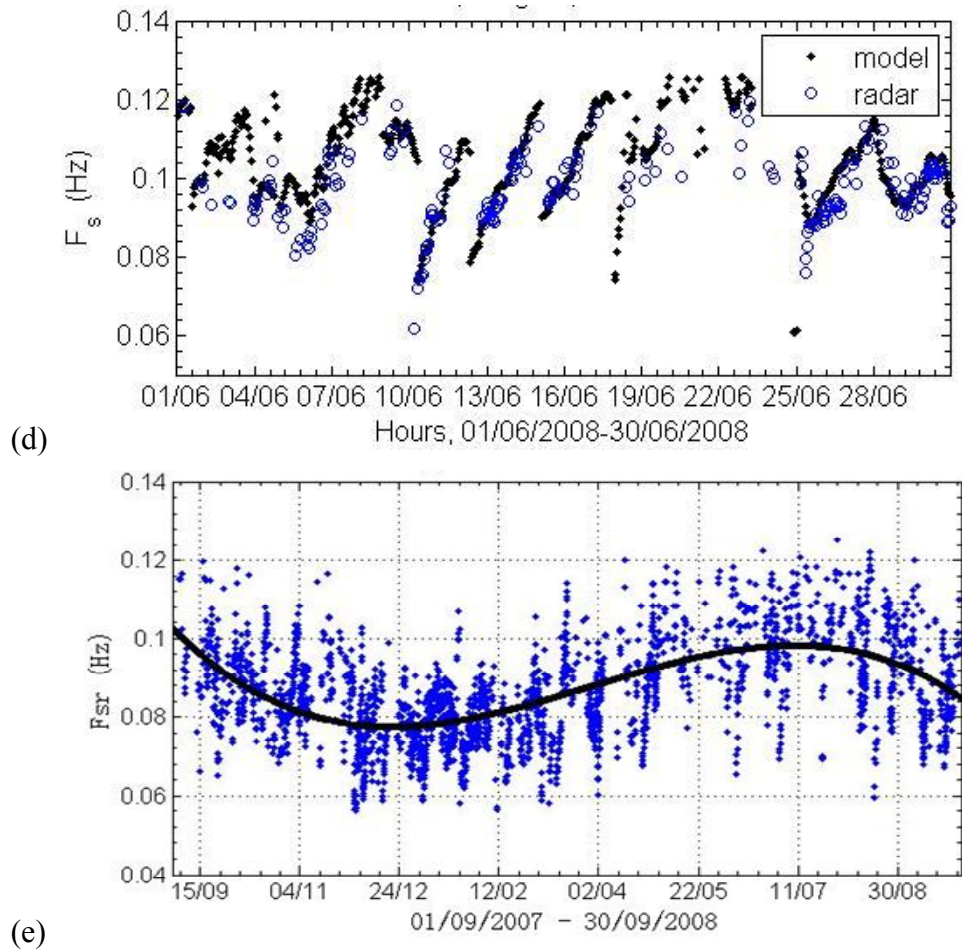


Fig. 6-8 Time series of radar and model estimated swell frequency. (a) Radar cell R1 (35 km, -30°), December 2007. (b) Radar cell R1 (23 km, -15°), December 2007. (c) Radar cell R1 (35 km, -30°), June 2008. (d) Radar cell R1 (23 km, -15°), June 2008. (e) F_{sr} at Radar cell R1 (29 km, 0°), September 2007 - September 2008. The black curve is the 3rd order polynomial fitting curve.

Comparisons of radar and model estimates of swell frequency during the whole 13-month period considering all radar cells are scatter plotted in Fig. 6-9 (a) and Fig. 6-9 (b) for station R1 and R2, respectively. Linear regression analyses are listed in Table 6-5.

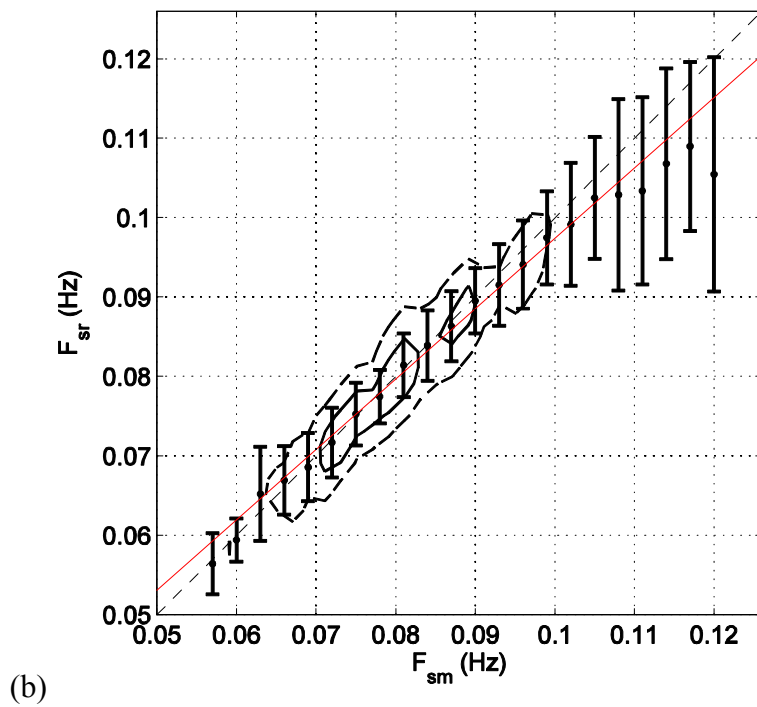
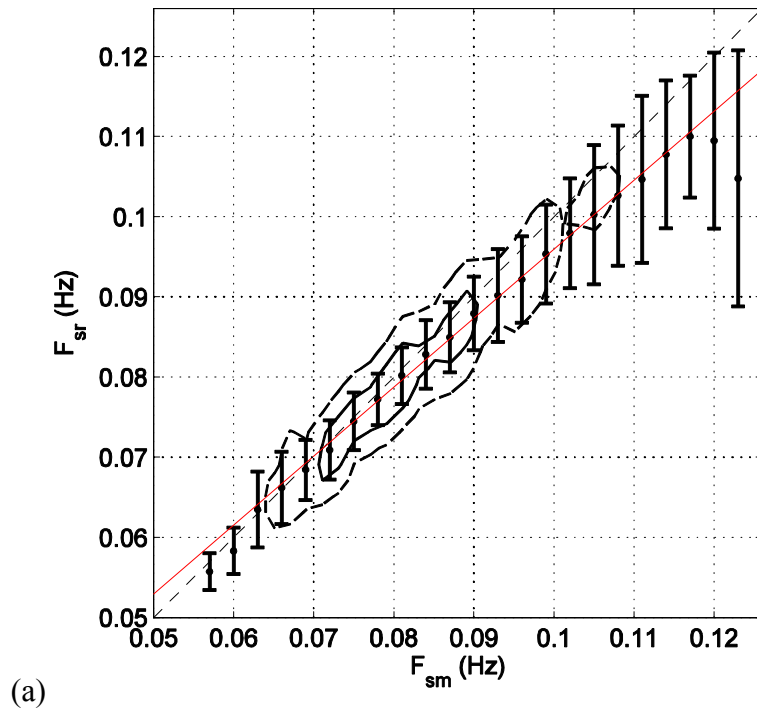


Fig. 6-9 Comparison of F_{sr} and F_{sm} for station R1 (a) and station R2 (b). Dots on central bold curve are mean values of F_{sr} in 0.003 Hz intervals. Bars depict \pm STD with respect to the mean. Dashed diagonal line is of equal frequency. Red solid line shows the regression line. Dashed and solid contours indicate relative sample density of 10% and 40%, respectively.

Mean values and standard deviations of F_{sr} are calculated in 0.003 Hz frequency intervals of F_{sm} . The minimum number of samples in an interval is required to be 5% of the number maximum. Number of samples is counted in a mesh of the scatter plot with a grid step a bit more precise (0.002 Hz). The ratio of the sample number in one mesh cell to the number maximum is defined as relative data density, shown in contours. As the thesis uses more rules for the quality control of spectra (Section 3.4), the number of samples decreases than what presented in Wang et al. (2014). A percentage of 78% (41%) of data lie within the relative density contour of 10% (40%) for station R1 and there are 69% of radar measurements within F_{sm} interval of 0.07 - 0.09 Hz. A percentage of 78% (36%) of data lie within the relative density contour of 10% (40%) for station R2 and there are 74% of radar measurements within F_{sm} interval of 0.07 - 0.09 Hz. The overall comparison considering both stations shows that F_{sr} and F_{sm} are in good agreement at low frequencies, typically < 0.09 Hz. At higher frequencies, F_{sm} values tend to exceed radar frequency values and STD dramatically increases. Mean values of radar and model estimates differ by less than 0.0013 Hz for $F_{sm} < 0.1$ Hz (period > 10 s) and by more for $F_{sm} > 0.1$ Hz. In the former range, the STD values are also small, whereas in the latter range they are much larger. The large number of samples, more than 300000, makes the total comparison statistically significant. The STDL value of the overall comparison, 0.0052 Hz, can be considered representative of the difference between radar and model estimates. It is typically 6.5% of F_s . The majority of data (82%) lie within \pm STDL from regression line.

Station	a (Hz)	b	R_e	RMSD(Hz)	STD(L)(Hz)	n	p_1 (%)	p_2 (%)
R1	0.010	0.860	0.90	0.0058	0.0052	198948	82	96
R2	0.009	0.887	0.89	0.0053	0.0051	118742	82	96
R1&R2	0.010	0.865	0.90	0.0056	0.0052	317690	82	96

Table 6-5 Linear regression analysis for the comparisons of radar and model estimates of swell frequency during September 1 2007 - September 30 2008. Parameters are the same as in Table 6-1.

The differences between F_{sr} and F_{sm} during the 13-month period are studied on each radar cell, Fig. 6-10. Each cell shown in the figure has at least 200 samples. Mean values of F_{sr} minus F_{sm} measured by station R1 are smaller than those measured by station R2 (Fig. 6-10 a, b). On average, radar estimates are lower (higher) than model estimates near (far from) radar stations.

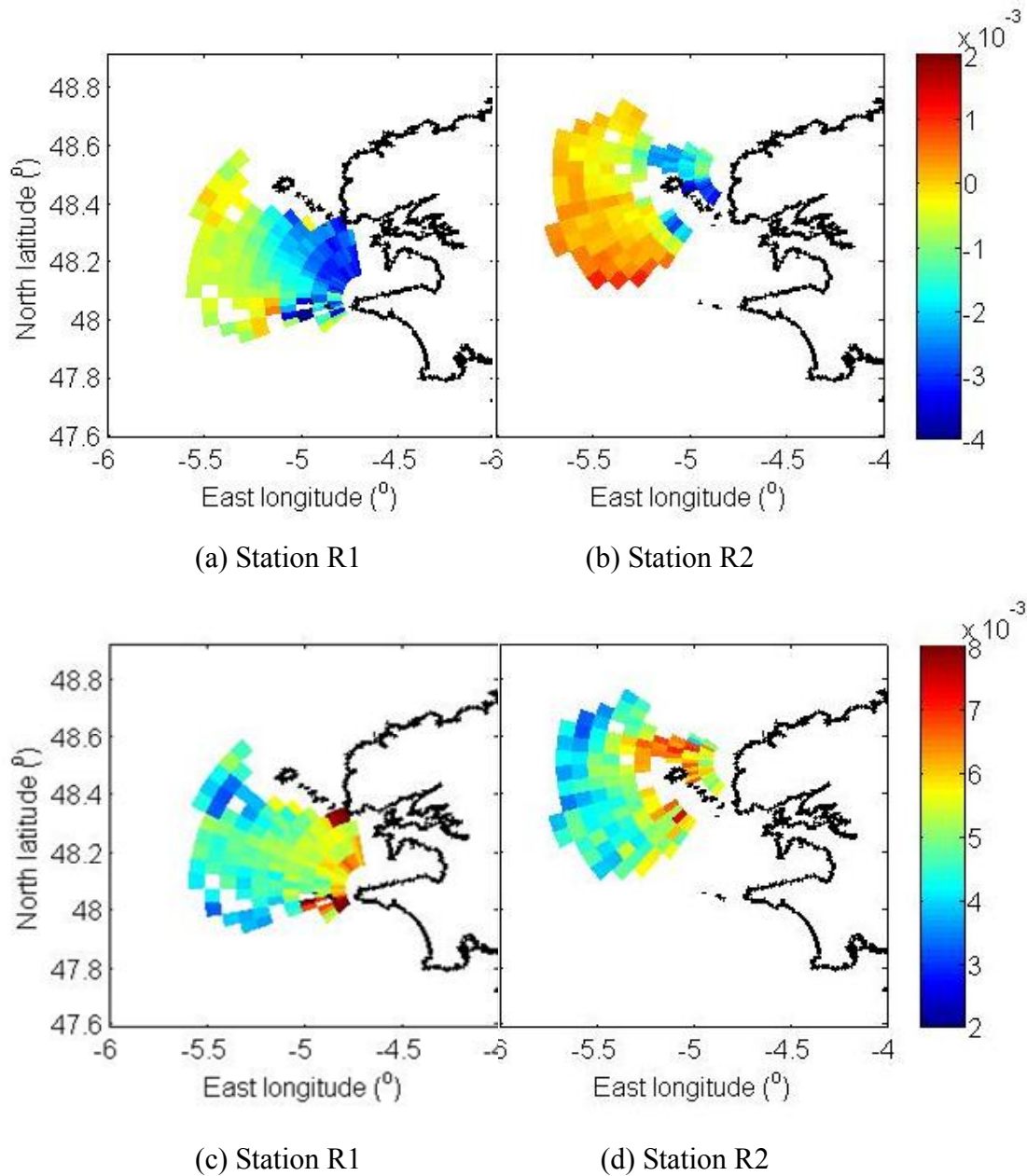


Fig. 6-10 Mean values (a, b) and stand deviations (c, d) of F_{sr} minus F_{sm} on radar cells. Colors denote values in unit of Hz.

Standard deviations of F_{sr} minus F_{sm} measured by the two stations are comparable indicated by Fig. 6-10 (c, d). The scatter between the two measurements shows similar characteristics for the near shore area and outer area. Near the islands and archipelagos both mean differences and STD of the differences vary much from other areas.

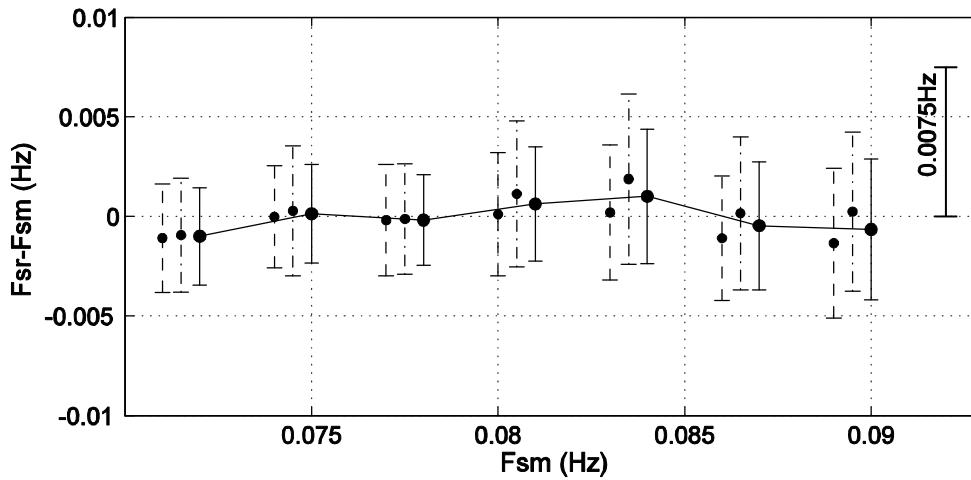


Fig. 6-11 Comparison of \bar{F}_{sr} and F_{sm} on common radar cells. Error bar indicates \pm STD of the differences between \bar{F}_{sr} (solid bar), F_{sr1} (dashed bar) and F_{sr2} (dot-dashed bar) in frequency intervals centered at the mean difference of radar and model estimates (dot). For a better visibility, dashed and dot-dashed error bars are slightly shifted to the left.

The consistency of swell frequency measurements from both radars (Section 6.1.1) suggests that using both measurements on common radar cells can improve the estimation of swell frequency. The mean values and standard deviations of F_{sr1} and F_{sr2} on common radar cells, \bar{F}_{sr} , are compared with model data in the intermediate frequency range 0.07-0.09 Hz, Fig. 6-11. The differences $\bar{F}_{sr} - F_{sm}$ are very close to zero. However, STD is only slightly reduced by the use of two radars. A slight larger STD in radar R2 than R1 is seen clearly here. We explain this difference by the much smaller number of observations from R2 due to more complicated topography (islands) in R2 spatial coverage. Making use of both radar sites reduces STD between radar

and model estimates to 0.004 Hz.

6.2 Swell directions

It is shown in Section 2.4.3 that there are two approaches to compute radar-inverted relative swell direction, q_{sr} . With measurements of normalized swell peak energy from single radar station, both POS and LS method were applied to invert relative swell direction, noted as q_{srp} and q_{srl} , respectively. On common radar cells, acquisitions of two measurements of relative swell direction enable the solution of absolute swell direction (q_{sa}).

6.2.1 Comparison between POS and LS methods

The overall comparison between q_{srp} and q_{srl} is shown in Fig. 6-12. Density shown in contours is defined as the number of samples counted in small grid squares, $5^\circ \times 5^\circ$, normalized by the number maximum. There are a percentage of 64% and 96% samples within contour 40% and 10%, respectively. Contours are approximately circles. The 64% of both results range from 120° to 160° and 96% results range from 110° to 170° . These directions indicate incoming swell towards radar stations. There is no significant correlation between the two measurements, with correlation coefficient of 0.17. The linear regression equation is $q_{srl} = -70^\circ + 1.47q_{srp}$. The majority of q_{srl} is smaller than q_{srp} . Mean difference between the two measurements is 3° and root-mean-square difference (RMSD) is 18° . Table 6-6 shows perpendicular regression analysis with a total number of samples of 127064. In fact, there are much more samples from POS-method. Radar measurements of normalized swell peak energy (r) are more easily to contaminated by noise and thus contain larger uncertainties than measurements of swell peak Doppler frequencies which are used to compute q_{srp} . The advantage of POS-method is its easy computation and a much larger number of samples, while results of from LS-method have much more failure cases.

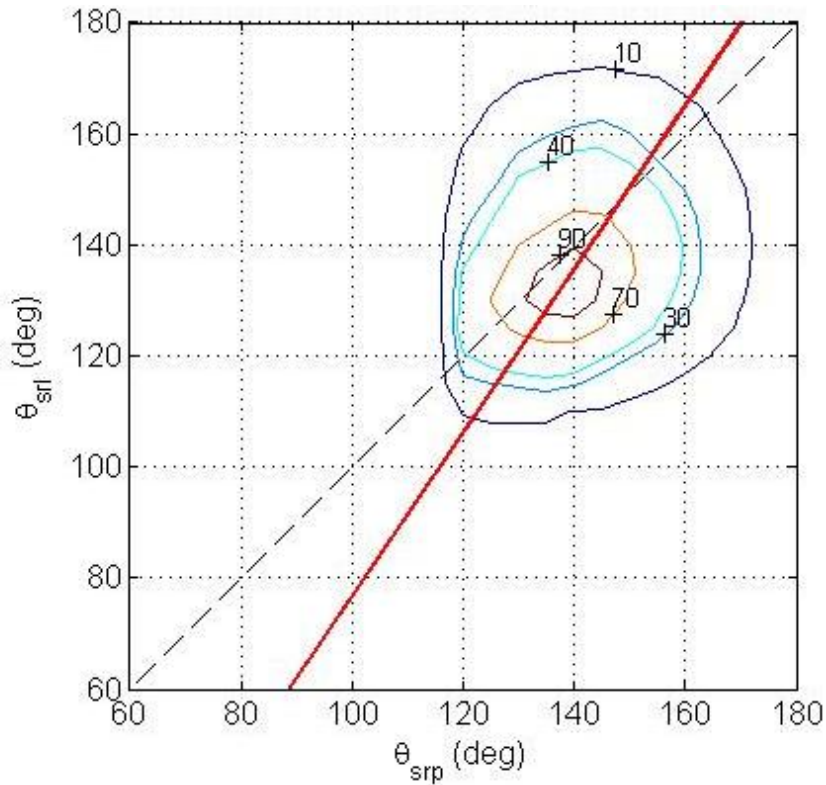


Fig. 6-12 Comparison between relative swell directions obtained from LS and POS method. Contours show relative sample density. Red line is the perpendicular regression line.

$a(^{\circ})$	b	R_e	RMSD($^{\circ}$)	STD($^{\circ}$)	n	p_1 (%)	p_2 (%)
-70	1.47	0.17	18	12	127064	43	75

Table 6-6 Perpendicular regression analysis between q_{srl} and q_{srp} during September 1 2007 – September 30 2008. Parameters are the same as in Table 6-1.

6.2.2 Comparison with model data

Radar measurements are compared with model-estimated relative swell direction, q_{sm} . Fig. 6-13 shows an example of a three-month time series of q_{srp} versus q_{sm} at radar cell R1 (23km, -15°). This radar cell lies within the region with the most qualified radar data for swell observation. The period considered spans from October 1 to December 31, 2007, which is the winter time with frequent swell events. Radar

measurements are very noisy and do not show evident feature of variations. The only coincidence of radar measurements and model estimates is that they both fall within interval of 120° - 180° . The mean difference between q_{srp} and q_{sm} for the whole 13-month period at this radar cell is 7.5° , and RMSD is 19° .

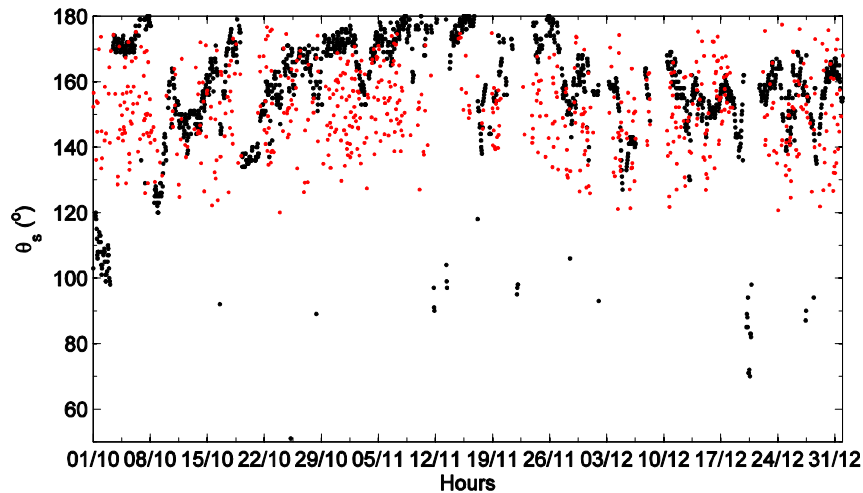


Fig. 6-13 Radar-derived relative swell direction q_{srp} (red dot) at radar cell R1 (23km, -15°) compared with model hind cast q_{sm} (black dot) during October 1 - December 31, 2007.

The overall comparisons of radar measurements by both methods and model estimates considering all radar cells of station R1 during the whole 13-month period are shown in Fig. 6-14, with results of linear regression analysis listed in Table 6-7. Neither method is correlated with model estimations, with correlation coefficient of 0.22 and 0.15. Mean values and STDs are computed in 10° intervals with number of samples over 5% of the maximum number in intervals. Mean values and STDs of both q_{srp} and q_{srl} are comparable. Mean values of q_{srp} are almost always slightly closer to model estimates. q_{srl} is less correlated with model estimates. We verify that mean values of q_{sr} vary less than q_{sm} for different radar beams. Model estimated absolute swell directions are more close to homogeneous in the coastal field, while radar measurements suggest potential swell directions with larger convergence approaching the coastline. However, results of q_{sr} are much scattered compared to q_{sm} for all radar cells.

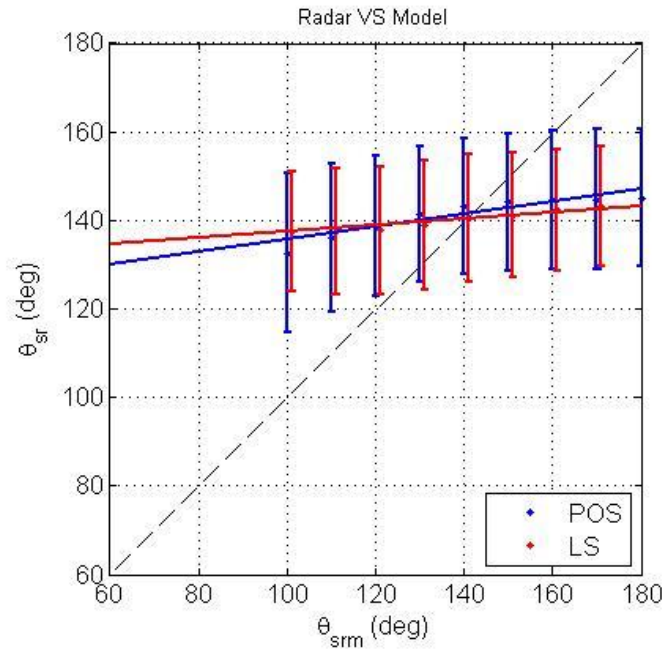


Fig. 6-14 Comparisons between radar (blue: POS method; red: LS method) and model estimated relative swell directions for all radar cells of station R1 during September 1 2007 - September 30 2008. Error bars and points denote \pm STD and mean value in each 10° interval.

	$a(^{\circ})$	b	R_e	RMSD($^{\circ}$)	STDL($^{\circ}$)	n	$p_1(\%)$	$p_2(\%)$
q_{srp}	121	0.14	0.22	27	16	189534	71	96
q_{srl}	130	0.07	0.15	27	14	139518	66	96

Table 6-7 Linear regression analysis of q_{srp} and q_{srl} with model estimations for all radar cells of station R1 during September 1 2007 - September 30 2008. Parameters are the same as in Table 6-1.

The differences between q_{srp} and q_{sm} during the 13-month period are studied from cell to cell, Fig. 6-15. Fig. 6-15 (a) shows that radar measurements from station R1 are larger (smaller) than model estimates in radar beams in the north (south). Fig. 6-15 (b) shows that radar measurements from station R2 are smaller (larger) than model estimates in radar beams in the north (south). They both illustrate that q_{srp}

varies more severely in different radar beams while q_{sm} varies much less. Stand deviations of q_{srp} minus q_{sm} measured by the two stations are both around 20°, Fig. 6-10 (c, d). The scatter near islands is relatively larger. So does the area farther off shore.

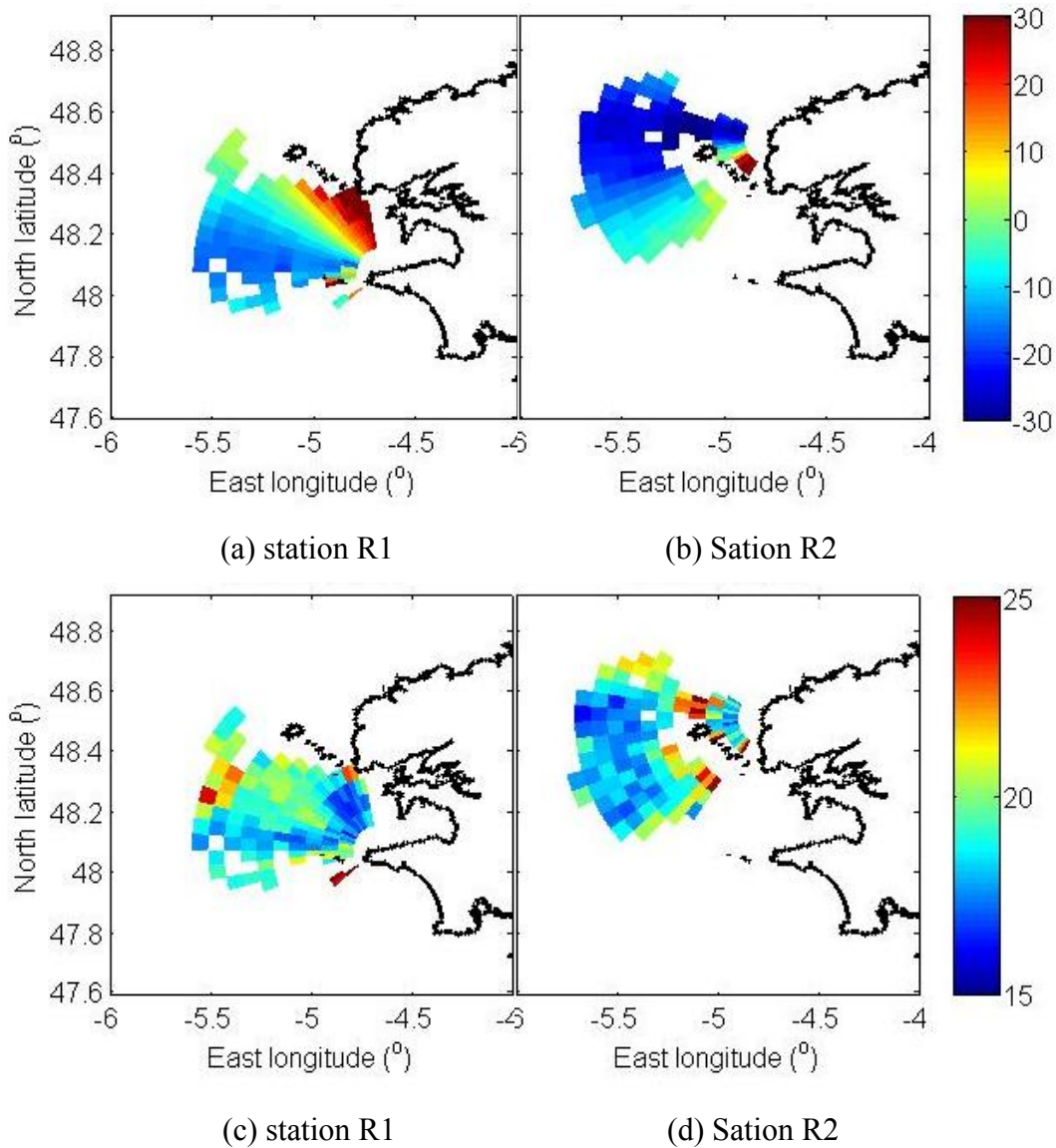


Fig. 6-15 Mean values (a, b) and stand deviations (c, d) of q_{srp} minus q_{sm} on radar cells with at least 200 samples. Colors denote values in unit of degree.

6.2.3 Absolute swell direction

The consistency between measurements from both radar stations (Section 6.1.1

and Section 6.3.1) offers an opportunity to employ both radar spectra to solve the ambiguity in relative swell direction at common radar cells. With doubled measurements of swell peaks (8 peaks), the LS method is applied in the same way to invert absolute swell direction, q_{sal} . Two relative swell directions with respect to different radar beams obtained from POS method gives four guesses of absolute swell directions. Two of them are supposed to be very close to the real swell direction. This offers another way to obtain absolute swell direction from POS method, q_{sap} .

Fig. 6-16 shows an example of q_{sal} and q_{sap} compared to model estimated absolute swell direction, q_{sam} . The period spans 5 days in the beginning of December 2007. The correlation coefficient between radar and model estimates for LS (POS) method is 0.601 (0.103); the regression slope is 0.791 (0.339); STDL is 12° (38°). These results suggest that LS method succeeds to obtain reasonable results of absolute swell direction with the combined use of both Doppler spectra, whereas POS method hardly benefits from the increase of radar spectra samples.

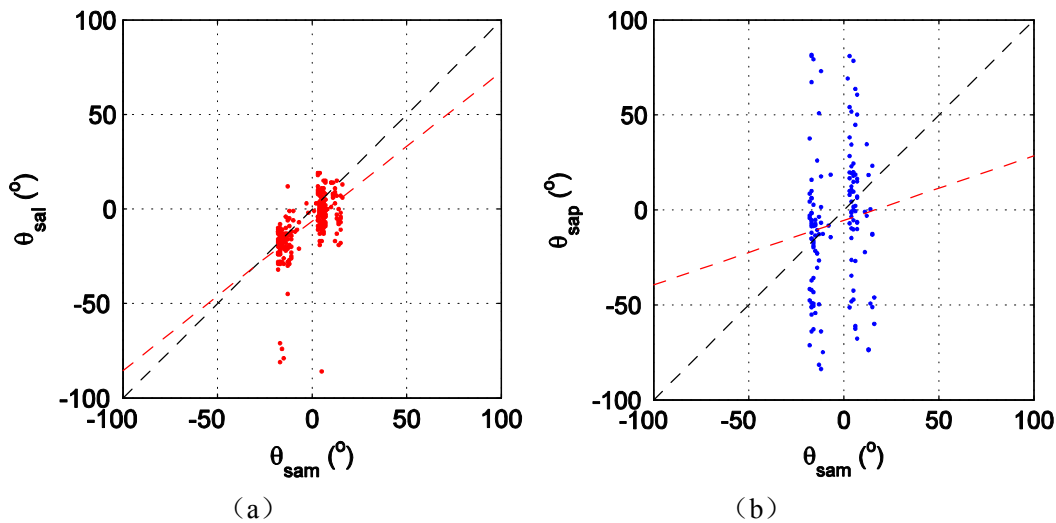


Fig. 6-16 Radar inverted absolute swell direction with comparison to model hind cast during December 1-5, 2007. (a) LS method. (b) POS method. Red dashed lines are the linear regression lines.

Statistics of q_{sam} during the whole 13-month period in six different locations in the Iroise Sea are shown in Fig. 6-17. For each location, values of q_{sam} and swell frequency are presented in the polar coordinate. It is observed that the propagation of

swell are mostly towards the absolute direction of -20° . The main variations of q_{sam} are within 50° . In near shore area, waves tend to turn directions perpendicular to the isobaths.

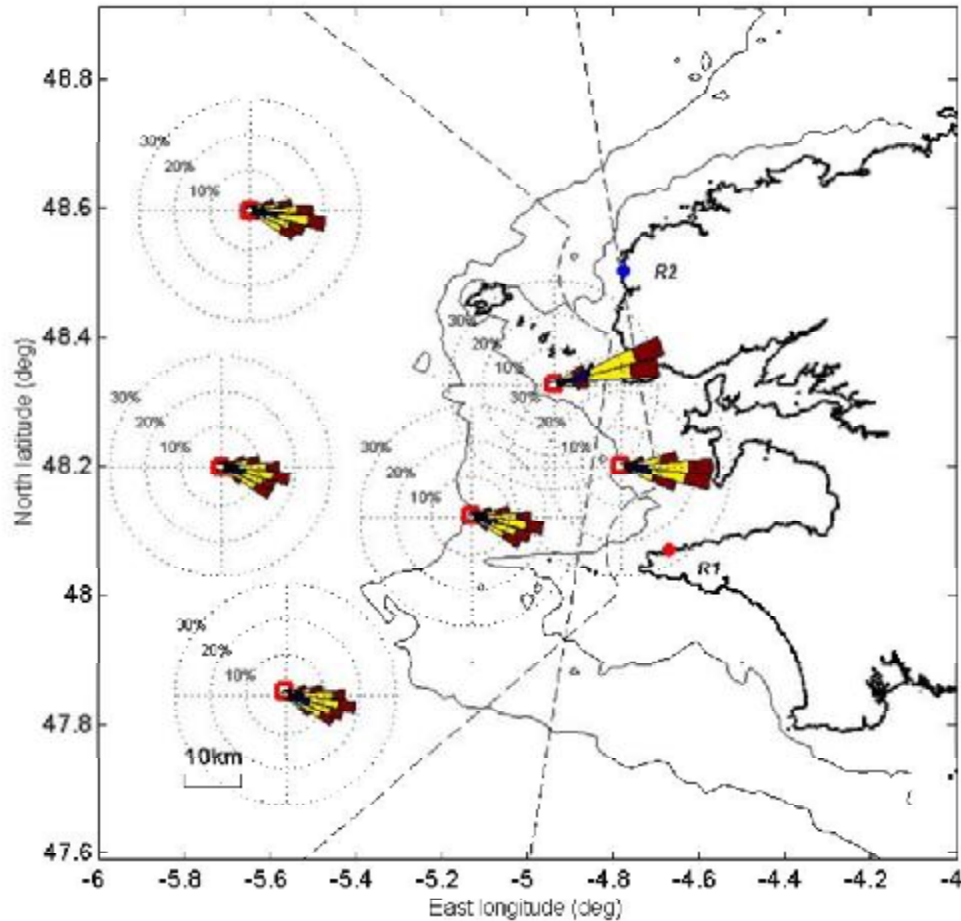


Fig. 6-17 Statistics of absolute swell direction estimated by WW3 during September 1 2007 - September 30 2008. The direction in the polar coordinate at each location is divided into 10° intervals. The radius circles show percentages of samples of 10%, 20% and 30%. Colors of dark blue, yellow and brown show proportion of samples in the interval with frequency of 0.045 - 0.08 Hz, 0.08 - 0.1 Hz, 0.1 - 0.126 Hz.

6.3 Swell significant waveheights

Radar-derived swell significant waveheight, H_{sr} , was obtained using values of

radar estimated swell frequency (F_{sr}), relative direction q_{sr} and measurements of r from the hourly averaged Doppler spectrum. As POS provides results with similar accuracy and much larger number of samples compared to LS method, q_{sr} takes values of q_{srp} in the computation (Eq. 2-54).

Also, the thesis proposes a constant relative swell direction, q_{sc} , to compute swell waveheight. It is shown in Section 4.1 that radar-inverted swell relative direction is very noisy, while the mean value does not vary much for different radar cells. For this reason, a constant mean value of q_{sr} can be employed in the computation of H_s . This proposal is supported by the analyses in Section 2.4.2 that computation of waveheight does not depend much on the accuracy of relative direction. WW3 estimations present that in radar beams of -25° to 60° of station R1, the relative swell direction are almost always larger than 130° with mean values larger than 140° . For these areas a variation of up to 20° in relative direction will bring less than 20% deviation of significant waveheight. For station R2, WW3 presents lots of cases with cross swell direction with respect to radar beams. These cases cause abnormal values in the coupling coefficient using methods described in Section 2.4.2. Thus a constant value of direction also helps to solve the singularity problem and gives a first guessed value of waveheight. Considering measurements of q_{srp} from all radar cells during the whole 13-month period, the value of q_{sc} is 140° . The output significant waveheight writes H_{sc} .

6.3.1 Comparison with buoy data

Buoy measured swell significant waveheight, H_{sb} , is used to validate radar inversions, Fig. 6-18 and Table 6-8. The two figures show samples lower than the radar measurement limitation of 4.6 m. The constant direction scheme (Fig. 6-18 b) significantly reduces the large scatter in the original scheme (Fig. 6-18 a). STDL decreases to 0.43 m from the original 0.65 m. The regression line of H_{sc} is slightly better than that of H_{sr} with comparisons to buoy data. Correlation coefficient of H_{sc} is much larger. There are less samples in the scheme of H_{sr} because of nulls in q_{srp} , while the scheme of H_{sc} is not affected by this problem. For this radar cell, the number of samples increases 20% in the scheme of H_{sc} than in the scheme of H_{sr} . If applied in all radar cells, this increase of number will be very large.

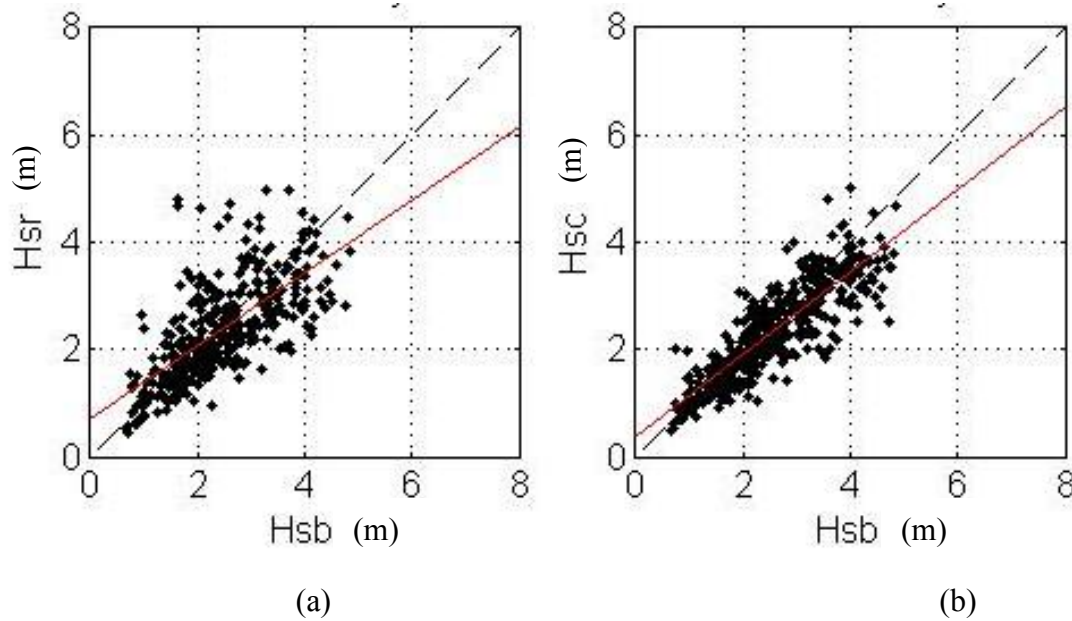


Fig. 6-18 Scatterplots of radar and buoy measurements of swell significant waveheight (unit: m) during February - July, 2008. Red line is the regression line. (a) Radar inversion scheme of H_{sr} . (b) Radar inversion scheme of H_{sc} .

	a (m)	b	R_e	RMSD(m)	STDL(m)	n	p_1 (%)	p_2 (%)
H_{sr}	0.68	0.68	0.70	0.72	0.65	377	75	96
H_{sc}	0.34	0.78	0.87	0.53	0.43	471	72	94

Table 6-8 Linear regression analysis of radar and buoy measurements of swell significant waveheight during February - July, 2008. Parameters are the same as in Table 6-1.

All the time series of the comparison of H_{sc} and H_{sb} is shown in Fig. 6-19. Radar measurements agree well with buoy measurements. For low to moderate swell cases (< 3 m), their differences are relatively small. For energetic swell cases, radar presents very few measurements and the measurements differ much from buoy measurements. The thesis verifies that the outliers often correspond to the severe distortions of Doppler spectra which hardly pass through the quality control described in Section 3.4. For these cases, the measurements of normalized swell peak energy

have large uncertainty.

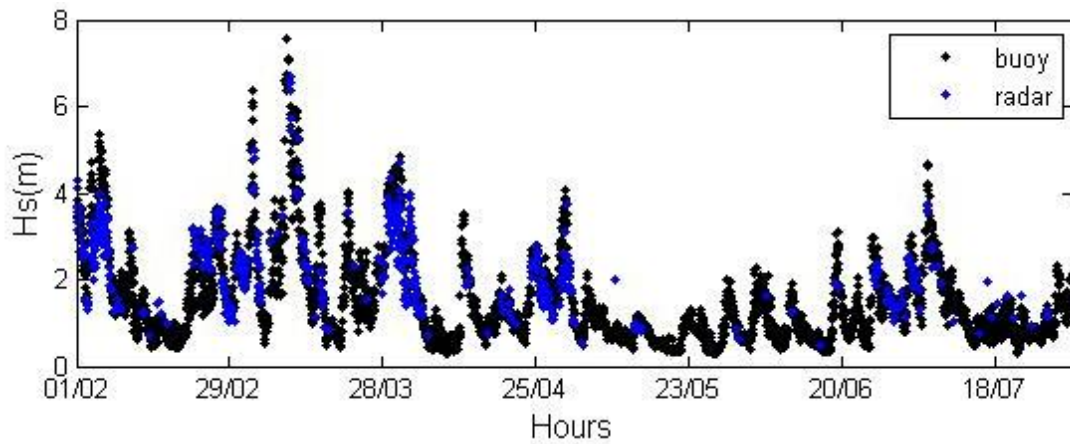


Fig. 6-19 Time series of radar and buoy measured swell significant waveheight during February - July 2008. Black dots: H_{sb} . Blue dots: H_{sc} .

6.3.2 Comparison with model data

Model (WW3) estimated swell significant waveheight, H_{sm} , is used to compare with radar measurements. Fig. 6-20 (a) shows examples of time series of H_{sr} at radar cell R1 (23 km, -15°) which is within the central area of efficient radar coverage. Fig. 6-20 (b, c) present values of F_{sr} and q_{sr} used in the computation of H_{sr} . Although values of q_{sr} are very noisy, the results of H_{sr} agrees reasonably well with H_{sm} . As F_{sr} agrees very well with F_{sm} , it is supposed that F_{sr} brings very limited amount of error to the computation of H_{sr} , except in the beginning of the period. It is observed that the increase of swell waveheight accompanies the decrease of frequency in each single swell event.

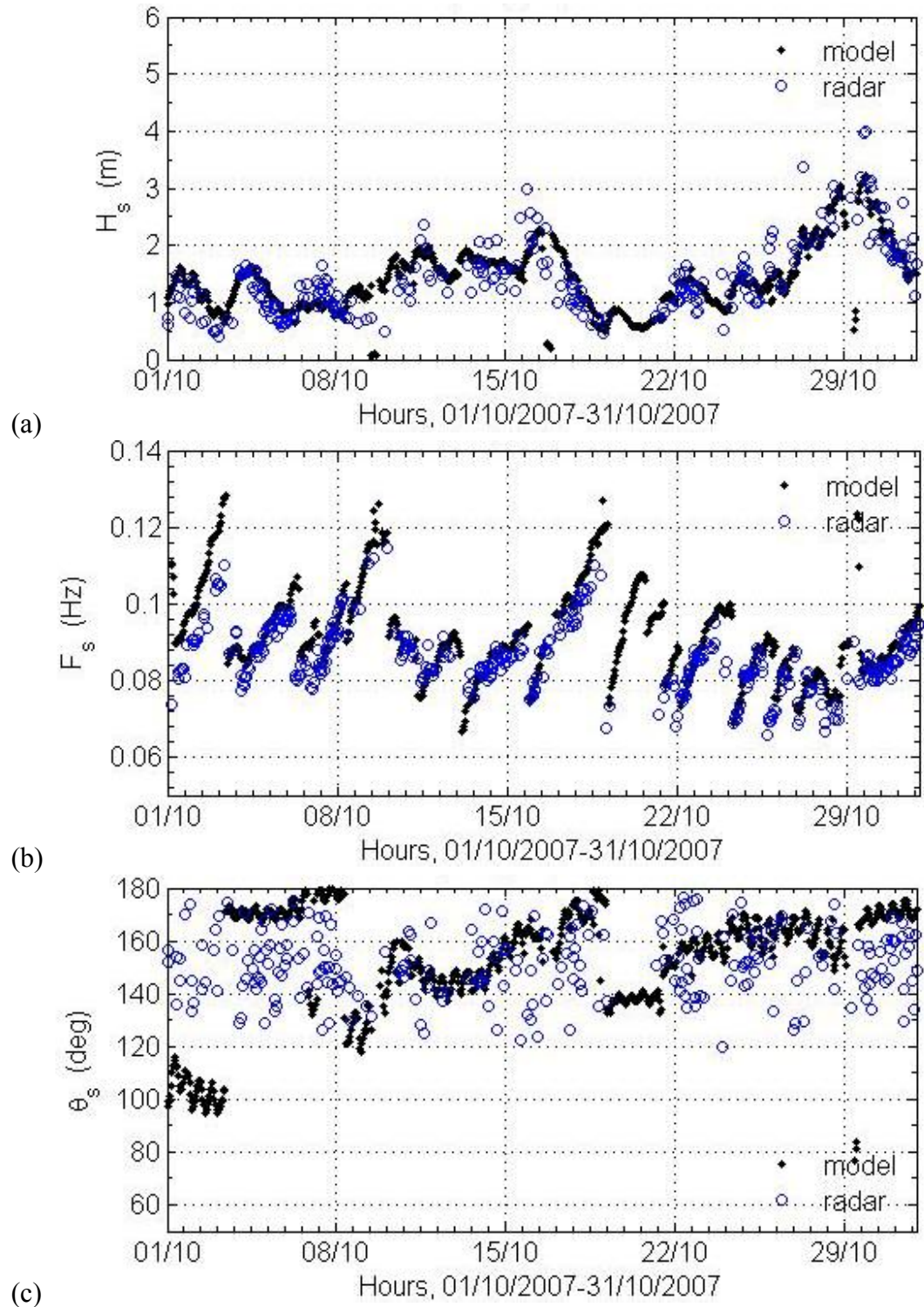


Fig. 6-20 Time series of H_{sr} (a), F_{sr} (b) and q_{sr} (c) during October 2007 at radar cell R1 (23 km, -15°). Black dots: model estimations. Blue circles: radar measurements.

Fig. 6-21 shows the performance of H_{sr} at the same radar cell and for the same

period as in Fig. 6-13. The difference between H_{sr} and H_{sm} is small for low to moderate swell (say < 3 m). Values of H_{sr} become more scattered, together with some outliers, for energetic swell. Despite the inaccuracy in q_{sr} , H_{sr} agrees generally well with H_{sm} concerning both temporal variation (Fig. 6-21 a) and statistical comparison (Fig. 6-21 b). This illustrates the theoretical analysis in Section 2.4.2. Fig. 6-21 (c) shows that HFR almost always measures swell during the whole period. Model estimations show the similar occurrence. In fall and winter, swell appear more frequently than in spring and summer. In particular, the swell energy significantly increase in winter.

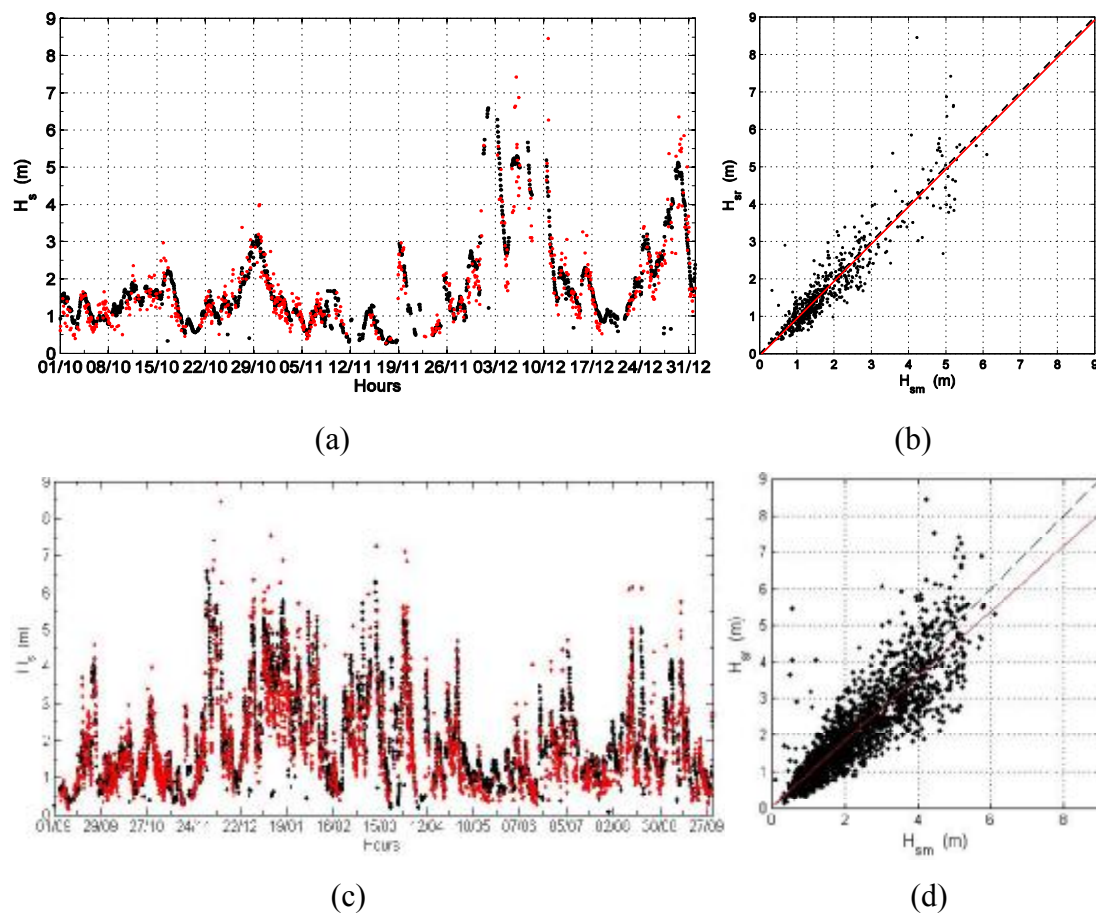


Fig. 6-21 Comparison of radar-derived significant waveheight H_{sr} (red dot) and model estimate H_{sm} (black dot) at the same radar cell as in Fig. 6-13. (a) and (c) show time series while (b) and (d) show scatterplots during October 1 - December 31, 2007, and the whole 13-month period, respectively. Red line is the linear regression line.

For comparison, model estimated q_{sm} is applied in the computation of swell significant waveheight. The output is denoted as H_{sw} . The comparisons between H_{sr} and H_{sw} with respect to H_{sm} at different locations are shown in the first six rows in Table 6-9. The three radar cells considered located every 20° in the same range crown of radar station R1. Comparisons in each series use the same number of samples according to the size of H_{sr} . Generally speaking, H_{sr} gives the regression slope more stable and closer to 1 than H_{sw} . However, the scatter of H_{sr} , characterized by STDL, is very large. The use of q_{sm} reduces 75% of the scatter of H_{sr} . This implies that the uncertainty of q_{sr} accounts for the most part of the scatter of H_{sr} . In addition to the advantage of smaller scattering, H_{sw} has also larger correlation coefficient than H_{sr} . However, there is obvious bias in H_{sw} induced by q_{sm} . There is a decrease of the regression slope in H_{sw} vs H_{sm} for these three locations. Mean swell relative directions from wave model (radar) estimates are 130° (142°), 154° (146°), 165° (145°) for the first three cells, separately. The smaller variation of q_{sr} is consistent with that observed in Section 6.2.2. Their regression analysis shows that in general H_{sw} overestimates (underestimates) H_{sm} when q_{sm} is small (large), whereas H_{sr} offers proper regression slopes for all. If we believe in wave model-derived H_{sm} and the Doppler spectrum model, this suggests an underestimation (overestimation) in q_{sm} when it is small (large) (Fig. 2-10). The difference between H_{sw} and H_{sm} may also come from the theory, in particular from an inadequacy of the coupling coefficient in some cases. This point probably needs further investigation.

Performances of the three inversion schemes, H_{sr} , H_{sw} and H_{sc} , on all radar cells during the whole 13-month period are quantified in the last three rows in Table 6-9. The comparisons concern all radar cells of both stations. The regression analysis shows that H_{sr} has the best regression slope and H_{sw} the worst. The schemes H_{sc} and H_{sw} have much smaller scatter than H_{sr} . Considering STDL and correlation coefficient listed in Table 1, H_{sc} offers the best way for swell waveheight estimation in general. Moreover, it also provides the largest number of results than the other two schemes which suffer from null q_s estimation from time to time.

Radar cell considered	Comparison with H_{sm}	a (m)	b	STDL(m)	R_e
-----------------------	--------------------------	---------	-----	---------	-------

R1(23km,-35°) N2=1676	H_{sr}	0.248	0.838	0.5838	0.762
	H_{sw}	0.021	1.179	0.4696	0.900
R1(23km,-15°) N1=2202	H_{sr}	0.217	0.792	0.6023	0.766
	H_{sw}	0.066	0.780	0.3006	0.920
R1(23km,5°) N3=1224	H_{sr}	0.168	0.859	0.6394	0.752
	H_{sw}	0.162	0.656	0.2912	0.886
All data from both stations N4=107790	H_{sr}	0.287	0.825	0.8384	0.699
	H_{sw}	0.201	0.764	0.5229	0.824
	H_{sc}	0.352	0.770	0.4287	0.873

Table 6-9 Comparisons of three inversion schemes (H_{sr} using radar inverted relative swell direction from POS-method, H_{sw} using model estimates of relative swell direction, H_{sc} using a constant relative swell direction 140°) with model estimate H_{sm} in the one-year period at different locations. N1~N4 are numbers of samples. Other parameters are the same as in Table 6-1.

Fig. 6-22 shows the statistical analysis of our method for swell waveheight inversion. To minimize the impact of the uncertainty of q_{sr} , the investigation compares H_{sw} and H_{sc} with H_{sm} . Mean values and standard deviations are computed in 0.2 m intervals plotted at the center of these intervals. The number of samples in each interval shown in the figure is greater than 500. Both schemes underestimate swell waveheight in most cases, except for low swell ($H_{sm} < 1$ m). H_{sc} provides closer estimations than H_{sw} for low to moderate swell ($H_{sm} < 4.5$ m). For the energetic swell, H_{sc} shows slightly larger bias than H_{sw} . The relative density is computed in a mesh gridded by 0.2 m. Fig. 6-22 (b) shows relative standard deviation of H_{sw} normalized by central interval values of H_{sm} . The relative standard deviation is less than 30% for $H_{sm} > 1$ m. It tends to a small constant of about 20% for $H_{sm} > 2$ m. The disadvantage of the scheme H_{sc} is that it shows obvious underestimation of waveheight for energetic swell, Fig. 6-22 (c).

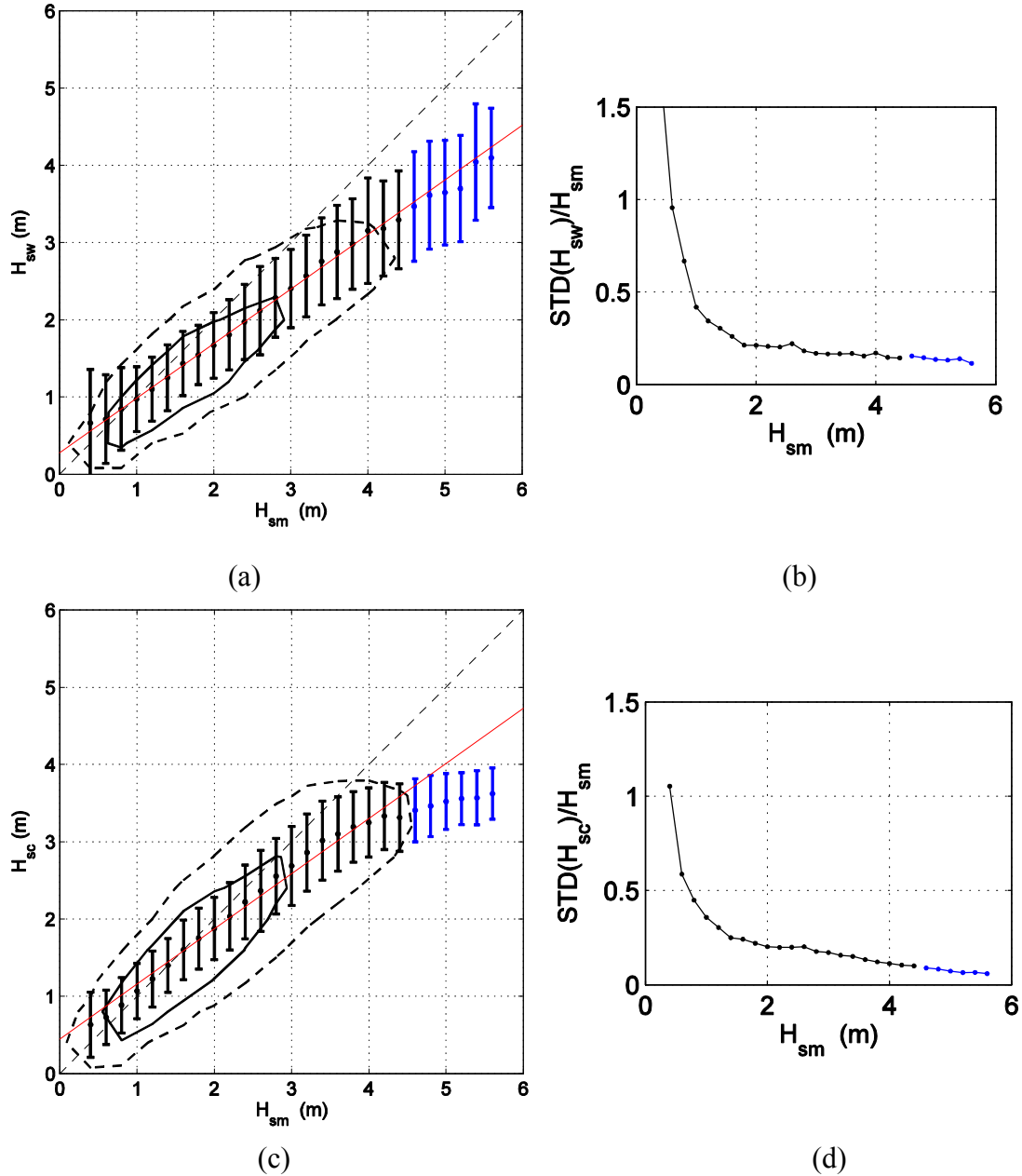


Fig. 6-22 Comparison of H_{sw} (a) and H_{sc} (c) with H_{sm} at all radar cells over the whole 13-month period. Dots are mean values of H_{sw} and H_{sc} in 0.2 m intervals of H_{sm} . Bars depict \pm STD with respect to the mean. Red line is the linear regression line. Dashed and solid contours indicate relative sample density of 10% and 40%, respectively. STD of H_{sw} and H_{sc} normalized by central value of H_{sm} in intervals is shown in (b) and (d), respectively. Statistics exceeding $H_{s,max} = 4.6$ m are noted in blue.

6.3.3 Consistency of both radar measurements

A comparison of H_{sw} during the 13-month period on common cells between the two radars, H_{sw1} and H_{sw2} for radar station R1 and R2, respectively, is shown in Fig. 6-23. The regression line (in red) is computed based on the perpendicular regression method which minimizes the root-mean-square perpendicular distance of samples from the regression line. Statistical parameters are listed in Table. We verify that the mean values of H_{sw1} and H_{sw2} agree well for every interval. Standard deviations for the two variables in each interval are indicated by bars centered on the equal line. The two measurements show similar scatter characteristics in individual intervals. Both give a majority of measurements of about 2.5 m.

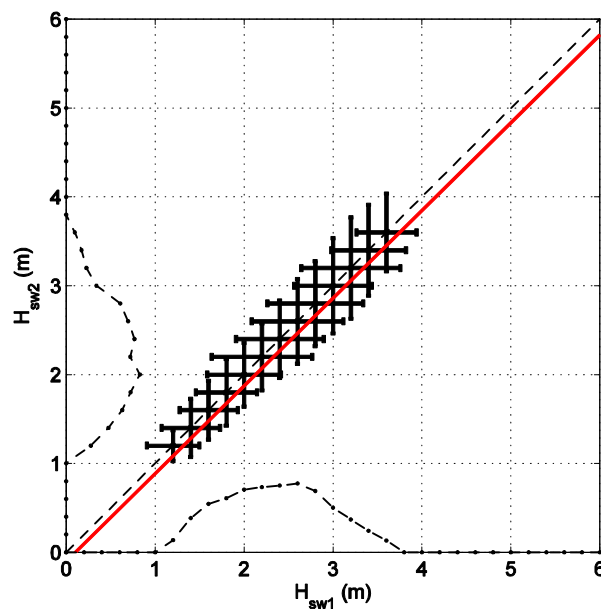


Fig. 6-23 Comparison of H_{sw1} and H_{sw2} at common radar cells. Horizontal (vertical) error bar depict \pm STD of H_{sw1} and (H_{sw2}) for samples in 0.2 m interval. Dashed diagonal line is of equal value. Red solid line shows the perpendicular regression line. Dashed curves indicate histograms of the two variables, respectively, counted in 0.2 m interval and divided by a factor of 500.

	a (m)	b	R_e	STDL(m)	n	p_1 (%)	p_2 (%)
--	---------	-----	-------	---------	---	-----------	-----------

H_{sw2} vs H_{sw1}	-0.102	0.987	0.733	0.2970	3182	54	86
------------------------	--------	-------	-------	--------	------	----	----

Table 6-10 Comparison of H_{sw1} and H_{sw2} on all the common radar cells between two radar stations in the whole period. Parameters are the same as in Table 6-1.

6.4 Summary

This section shows the inverted results of swell frequency, direction and significant waveheight. These results are validated by buoy and WW3 estimates. Comparisons show that radar-inverted swell frequency and waveheight are reasonably in good accuracy while radar-inverted swell direction has much uncertainty.

There two methods, POS and LS, for the inversion of relative direction show similar accuracy for single radar station. But accuracy of LS method greatly increases when using both radar spectra on common cells. However, POS method provides very efficient computation and much larger number of samples as it is less disturbed by the quality of spectra.

The inversion technique of significant waveheight works for swell with relative direction well beyond the singularity region. Using radar-derived direction gives a rough estimation of waveheight, but with very large scatter. This noisy feature was illustrated to be related with the uncertainty of radar-derived direction. A constant relative swell direction method is proposed in the computation of swell waveheight. This method is demonstrated to improve the inversion of swell waveheight. Although there is certainly bias when appoint a constant direction, this scheme might do some help when we lack data of swell direction. It could also be useful for radar cells where cross swell events frequently encountered.

These results demonstrate the consistency of both single radar measurements. The two radars can be used in a complementary way in case of failure of one of them or, more generally, for the improvement of the estimations of swell parameters. The combined use of both radar measurements solves the ambiguity in the relative swell direction.

7 Accuracy analysis

The thesis employs estimations of buoy and WW3 wave model to validate the accuracy of radar inversion of swell parameters. The differences between radar measurements and buoy or model estimates can be explained by three main causes: radar measurement uncertainty, methodological discrepancies and buoy / model estimate uncertainty.

The total uncertainty of radar-inverted swell frequency validated by buoy measurement is evaluated by STDL of 0.0041 Hz (Table 6-4). The total uncertainty validated by model estimation is evaluated by STDL of 0.0052 Hz (Table 6-5).

For relative swell direction, the total uncertainty validated by model estimation is evaluated by STDL of 16° (Table 6-7).

The total uncertainty of radar-inverted swell waveheight validated by buoy measurement is evaluated by STDL scheme H_{sc} , 0.43 m (Table 6-8), excluding the large scatter induced by of relative direction. The total uncertainty validated by model estimation is evaluated by STDL of scheme H_{sw} , 0.52 m (Table 6-9).

7.1 Radar intrinsic errors

Errors of radar measurements of swell parameters come from errors of the measurements of swell peak Doppler frequencies and amplitudes. There are contributions from randomness, occasional environmental pollution and failure of the swell identification method. Random errors are greatly reduced by the averaging processing described in Section 3.3. Environmental noise, such as RFIs (radio-frequency interferences), and undesired echoes, such as ship echoes, can generate disturbing spectral signatures which contaminate the values of Doppler frequencies and spectral amplitudes of swell peaks. Thus they decrease the accuracy of raw measurements, especially at far distances where radar signals are weak. Although the discrimination criteria of quality control described in Section 3.4 reject most of these cases, residual failures still exist. In addition, the identification program for swell peaks in a Doppler spectrum has subjective criteria which may contribute to the inaccuracy of inverted parameters.

Considering the comparison of both radar measurements on common cells, the radar intrinsic uncertainty of swell frequency, is characterized by STDL of 0.0035 Hz (Table 6-1); the radar intrinsic uncertainty of swell significant waveheight is evaluated

by STDL of scheme H_{sw} , 0.30 m (Table 6-10). As single station gives relative swell direction which is not comparable between different radar beams, there is no evaluation of intrinsic error of q_{sr} .

7.1.1 Random error in radar-inverted frequency

The ocean surface height is customarily considered as a random variable and can be described by sum of Fourier series. The central limit theorem states that the sum of random variables follows Gaussian distribution. Barrick and Snider (1977) explained that backscattered sea echo signals from the ocean surface can be well represented by a Gaussian distribution. Thus the power of each spectral sampling point in the Doppler spectrum obeys the c^2 distribution with two degrees of freedom. Section 3.3 showed that a total number of 48 independent samples were averaged to produce hourly spectra. This greatly reduces the fluctuation of sampling points due to randomness, Fig. 7-1. Random error has been greatly reduced by the averaging processing of Doppler spectra.

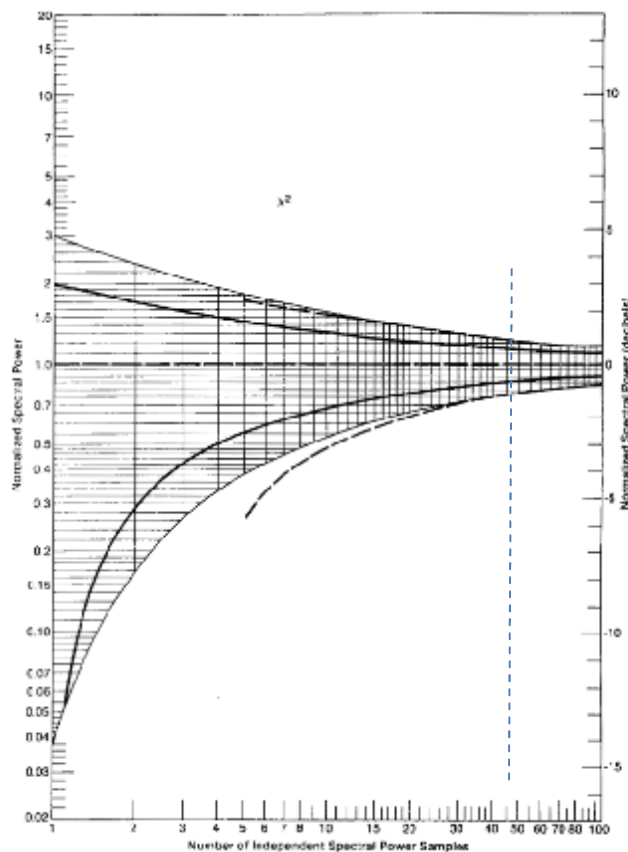


Fig. 7-1 Fluctuation statistics of the c^2 distribution as function of number of independent spectral power samples (from Barrick 1980). Horizontal dashed line is the mean of normalized spectral power. Two inner heavy solid lines are \pm STD from the mean. Upper (lower) outer line shows the 95% (5%) confidence limit.

According to Barrick (1980), the accuracy of Doppler frequency estimate of a peak (f_j) with a Gaussian shape can be quantified by an RMS error given by

$$\text{RMSE}(f_j) = 0.5 \sqrt{\frac{N_h}{K}} df \quad (7-1)$$

where K is the number of averaged independent spectra and N_h is the equivalent number of samples within half-power width of the spectral peak. If the shape of a spectral peak has a rectangular shape, the RMS error is expressed by

$$\text{RMSE}(f_j) = 0.58 \sqrt{\frac{N_h}{K}} df \quad (7-2)$$

The difference between Gaussian and rectangular models is small. This supports the feasibility of doing Gaussian fitting on spectral peaks in the statistical work in Section 3.4.

As the averaging is done over samples having unequal means, N_h is modified by a factor m

$$N_h = mN_{1/2} \quad (7-3)$$

with $N_{1/2}$ the number of samples within half-power width. This thesis uses $N_{1/2} \approx 5$ (Section 3.4). The factor m varies for different shape models. A fast estimation suggested by Barrick (1980) is $m \approx 1.3$. With $K = N_{sum} = 48$ (Section 3.2) and $N_{1/2} = 5$ (Section 3.3), Eq. (7-1) and Eq. (2-48) give

$$\text{RMSE}(F_s) = 0.0013 \text{ Hz} \quad (7-4)$$

This represents 29% (32%) of RMSD (STDL) of radar and buoy measurements of swell frequency of 0.0045 Hz (0.0041 Hz); 23% (25%) of RMSD (STDL) of radar and model estimates of swell frequency of 0.0056 Hz (0.0052 Hz).

7.1.2 Random error in radar-inverted relative direction

The calculation of relative swell frequency is mainly performed by POS method

which uses the Doppler frequencies of swell peaks. According to error propagation law, Eq. (2-49) and Eq. (7-4) give a theoretical estimation of the RMS error of $\cos q_s$ of equal to 0.146. This value corresponds to a broad interval of q_s . For example, q_s varies over 44° assuming a real swell relative direction of 180° . For a true swell relative direction of 140° , which is the value applied in the constant direction scheme of waveheight inversion, the variation of q_s is $134^\circ - 147^\circ$, 13° in total. This value accounts for 48% of the total RMSD and 81% of STDL between q_{sr} and q_{sm} (Table 6-7). This large uncertainty contributes to the inaccuracy of the inversion of swell waveheight.

7.1.3 Random error in radar-inverted waveheight

According to Barrick (1980), the RMS error of radar-inverted swell RMS waveheight induced by random error writes

$$\text{RMSE}(h_s) = p\sqrt{1/KM + 1/KN} \quad (7-5)$$

with p the power of normalized swell peak energy in the equation of waveheight computation; $M(N)$ the number of spectral points considered for swell (Bragg) peak computation. Here, $p = 1/2$ (Eq. 2-53), and M and N are both 5. The left term of Eq. (12) is 0.046, giving an RMS error of radar inverted significant swell waveheight equal to 0.184 m. This contributes to 26% (28%) of RMSD (STDL) of radar (scheme of H_{sr} using radar-inverted swell direction) and buoy measurements of swell significant waveheight of 0.72 m (0.65 m); 22% of STDL of radar and model estimates of swell significant waveheight of 0.84 m.

7.2 Methodological discrepancies

The second possible source of error comes from the different methods of swell measurements between radar and buoy/model. Radar measures swell from averaged sea echo over a large area. Buoy measures swell at fixed location. WW3 estimates swell by combinations of boundary conditions and forcing. The inversion model used in this thesis for the inversion of swell parameters is not perfect. The expression of the coupling coefficient is not well validated for different sea states. Moreover, the surface conditions, like currents, wind etc., affect radar and buoy in different ways. At high sea states, wind wave and swell frequencies can be close to each other. We verified that comparison results were similar in low to moderate wind conditions for

which swell identification is unambiguous. Indeed, in such conditions, our swell frequency interval is well separated from the peak frequency of the wind wave spectrum, F_{WP} . For example, the Pierson-Moskowitz (PM) wave spectrum model gives $F_{WP} > 0.137$ Hz for wind velocity lower than 10 ms^{-1} , i.e. F_{WP} is well larger than the upper limit (0.126 Hz) of swell frequency. However, in the Doppler frequencies, their difference is only 1.5 times of frequency resolution.

7.3 Buoy and model intrinsic errors

The third source of error comes from buoy or model itself. Buoy measurements are affected by random error and occasional environmental interruptions. It is also suspected that model estimations experience randomness, possible inaccurate program of forcing etc. However, it is difficult to discriminate the contributions of the last two sources (Section 7.2 and 7.3) to the differences between radar and buoy or model measurements of swell parameters. As an empirical alternative, they are evaluated by the total uncertainty minus radar intrinsic uncertainty.

For swell frequency, radar intrinsic uncertainty, 0.0035 Hz, represents 85% (67%) of the total uncertainty of radar-buoy (model) comparison, 0.0041 Hz (0.0052 Hz). It is then suggested that the other factors, second and third source, contribute to 12% (31%) of the total difference between radar and buoy (model) estimations.

For swell significant waveheight, radar intrinsic uncertainty represents 70% (58%) of the total uncertainty of radar-buoy (model) comparison. The other factors, second and third source, contribute to 30% (42%) of the total difference between radar and buoy (model) estimations.

7.4 Summary

The accuracy of radar-inverted swell parameters is evaluated using statistics of comparisons to buoy and model estimations. Random error of radar instrument is studied by assuming Gaussian distribution of the sea echo. The accuracy of radar-inverted swell frequency and significant waveheight is relatively good while the accuracy of relative swell direction is low.

Results suggest that radar measurement error is the dominant source of the difference between radar and buoy/model estimates. Other sources of errors can be the differences between methods by different devices and errors of buoy or model. Instead, contributions of these sources are evaluated by comparing radar intrinsic

uncertainty and the total uncertainty of differences between radar and buoy or model estimations.

Both experimental results and theoretical analysis show that radar-inverted relative swell direction has quite low accuracy. The representative quantity of theoretical uncertainty, 13° , is 48% (81%) of RMSD (STD) of radar and model estimates of relative swell direction of 27° (16°).

For swell frequency, radar intrinsic uncertainty represents 88% (69%) of the total uncertainty of radar-buoy (model) comparison. The other factors, second and third source, contribute to 12% (31%) of the total difference between radar and buoy (model) estimations.

For swell significant waveheight, radar intrinsic uncertainty represents 70% (58%) of the total uncertainty of radar-buoy (model) comparison. The other factors, second and third source, contribute to 30% (42%) of the total difference between radar and buoy (model) estimations.

8 Conclusions and perspectives

8.1 Main conclusions

The thesis uses a period of 13 months, September 1, 2007 - September 30, 2008, of HF radar echo data to invert ocean surface information. A series of data processing and quality control methods are proposed based on the theoretical analysis and statistical studies of radar data. Noise level is determined according to the circumstances of each specific radar spectrum. Taking into account the characteristics of relatively small variation in time, Doppler spectra are averaged during one hour for the computation of swell. An hourly spectrum comes from 48 independent Doppler spectra, with degree of freedom of 96. An automatic computing program with low consumption of computation resources is employed to give radar-inverted sea surface currents, wind directions and swell parameters. Statistics of qualified spectra for both stations show that station R1 presents better data while station R2 suffers much from shadowing of islands.

Radial velocity of surface current is obtained from measuring Doppler shift of Bragg peaks. Combination of radial velocities from two radar stations gives surface flow vectors. The one year mean (September 2007 - August 2008) flow field in the Iroise Sea is presented, together with its vorticity and divergence. Currents show more complex features near coast due to influences of islands and topography and larger velocity (20 cm/s). Off coast, the mean flow moves westward with small velocity (5 cm/s).

Bragg peaks ratio corresponds to relative wind direction with respect to radar look direction. Empirical methods are employed to obtain relative wind direction. Results agree with model hind cast. Harlan and Georges (1974) method works better than Long and Trizna (1973) method for our dataset. The dataset gives values of spreading parameters for different directional distributions. A mean value of the spreading factor using cardioid model of Cochin et al. (2005) is 3.92 for the Iroise Sea; a mean value of the spreading factor using hyperbolic secant squared model of Donelan et al. (1985) is 1.14.

Measurement of swell parameters uses nonlinear relationship between ocean waves and radar Doppler spectra. The method requires identifying four swell peaks. Doppler frequencies and amplitudes of these spectral peaks are used to compute swell

frequency, relative direction and significant waveheight. Radar-inverted swell frequencies agree very well with buoy and model estimations. Radar-derived relative swell directions from either POS or LS method show low accuracy compared to model hind cast. However, it is predicted theoretically and illustrated experimentally that the inversion of swell waveheight is not much dependent on value of relative direction. Radar-inverted swell significant waveheights agree reasonably well with buoy and model estimations. A constant relative direction method is proposed in the computation of waveheight. This method reduces the scatter and improves the global agreement with model and buoy estimated significant waveheight. It can be applied to provide a rough estimation of waveheight when cross swell frequently encountered as the present radar theory fails to compute such cases.

Radar-inverted swell parameters are validated by buoy and WAVEWATCH III model estimations. Comparisons between radar and buoy measurements of swell frequency give correlation coefficient of 0.92 and RMS difference of 0.0045 Hz. Comparisons between radar and model estimations of swell frequency give correlation coefficient of 0.90 and RMS difference of 0.0056 Hz. Both POS and LS methods obtain relative swell direction with low correlation coefficient compared to model estimations, with RMS difference of 27°. Comparisons between radar and buoy measurements of swell significant waveheight give RMS difference of 0.53 m. Radar measured swell significant waveheights are generally smaller than model estimations with STD from the linear regression line of 0.43 m.

Factors contributing to the differences between radar measurements of swell parameters and buoy and model estimations are investigated. Uncertainties in radar measurements due to randomness are quantified. This contributes not much in the differences between radar and buoy or radar and model estimated swell frequency and significant waveheight. It accounts much for the large scatter of radar-inverted relative swell direction. Results suggest that radar measurement error is the dominant source of the difference between radar and buoy/model estimates. Other sources of errors can be the differences due to different devices and errors of buoy or model.

8.2 Inadequate points and future work

Efforts presented in this thesis are useful for operational near real time monitoring of the ocean surface. Yet, accuracy of radar-inverted parameters can be further improved. More rigorous quality control considering impacts of islands and

topography can help reduce scatter. Besides, higher order interactions between ocean waves and electromagnetic waves are not considered in this thesis. The requirement of four swell peaks is very strict. Some information could be inverted with less number of peaks. Besides, the thesis assumes one single swell on the ocean surface, whereas neighbouring swell peaks have been observed in a single searching interval in some Doppler spectra, implying a multipul swell system. In addition, the variation of the Doppler spectra caused by strong currents could be analyzed. These envisaged improvements can be added into the computation program accordingly.

The thesis does not obtain results of relative swell direction in good accuracy. This can be further investigated from two perspectives. One is to increase resolution of Dopler frequencies by keeping longer time series in the data processing program. However, this will decrease the degree of freedom of spectral points, result in more spectral peaks, and bring in difficulties to swell identification. The other way is to investigate the modification of coupling coefficient in Barrick's integration equation. This thesis applies a constant effective value proposed by previous research. However, the value of coupling coefficient can be changeable for different sea states. The value could be determined by an empirical approach.

The potential utilization of radar inverted swell parameters could be envisaged for data assimilation in wave models. Similar work has already been attempted for radar derived surface currents in coastal circulation models (e.g., Breivik and Sætra 2001; Paduan and Shulman 2004; Marmain et al. 2014). However, there are only a few studies concerned assimilation of HF radar data into wave models. Siddons et al. (2009) showed that assimilation of HF radar inverted wave data into the SWAN model improves model results. The work on data assimilation can contribute to improvement of model forecasts and modifications of model parameters.

The work on second-order spectra focuses on the measurements of swell in this thesis. This large dataset can be very useful for the study of wind waves. Radar measurements also contribute to better knowledge of the fine scale evolution of swell and its interactions with other oceanic processes (Section 1.4). Applications of HFRs are being expanded in China which offers more datasets to investigate the inversion methods. Although the application for surface currents is well developed, there are not yet much work on wind and swell using these datasets. In this thesis, a constant relative swell direction method is proposed for the computation of swell waveheight. However, the ocean circumstances in the east of the ocean and in the west of the

ocean are very different. Historical dataset shows that there are much less frequent and less energetic swell cases in the ocean off Qingdao (Zhang et al. 2011). The application of our method in other locations needs more validation.

These are all expected in the future work.

Appendix A

The coupling coefficient Γ in the expression of the second-order sea echo is obtained from a perturbational solution of the nonlinear boundary conditions at the ocean surface, and is the sum of electromagnetic and hydrodynamic components, Γ_{EM} and Γ_H , respectively (E.g. Barrick 1977; Lipa and Barrick 1986). The expression of Γ is given by

$$\Gamma = \Gamma_{EM} - i\Gamma_H \quad (\text{A-1})$$

with i the imaginary number $\sqrt{-1}$.

The hydrodynamic component in deep-water is (Barrick 1972a; Weber and Barrick 1977)

$$\Gamma_H = \frac{1}{2}[K_1 + K_2 - \frac{(K_1 K_2 - \overset{\text{p}}{K}_1 \times \overset{\text{p}}{K}_2)(w^2 - w_B^2)}{m_1 m_2 \sqrt{K_1 K_2} (w^2 - w_B^2)}] \quad (\text{A-2})$$

with w the angular Doppler frequency.

For grazing incidence, the second-order simplified backscattered polarized electromagnetic waves under perturbation theory, i.e. the electromagnetic component, is

$$\Gamma_{EM} = \frac{1}{2} \frac{(\overset{\text{p}}{K}_1 \times \overset{\text{p}}{k}_0)(\overset{\text{p}}{K}_2 \times \overset{\text{p}}{k}_0) / k_0^2 - 2\overset{\text{p}}{K}_1 \times \overset{\text{p}}{K}_2}{\sqrt{\overset{\text{p}}{K}_1 \times \overset{\text{p}}{K}_2} - k_0 \Delta} \quad (\text{A-3})$$

with Δ the impedance of the sea surface. Barrick (1970) proposed an effective value of $\bar{\Delta} = 0.011 - 0.012i$ for a rough sea surface.

In shallow water condition, the electromagnetic component remains the same form, while the hydrodynamic component depends on water depth through

$$\Gamma_{HS} = \frac{1}{2} \left\{ K_1' + K_2' - \frac{(K_1' K_2' - \overset{\text{h}}{K}_1 \times \overset{\text{h}}{K}_2)(w^2 + w_B^2)}{m_1 m_2 \sqrt{K_1' K_2'} (w^2 - w_B^2)} + \frac{w[(m_1 \sqrt{gK_1'})^3 \csc h^2(K_1 d) + (m_2 \sqrt{gK_2'})^3 \csc h^2(K_2 d)]}{g(w^2 - w_B^2)} \right\} \quad (\text{A-4})$$

with d the water depth. K_1' and K_2' are the modified wave numbers

$$K_1' = K_1 \tanh(K_1 d) \quad (\text{A-5})$$

$$K_2' = K_2 \tanh(K_2 d) \quad (\text{A-6})$$

For water depth over 50 m, the shallow water effect is negligible, Fig. A-1.

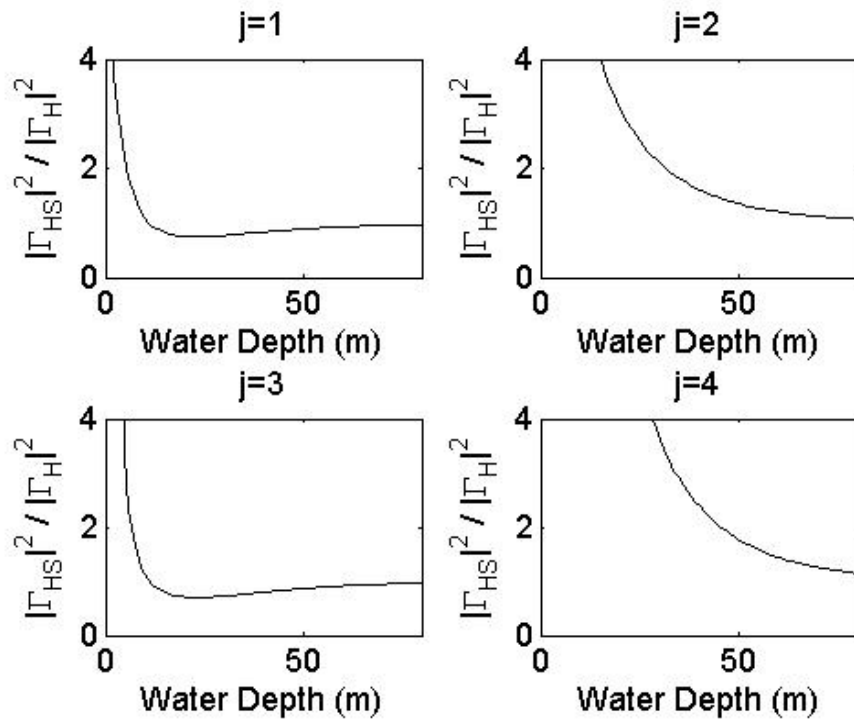


Fig. A-1 Normalized squared shallow water hydrodynamic coupling coefficient, $|\Gamma_{HS}|^2 / |\Gamma_H|^2$, as a function of water depth, under the assumption of single swell moving towards radar station with frequency 0.08 Hz.

References

- Ardhuin F, O'Reilly W C, Herbers T H C, Jessen P F (2003) Swell transformation across the continental shelf. Part I: Attenuation and directional broadening. *J Phys Oceanogr* 33: 1921-1939. DOI: doi: [http://dx.doi.org/10.1175/1520-0485\(2003\)033<1921:STATCS>2.0.CO;2](http://dx.doi.org/10.1175/1520-0485(2003)033<1921:STATCS>2.0.CO;2)
- Ardhuin F, Marié L, Rasclé N, Forget P, Roland A (2009a) Observation and estimation of Lagrangian, Stokes, and Eulerian currents induced by wind and waves at the sea surface. *J Phys Oceanogr* 39: 2820-2838
- Ardhuin F, Chapron b, Collard F (2009b) Observation of swell dissipation across oceans. *Geophys Res Lett* 36 (L06607). DOI: 10.1029/2008GL037030
- Ardhuin F, Rogers E, Babanin AV et al. (2010) Semi-empirical dissipation source functions for wind-wave models: Part I, definition, calibration and validation. *J Phys Oceanogr* 40 : 1917 - 1941
- Barrick D E (1971) Theory of HF/VHF propagation across the rough sea - Parts I and II. *Radio Sci* 6: 517-533
- Barrick D E (1972a) First-order theory and analysis of MF/HF/VHF scatter from the sea. *IEEE Trans Antennas Propag* 20 (1): 2 - 10. DOI: 10.1109/TAP.1972.1140123
- Barrick DE (1972b) Remote sensing of sea state by radar. *Remote Sensing of the Troposphere*, edited by V. E. Derr, chap. 12, US Government Printing Office, Washington DC.
- Barrick D E, Evans M W, Weber B L (1977a) Ocean surface currents mapped by radar. *Science*. 198: 138-144. DOI: 10.1126/science.198.4313.138
- Barrick, D E (1977a) The ocean waveheight nondirectional spectrum from inversion of the HF sea-echo Doppler spectrum. *Remote Sensing Environ.* 6: 201 - 227
- Barrick D E (1977b) Extraction of wave parameters from measured HF radar sea-echo Doppler spectra. *Radio Sci* 12(3) : 415 – 424
- Barrick D E and Snider J B (1977) The statistics of HF sea-echo Doppler spectra. *IEEE Trans Antennas Propagat* AP-25 (1) : 19 - 28
- Barrick D E (1980) Accuracy of parameter extraction from sample-averaged sea-echo Doppler spectra. *IEEE Trans Antennas Propag* 28 : 1 – 11
- Bathgate J S, Heron M L, Prytz A (2006) A new method of swell-wave parameter extraction from HF ocean surface radar spectra. *IEEE J Oceanic Eng* 31:812-818
- Breivik O, Saetra O (2001) Real time assimilation of HF radar currents into a coastal ocean model. *J Mar Syst* 28 : 161 - 182. DOI : 10.1016/S0924-7963(01)00002-1
- Broche P (1979) Estimation du spectre directionnel des vagues par radar decametrique coherent.

- AGARD Conference on special topics in HF propagation, Proc. Lisbon, 28 May-1 June, 1979.
AGARD-CP-263
- Broche P, Forget P (1993) Shallow water waves observed by a VHF groundwave Doppler radar.
Int J Remote Sens 14 : 2301 - 2314
- Chapman R D, Shay L K, Graber H C, Edson J B Karachintsev A, Trump C L, Ross D B (1997)
On the accuracy of HF radar surface current measurements: Intercomparisons with ship-based
sensors. J Geophys Res 102 (C8): 18737 - 18748. DOI: DOI: 10.1029/97JC00049
- Chen G, Chapron B, Ezraty R (2002) A global view of swell and wind sea climate in the ocean by
satellite altimeter and scatterometer. J Atmos Oceanic Technol 19: 1849 - 1859
- Crombie D D (1955) Doppler spectrum of sea echo at 13.56 Mc./s. Nature 175: 681-682. DOI:
10.1038/175681a0
- Crombie D D (1972) Resonant backscatter from the sea and its application to physical
oceanography. Engineering in the Ocean Environment, Ocean 72 - IEEE International
Conference, 13-15 Sept. 1972: 174-179. DOI: 10.1109/OCEANS.1972.1161189
- Cochin V, Forget P, Seille B, Mercier G (2005) Sea surface currents and wind direction by VHF
radar: results and validation. Conference Oceans 20-23 June 2005 - Europe 2: 942-947
- Collard F, Ardhuin F, Chapron B (2009) Monitoring and analysis of ocean swell fields from space:
New methods for routine observations. J Geophys Res 114: C07023. DOI: 10.1029/2008JC
005215
- Dexter P E, Theodoridis S (1982) Surface wind speed extraction from HF sky wave radar Doppler
spectra. Radio Sci 17 (3): 643-652. DOI: 10.1029/RS017i003p00643
- Donelan M A, Hamilton J, Hui W H (1985) Directional spectra of wind-generated waves. Philos
Trans R Soc Lond Ser A Math Phys Sci 315: 509-562
- Drennan W M, Graber H C, Donelan M A (1999) Evidence for the effects of swell and unsteady
winds on marine wind stress. J Phys Oceanogr 29: 1853-1864. DOI: [http://dx.doi.org/10.1175/
1520-0485\(1999\)029<1853:EFTEOS>2.0.CO;2](http://dx.doi.org/10.1175/1520-0485(1999)029<1853:EFTEOS>2.0.CO;2)
- Essen H H, Gurgel K W, Schirmer F (1983) Tidal and wind-driven parts of surface currents as
measured by radar. Dtsch Hydrogr Z 36: 81 - 96. DOI: 10.1007/BF02275373
- Forget P, Broche P, de Maistre J C, Fontanel A (1981) Sea state frequency features observed by
ground wave HF Doppler radar. Radio Sci 16(5) : 917 - 925. DOI : 10.1029/RS016i005p00917
- Forget P (1985) The wave field dynamics inferred from HF radar sea-echo. The Ocean Surface,
Eds Toba Y and Mitsuyasu H, Reidel Publishing Co., 257 - 262
- Forget P, Broche P, Cuq F (1995) Principles of swell measurement by SAR with application to
ERS-1 observations off the Mauritanian coast. International Journal of Remote Sensing 16:

2403-2422

- Frisch A S and Weber B L (1980) A new technique for measuring tidal currents by using a two-site HF Doppler radar system. *J Geophys Res* 85 (C1): 485 - 493. DOI: DOI: 10.1029/JC085iC01p00485
- Fujii S, Heron M L, Kim K et al (2013) An overview of developments and applications of oceanographic radar networks in Asia and Oceania countries. *Ocean Sci J* 48(1): 69 – 97. DOI: 10.1007/s12601-013-0007-0
- Gallet B, Young W R (2014) Refraction of swell by surface currents. *J Mar Res* 72: 105-126
- Gill E W, Khandekar M L, Howell R K, Walsh J (1996) Ocean surface wave measurement using a steerable high-frequency narrow-beam ground wave radar. *Journal of Atmospheric and oceanic technology*. 13 :703-713
- Green D, Gill E, Huang W (2009) An inversion method for extraction of wind speed from high-frequency ground-wave radar oceanic backscatter. *IEEE Trans Geosci Remote Sens* 47 (10): 3338-3346. DOI: 10.1109/TGRS.2009.2022944
- Grosdidier S, Forget P, Barbin Y, Guerin C A (2014) HF bistatic ocean Doppler spectra: simulation versus experimentation. *IEEE Trans Geosci Remote Sens* 52(4): 2138-2148. DOI: 10.1109/TGRS.2013.2258352
- Gurgel K W, Antonischki G, Essen H H, Schlick T (1999) Wellen radar (WERA): a new ground-wave based HF radar for ocean remote sensing. *Coast Eng* 37: 219 - 234
- Gurgel K W, Essen H H, Schlic T (2006) An empirical method to derive ocean waves from second-order Bragg scattering: prospects and limitations. *IEEE J Oceanic Eng* 31: 804-811. DOI: 10.1109/JOE.2006.886225
- Hanson J L, Phillips O M (2001) Automated Analysis of Ocean Surface Directional Wave Spectra. *J Atmos Ocean Technol* 18 : 277-293
- Hara T, Hanson K A, Bock E J, Uz B M (2003) Observation of hydrodynamic modulation of gravity-capillary waves by dominant gravity waves. *J Geophys Res* 108: 3208
- Harlan J, Georges T (1994) An empirical relation between ocean surface wind direction and the Bagg line ratio of HF radar sea echo spectra. *J Geophys Res* 99 (C4): 7971-7978
- Hasselmann K (1971) Determination of ocean-wave spectra from Doppler radio return from the sea surface. *Nat Phys Sci* 229: 16-17. DOI: 10.1038/physci229016a0
- Heron M L, Dexter P E, McGann B T (1985) Parameters of the air-sea interface by high-frequency ground-wave doppler radar. *Aust J Mar Freshwater Res* 36: 655–670
- Heron M L, Rose R (1986) On the application of HF ocean radar to the observation of temporal and spatial changes in wind direction. *IEEE J Oceanic Eng* 11(2): 210-218. DOI: 10.1109/

- JOE.1986.1145173
- Hildebrand P H, Sekhon R S (1974) Objective Determination of the Noise Level in Doppler Spectra. *J Appl Meteorol* 13: 808 - 811
- Hisaki Y (2005) Ocean wave directional spectra estimation from an HF ocean radar with a single antenna array : observation. *J Geophys Res* 110 (C11004). DOI: 10.1029/2005JC002881
- Howell R, Walsh J (1993) Measurement of ocean wave spectra using narrow-beam HF radar. *IEEE J Oceanic Eng* 18: 296 - 305. DOI: 10.1109/JOE.1993.236368
- Ivonin D V, Broche P, Devenon J-L, Shrira V I (2004) Validation of HF radar probing of the vertical shear of surface currents by acoustic Doppler current profiler measurements. *J Geophys Res* 109(C4): 1-8. DOI: 10.1029/2003JC002025
- Ivonin D V, Shrira V I, Broche P (2006) On the singular nature of the second-order peaks in HF radar sea echo. *IEEE J Oceanic Eng* 31 (4): 751 - 767. DOI: 10.1109/JOE.2006.886080
- Jiang H, Chen G (2013) A global view on the swell and wind sea climate by the Jason-1 mission: a revisit. *JAOT*. DOI: 10.1175/JTECH-12-00180.1
- Kim S Y, Terrill E J, Cornuelle B D et al (2011) Mapping the U.S. west coast surface circulation: a multiyear analysis of high-frequency radar observations. *J Geophys Res* 116: C03011. DOI: 10.1029/2010JC006669
- Kosro P M, Barth J A, Strub P T (1997) The coastal jet: Observations of surface currents over the Oregon continental shelf from HF radar. *Oceanography* 10 (2): 53 - 56
- Kudryavtsev V N, Makin V K (2004) Impact of swell on the marine atmospheric boundary layer. *J Phys Oceanogr* 34: 934-949. DOI: [http://dx.doi.org/10.1175/1520-0485\(2004\)034<0934:IOSO TM>2.0.CO;2](http://dx.doi.org/10.1175/1520-0485(2004)034<0934:IOSO TM>2.0.CO;2)
- Le Boyer A, Cambon G, Daniault N, Herbette S, Le Cann B, Marié L, Morin P (2009) Observations of the Ushant tidal front in September 2007. *Cont Shelf Res* 29: 1026-1037. DOI: 10.1016/j.csr.2008.12.020
- Lipa, B J, Barrick D E (1979) Ocean Swell Parameters from Narrow Beam HF Radar Sea Echo. Chapter 34 in AGARD Conference Proceedings Special Topics in HF Propagation. 28 May-1 June 1979. No. 263
- Lipa B J, Barrick D E, Maresca Jr J W (1981) HF radar measurements of long ocean waves. *J Geophys Res* 86 (C5): 4089-4102. DOI: 10.1029/JC086iC05p04089
- Lipa B J, Barrick D E (1983) Least squares methods for the extraction of surface currents from CODAR crossed-loop data: Application at ARSLOE. *IEE J Oceanic Eng* 8 (4): 226-253
- Lipa B J, Barrick D E (1986) Extraction of sea state from HF radar sea echo: Mathematical theory and modeling. *Radio Sci* 21(1): 81-100. DOI: 10.1029/RS021i001p00081

- Lipa B J, Nyden B (2005) Directional wave information from the SeaSonde. *IEEE J Oceanic Eng* 30: 221 - 231. DOI: 10.1109/JOE.2004.839929
- Lipa B J, Barrick D E, Bourg J, Nyden B B (2006) HF radar detection of tsunamis. *J Oceanogr* 62 : 705 - 716
- Lipa B, Barrick D, Alonso-Martirena A, Fernandes M, Ferrer M I, Nyden B (2014) Brahan project high frequency radar ocean measurements: currents, winds, waves and their interactions. *Remote Sens* 6: 12094-12117. DOI: 10.3390/rs61212094
- Liu Y, Weisberg R H, Merz C R (2014) Assessment of CODAR SeaSonde and WERA HF radars in mapping surface currents on the west Florida shelf. *J Atmos Oceanic Technol* 31: 1363-1382. DOI: <http://dx.doi.org/10.1175/JTECH-D-13-00107.1>
- Long A E, Trizna D B (1973) Mapping of North Atlantic winds by HF radar sea backscatter interpretation. *IEEE Trans Antennas Propag AP-21(5)*: 680–685
- Longuet-Higgins M S, Cartwright D E, Smith N D (1963) Observations of the directional spectrum of sea waves using the method of a floating buoy. *Ocean Wave Spectra*, Prentice-Hall, Inc., Englewood Cliffs N J, US, 111-136
- Lu Y, Hua F, Wei Z, Fan B (2008) Preliminary analysis on residual current along the section across the Jiaozhou Bay mouth (in Chinese). *Adv Mar Sci* 26 (3): 305-316
- Magne R, Belibassakis K A, Hervers T H C, Ardhuin F, O'Reilly W C, Rey V (2007) Evolution of surface gravity waves over a submarine canyon. *J Geophys Res* 112: C01002. DOI:10.1029/2005JC003035
- Marmain J, Molcard A, Forget P, Barth A, Ourmières Y (2014) Assimilation of HF radar surface currents to optimize forcing in the North Western Mediterranean sea. *Nonlin Processes Geophys* 21:659-675. DOI: 10.5194/npg-21-659-2014
- Mcwilliams J C, Huckle E, Liang J, Sullivan P P (2014) Langmuir turbulence in swell. *J Phys Oceanogr* 44: 870-890. DOI: <http://dx.doi.org/10.1175/JPO-D-13-0122.1>
- Muller H, Blanke B, Dumas F, Lekien F, Mariette V (2009) Estimating the Lagrangian residual circulation in the Iroise Sea. *J Mar Syst* 78: S17-S36. DOI: 10.1016/j.jmarsys.2009.01.008
- Muller H, Blanke B, Dumas F, Mariette V (2010) Identification of typical scenarios of the surface Lagrangian residual circulation in the Iroise Sea. *J Geophys Res* 115: C07008. DOI: 10.1029/2009JC005834
- Munk WH, Miller GR, Snodgrass FE, Barber NF (1963) Directional recording of swell from distant storms. *Phil. Trans. Roy. Soc. London*, A255: 505-584
- Paduan J D and Rosenfield L K (1996) Remotely sensed surface currents in Monterey bay from shore-based HF radar (Coastal Ocean Dynamics Application Radar). *J Geophys Res*101 (C9) :

- 20669 - 20686. DOI: DOI: 10.1029/96JC01663
- Paduan J D, Shulman I (2004) HF radar data assimilation in the Monterey Bay area. *J Geophys Res* 109: C07S09. DOI: 10.1029/2003JC001949
- Phillips O M (1966) *Dynamics of the Upper Ocean*. Cambridge University Press, London.
- Phillips O M, Banner M L (1974) Wave breaking in the presence of wind drift and swell. *J Fluid Mech* 66: 625-640
- Portilla J, Ocampo-Torres F J, Monbaliu J (2009) Spectral partitioning and identification of wind sea and swell. *J Atmos Ocean Technol* 26: 107 – 122
- Prandle D (1987) The fine structure of nearshore tidal and residual circulations revealed by HF radar surface current measurements. *J Phys Oceanogr* 17: 231 - 245. DOI: doi: [http://dx.doi.org/10.1175/1520-0485\(1987\)017<0231:TFSONT>2.0.CO;2](http://dx.doi.org/10.1175/1520-0485(1987)017<0231:TFSONT>2.0.CO;2)
- Rice S O (1961) Reflection of electromagnetic waves from slightly rough surfaces. *Theory of Electromagnetic Waves*, M Kline, Ed. New York: Interscience, 351 - 378
- Rogers W E (2002) An investigation into sources of error in low frequency energy predictions. Formal Report 7320-02-10035, Oceanography division, Naval Research Laboratory, Stennis Space Center, MS, pp 63
- Schmidt R O (1986) Multiple emitter location and signal parameter estimation. *IEEE Trans Antennas Propag* 34: 276-280. DOI: 10.1109/TAP.1986.1143830
- Sekhon R S, Srivastava R C (1971) Doppler radar observations of drop-size distributions in a thunderstorm. *J Atmos Sci* 28: 983-994. DOI: [http://dx.doi.org/10.1175/1520-0469\(1971\)028<0983:DROODS>2.0.CO;2](http://dx.doi.org/10.1175/1520-0469(1971)028<0983:DROODS>2.0.CO;2)
- Sentchev A, Forget P, Barbin Y, Yaremchuk M (2013) Surface circulation in the Iroise Sea (W. Brittany) from high resolution HF radar mapping. *J Mar Syst* 109-110(Suppl.): S153 - S168. DOI: 10.1016/j.jmarsys.2011.11.024
- Shay L K, Martinez-Pedraja J, Cook T M, Haus B K, Weisberg R H (2007) High-Frequency radar mapping of surface currents using WERA. *J Atmos Ocean Technol* 24: 484 - 503
- Shen W, Gurgel K-W, Voulgaris G, Schlick T, Stammer D (2012) Wind-speed inversion from HF radar first-order backscatter signal. *Ocean Dynamics* 62: 105-121. DOI: 10.1007/s10236-011-0465-9
- Shrira V I, Ivonin D V, Broche P, de Maistre J C (2001) On remote sensing of vertical shear of ocean surface currents by means of a single-frequency VHF radar. *Geophysical Research Letters* 28 (20): 3955-3958. DOI: 10.1029/2001GL013387
- Siddons L A, Wyatt L R, Wolf J (2009) Assimilation of HF radar data into the SWAN wave model. *J Mar Syst* 77(3) : 312 - 324. DOI: 10.1016/j.jmarsys.2007.12.017

- Smedman A, Högström U, Sahleé E (2009) Observational Study of Marine Atmospheric Boundary Layer Characteristics during Swell. *J Atmos Sci* 66: 2747 - 2763
- Snodgrass F E, Groves G W, Hasslemann K F, Miller G R, Munk W H, Powers W H (1966) Propagation of ocean swell across the Pacific. *Phil Trans. A259*: 431 - 497
- Stewart R H, Joy J W (1974) HF radio measurements of surface currents. *Deep Sea Res* 21: 1039-1049
- Stewart R H, Barnum J R (1975) Radio measurements of oceanic winds at long ranges: an evaluation. *Radio Sci* 10(10): 853-857. DOI: 10.1029/RS010i010p00853
- Taylor G L, Teague C C, Stewart R H, Peterson A M, Munk W H, Joy J W (1974) Wave directional spectra from synthetic aperture observations of radio scatter. *Deep Sea Res* 21: 989 - 1016
- Tolman H L (2008) A mosaic approach to wind wave modeling. *Ocean Model* 25: 35-47. DOI: 10.1016/j.ocemod.2008.06.005
- Wang W, Forget P, Guan C (2014) Inversion of swell frequency from a 1-year HF radar dataset collected in Brittany (France). *Ocean Dynamics* 64 : (10) 1447 - 1456
- Wait J R (1966) Theory of HF ground wave backscatter from sea waves. *J Geophys Res* 71: 4832 - 4839
- Wu X, Yang S, Cheng F, Wu S, Yang J I, Wen B, Shi Z, Tian J, Hou J, Ke H, Gao H (2003) Ocean surface currents detection at the Eastern China Sea by HF surface wave radar. *Chinese J Geophys.* 46 (3): 340 - 346
- Wyatt L R (1986) The measurement of the ocean wave directional spectrum from HF radar Doppler spectra. *Radio Sci* 21(3): 473 - 485. DOI: 10.1029/RS021i003p00473
- Wyatt L R (1990) A relaxation method for integral inversion applied to HF radar measurement of the ocean wave directional spectrum. *Int J Remote Sens* 11: 1481-1494. DOI: 10.1080/01431169008955106
- Wyatt L R (2000) Limits to the inversion of HF radar backscatter for ocean wave measurement. *J Atmos Oceanic Technol* 17: 1651-1666. DOI: [http://dx.doi.org/10.1175/1520-0426\(2000\)017<1651:LTTIOH>2.0.CO;2](http://dx.doi.org/10.1175/1520-0426(2000)017<1651:LTTIOH>2.0.CO;2)
- Wyatt L R, Ledgard L J, Anderson C W (1997) Maximum-likelihood estimation of the directional distribution of 0.53-Hz ocean waves. *J Atmos Oceanic Technol* 14: 591-603. DOI: [http://dx.doi.org/10.1175/1520-0426\(1997\)014<0591:MLEOTD>2.0.CO;2](http://dx.doi.org/10.1175/1520-0426(1997)014<0591:MLEOTD>2.0.CO;2)
- Wyatt L R (2005) HF radar for coastal monitoring - a comparison of methods and measurements. *Conference Oceans 20-23 June 2005 - Europe* 1: 314-318. DOI: 10.1109/OCEANSE.2005.1511732
- Wyatt L R, Green J J, Middleditch A, Moorhead M D, Howarth J, Holt M, Keogh S (2006)

- Operational wave, current, and wind measurements with the Pisces HF radar. *IEEE J Oceanic Eng* 31 (4): 819-834
- Wyatt L R, Green J J, Middleditch A (2011) HF radar data quality requirements for wave measurement. *Coastal Engineering* 58: 327 - 336. DOI: 10.1016/j.coastaleng.2010.11.005
- Yoshikawa Y, Masuda A, Marubayashi K, Ishibashi M, Okuno A (2006) On the accuracy of HF radar measurement in the Tsushima Strait. *J Geophys Res* 111: C04009. DOI: 10.1029/2005JC003232
- Young I R, Babanin A V, Zieger S (2013) The decay rate of ocean swell observed by altimeter. *J Phys Oceanogr* 43: 2322-2333. DOI: 10.1175/JPO-D-13-083.1
- Zhang J, Wang W, Guan C (2011) Analysis of the global swell distributions using ECMWF Re-analyses wind wave data. *J Ocean Univ China* 10(4):325-330. doi:10.1007/s11802-011-1859-5
- Zhao J, Chen X, Hu W, Chen J, Guo M (2011) Dynamics of surface currents over Qingdao coastal waters in August 2008. *J Geophys Res* 116: C10020. DOI: 10.1029/2011JC006954

Acknowledgements

Radar data were kindly provided by SHOM (Service Hydrographique et Océanographique de la Marine) thanks to the projects Previmer and EPIGRAM (funded under contract ANR-08-BLAN-0330). WAVEWATCH III wave model data was provided by the IOWAGA project funded by the ERC under grant number 240009. This study is supported by Ministry of Science and Technology of China (No.2011BAC03B01). The fellowship supported by CSC (China Scholarship Council) is appreciated.

I am deeply grateful to my supervisors Philippe Forget and Changlong Guan for their great instructions and generous help on my research, work and life. Friendship and help from colleagues of University of Toulon, Mediterranean Institute of Oceanography and Ocean university of China are much appreciated. Love from my families is the fundamental support throughout the PhD years.

CV

Weili WANG, female, born in February 1987.

2005.09-2009.06: College of Physical and Environmental Oceanography, Ocean University of China. B. S. in Marine Science.

2009.09-2011.06: College of Physical and Environmental Oceanography, Ocean University of China. M. S. in Physical Oceanography.

2011.09-now: College of Physical and Environmental Oceanography, Ocean University of China. Among which, 2012.09-2014.06: Mediterranean Institute of Oceanography, University of Toulon. Ph. D. in Physical Oceanography.

List of articles

1. Wang W, Forget P, Guan C (2014) Inversion of swell frequency from a 1-year HF radar dataset collected in Brittany (France). *Ocean Dynamics*. 64 (10) : 1447-1456.
DOI : 10.1007/s10236-014-0759-9
2. Zhang J, Wang W, Guan C (2011) Analysis of the global swell distribution using ECMWF re-analyses wind wave data. *J Ocean Univ China* 10 (4) : 325-330.
DOI : 10.1007/s11802-011-1859-5
3. Wang W, Forget P, Guan C (2015) Inversion and assessment of swell waveheights from HF radar spectra in the Iroise Sea. submitted to “*Ocean Dynamics*”,
First round revisions after review.